

**CHRONOMORPHIC CHARACTERIZATION AND RADIOLYTIC DEGRADATION ANALYSIS OF
POLYURETHANE WITH MONTE CARLO MODELING OF THE NEUTRON SPECTRA
SURROUNDING A GE PETTRACE CYCLOTRON**

A Thesis
Presented to
The Faculty of the Graduate School
At the University of Missouri

In Partial Fulfillment
Of the Requirements for the Degree
Master of Science

By
Christopher S. Algieri
Dr. John Brockman, Thesis Supervisor

May 2018

The undersigned, appointed by the dean of the Graduate School,
have examined the thesis entitled
**CHRONOMORPHIC CHARACTERIZATION AND RADIOLYTIC DEGRADATION ANALYSIS OF
POLYURETHANE WITH MONTE CARLO MODELING OF THE NEUTRON SPECTRA
SURROUNDING A GE PETTRACE CYCLOTRON**

Presented by
Christopher S. Algieri

A candidate for the degree of
Master of Science

And hereby certify that, in their opinion, it is worthy of acceptance.

Dr. John Brockman

Dr. John Gahl

Dr. Mahmoud Almasri

Acknowledgements

First and foremost I would like to thank Dr. John Brockman for the continued guidance offered throughout my graduate research and giving me the opportunity to work on this project. You have been an excellent teacher and mentor, thank you for helping an engineer survive in a chemistry realm. A special thanks to Dr. John Gahl for taking me under his wing and ushering me past the many obstacles within the University of Missouri Engineering department, your ongoing mentorship is enormously appreciated. And thank you Dr. Mahmoud Almasri for serving on my thesis committee and enlightening me with the most interesting course in ECE.

Thank you to Alex Saale for the many hours of assistance and expertise with the MURR cyclotron, without your help this project could not have happened. Thank you to Dr. David Robertson and the entire Robertson Research Group for the ongoing collaboration and support. I am appreciative to the MURR community, with a special thanks to Dr. Bill Miller, Charles Fairfax, Carl Herbold, Don Bryan, Mark Richardson, Greg Gunn, and Gayla Neumeyer who went out of their way to assist whenever possible.

Thanks to Dr. Michael Quinn for not only offering your proficiency of organic chemistry but functioning as my mentor while escorting me around Y-12 for a summer. Thanks to Brad Jeffries and Dr. C.W. Littlefield for your daily contributions and insight to this research and to Josh Jo and Jake Gallagher for assistance with sample analysis.

Lastly, thank you to my domestic partner, Moriah Morrison, for your consistent love and support, daily laughter, and always encouraging me to strive for happiness. You were the one constant in an otherwise chaotic, often vexing graduate experience.

Table of Contents

Acknowledgements.....	ii
List of Figures	v
List of Tables.....	viii
Abstract.....	ix
Chapter 1 Introduction.....	1
1.1 Introduction.....	1
1.2 Research Objectives	3
1.3 Brief Description of Thesis Content.....	4
Chapter 2 Background.....	5
2.1 Ubiquitous Use of Polyurethanes in Industrial and Nuclear Settings.....	5
2.2 GE PETtrace Cyclotron	8
2.3 Radiolysis from Fast Neutrons.....	12
2.4 Monte Carlo N-Particle Transport Code (MCNP).....	14
2.5 Current Work.....	15
2.5.1 Radiolysis of Polyurethanes	15
2.5.2 Neutron Flux Spectrum Surrounding Cyclotrons	18
Chapter 3 Polyurethane Synthesis.....	20
3.1 Y-12 Samples	20
3.1.1 Pre-polymers.....	20
3.1.2 Procedure.....	21
3.2 MU Samples.....	23
3.2.1 Pre-polymers.....	23
3.2.2 Procedure.....	25
Chapter 4 MURR: GE PETtrace Cyclotron.....	28
4.1 Operational Specifications.....	28
4.1.1 Schematics	28
4.1.2 Vault & Target Assembly.....	30
4.1.3 Neutron Production Considerations	34

4.2	MCNP Model of Neutron Flux Spectrum.....	36
4.2.1	Input File Structure	36
4.2.2	Experimental Data vs. Physics Models.....	38
4.2.3	MCNPX Visual Editor: Particle Simulations	45
4.2.4	Neutron Flux Spectrum	51
4.2.5	MCNP Dose Calculation.....	56
Chapter 5	Neutron Spectrum Validation	59
5.1	Sample Irradiation Stand	59
5.2	Activation Foils	61
5.3	Calibrated Irradiation Positions.....	64
5.4	Gamma Considerations	70
5.4.1	Cyclotron Vault.....	70
5.4.2	Cobalt-60 Beam Port.....	70
Chapter 6	Analysis of Irradiated Polyurethane	71
6.1	Attenuated Total Reflectance Fourier-Transform Infrared Spectroscopy.....	71
6.1.1	Mechanism and Sampling Technique	71
6.1.2	Pre-polymers.....	74
6.1.3	Atmospheric vs Degassed: Observed Isocyanate Reaction.....	76
6.1.4	Dose Dependent Physicochemical Changes.....	81
Chapter 7	Conclusions.....	90
7.1	Calibrated Neutron Flux Spectrum	90
7.1.1	Efficacy and Challenges.....	90
7.1.2	Future Applications	92
7.2	Dose Response of Irradiated Polyurethane.....	93
7.2.1	Efficacy & Challenges	93
7.2.2	Future Work	94
References	95
Appendix	98

List of Figures

Figure 2-1: Cyclotron principle of operation as specified by Lawrence [8].	8
Figure 2-2: GE PETtrace Cyclotron, showing an advanced electrode and magnet design.	10
Figure 2-3: MCNP6 particle types, energy ranges, and interaction physics [10].	15
Figure 2-4: N-C linkage in poly(ester-urethane)s [13].	17
Figure 3-1: PUR synthesis with pre-polymers Halthane 88 and Asilamine 170.	21
Figure 3-2: Schlenk line and vacuum desiccator with collar used to degas pre-polymers.	22
Figure 3-3: Cut 2x2 cm square samples and drilled 0.5 cm diameter samples pre-irradiation.	23
Figure 3-4: Synthesis of University of Missouri PUR samples.	24
Figure 3-5: PUR samples wrapped in aluminum foil prior to irradiation.	26
Figure 4-1: Schematic of GE PETtrace cyclotron [22].	29
Figure 4-2: Beam profile of MURR PETtrace 860 cyclotron.	31
Figure 4-3: Target assembly by Bruce Technologies for fluorine-18 production.	32
Figure 4-4: Niobium insert (left) and Havar foil (right) used in the target chamber.	33
Figure 4-5: Isotopic material specification of Havar foil.	37
Figure 4-6: Cross section curves for the oxygen-18 (p,n) reaction [25].	39
Figure 4-7: Neutron flux 3 inches from target using TENDL (black), CEM (blue), BERTINI (red), and INCL4 (green).	41
Figure 4-8: The 3 inch, "hot" irradiation position on the Bruce target assembly.	42
Figure 4-9: Bruce target assembly plotted in X-Z (left) and X-Y (right) planes with colored cells as modeled by The Visual Editor.	46
Figure 4-10: MCNP model of the Bruce and GE target assemblies and calibrated irradiated positions as represented by The Visual Editor.	47
Figure 4-11: 3D image of Bruce (top) and GE (bottom) target assemblies generated using The Visual Editor Code.	48
Figure 4-12: Particle track plot simulating 1.0×10^4 protons striking the water target in the Bruce target assembly.	49

Figure 4-13: Beam profile of MURR’s GE PETtrace cyclotron as modeled by MCNP.	50
Figure 4-14: Normalized neutron flux at 3” irradiation position during fluorine-18 production using Bruce target.....	51
Figure 4-15: Normalized neutron flux at 4.4” irradiation position during fluorine-18 production using Bruce and GE targets.	52
Figure 4-16: Normalized neutron flux at 9” irradiation position during fluorine-18 production using Bruce and GE targets.	53
Figure 4-17: Normalized neutron flux at 14” irradiation position during fluorine-18 production using Bruce and GE targets.	54
Figure 5-1: PUR samples secured at the 4.4, 9, and 14 inch irradiation positions.	59
Figure 5-2: Portable PVC stand with calibrated positions for irradiation at MURR.....	60
Figure 5-3: MCNP calculated neutron flux spectrum compared to the overdetermined ASTM unfolded spectrum at the 4.4” position for the Bruce target.....	65
Figure 5-4: MCNP calculated neutron flux spectrum compared to the overdetermined ASTM unfolded spectrum at the 4.4” position for the GE target.	66
Figure 5-5: MCNP calculated neutron flux spectrum compared to the overdetermined ASTM unfolded spectrum at the 9” position for the Bruce target.....	67
Figure 5-6: MCNP calculated neutron flux spectrum compared to the overdetermined ASTM unfolded spectrum at the 9” position for the GE target.	67
Figure 6-1: ATR interface (top left), PUR sample (bottom left), and 3D printed polypropylene sample holder.	72
Figure 6-2: Schematic diagram of ATR and total internal reflection principle [28].	73
Figure 6-3: IR spectra of pre-polymer A showing the presence of isocyanate and free urethane.	75
Figure 6-4: IR spectra of pre-polymer B used for synthesizing Y-12 PUR samples.	76
Figure 6-5: IR spectra comparing Y-12 PUR standard controls prepared under atmospheric conditions (STD ATM) and when pre-polymers were degassed under vacuum (STD DG).	77
Figure 6-6: IR spectra of degassed PUR samples from treatment group 1.....	78
Figure 6-7: Sample 1 treatment groups 1 and 4 and non-irradiated control prior to and following irradiation.	79

Figure 6-8: Sample 2 IR spectra comparing treatment group 1 with standard control and pre-irradiation. 80

Figure 6-9: Comparison of non-irradiated control Y-12 ATM PUR versus treatment groups 1-6. 81

Figure 6-10: Dose response of secondary amines and alcohol in ATM PUR. 82

Figure 6-11: Ether cleavage following neutron exposure in ATM PUR..... 83

Figure 6-12: Urea and Urethane concentrations for Y-12 ATM PUR samples groups 1-6..... 84

Figure 6-13: Sample 7 IR spectra of treatment groups 1, 5, and non-irradiated control before and after irradiation..... 85

Figure 6-14: Sample 7 urethane and urea concentrations prior to and post irradiation. 86

Figure 6-15: Sample 4 IR spectra of treatment groups 1, 4, and non-irradiated controls before and after irradiation..... 87

Figure 6-16: Regression analysis of the urethane to urea concentrations as a function of neutron dose for sample 4 (prepared under ATM conditions). 88

Figure 6-17: Regression analysis of the amine to urea concentrations as a function of neutron dose for sample 4 (prepared under ATM conditions). 89

List of Tables

Table 2.1: Types of commonly synthesized PURs and their applications in industry [2, 3].....	6
Table 2.2: Neutron classification according to kinetic energy.....	12
Table 3.1: PUR samples synthesized at the University of Missouri.	27
Table 4.1: Elemental composition of Havar foil with probable modes of activation producing neutrons.....	35
Table 4.2: Measurements of Bruce and GE target assemblies.	36
Table 4.3: Simulation runtime and calculation uncertainty for TENDL, CEM.03, BERTINI, and INCL models.....	43
Table 4.4: Comparison of TENDL neutron flux to CEM, BERTINI, and INCL models for Bruce target assembly at the 3 inch position.	44
Table 4.5: Total neutron flux contributions at 4.4, 9, and 14 inch irradiation positions.	54
Table 4.6: Compared neutron flux calculated using a F5 and F4 tally for the 4.4” irradiation position during fluorine-18 production using the Bruce target.....	55
Table 4.7: Calculated neutron dose, per second, at 4.4, 9, and 14 inch positions during fluorine-18 production.....	56
Table 4.8: The irradiation position, target run time, and dose associated with each treatment group for the samples prepared at Y-12.....	58
Table 4.9: The irradiation position, target run time, and dose associated with each treatment group for the samples prepared at MU.....	58
Table 5.1: Characteristics of the activation foils used for spectrum validation.	61
Table 5.2: Activation foils irradiation parameters.	62
Table 5.3: Decay corrected foil activities at the 4.4 and 9 inch positions.	63
Table 5.4: Total fast neutron flux from MCNP and Overdetermined ASTM unfolding.	68
Table 5.5: Fast neutron flux from MCNP using CEM physics model.....	69
Table 5.6: Fast neutron flux from MCNP using BERTINI physics model.	69
Table 5.7: Fast neutron flux from MCNP using INCL physics model.....	69

Abstract

This thesis describes the development of fast neutron irradiation positions at the MURR GE PETtrace cyclotron for polyurethane (PUR) radiolysis studies. Monte Carlo N-Particle (MCNP) Transport code was used to calculate the fast neutron flux spectra and absorbed neutron dose at the irradiation positions during routine fluorine-18 production. The calculated MCNP neutron flux is validated using neutron activation threshold foils with spectrum unfolding techniques. The a priori MCNP flux and experimentally measured flux spectra are ultimately shown to validate using TENDL-2015 cross section data for neutron production reactions by comparing results with CEM03.03, BERTINI INC, and INCL physics models within MCNP.

Following irradiation of PUR, the degree of radiolysis was analyzed using attenuated total reflectance Fourier-transform infrared spectroscopy (ATR-FTIR) to quantify neutron dose dependent changes. Collectively, the results show that PURs do not appear to be affected up to doses of 5 kGy and should be considered for use in radiation fields.

Chapter 1 Introduction

1.1 Introduction

Ionizing radiation can induce a variety of physicochemical changes in materials by either liberating atomic electrons or by reacting with the nuclei of the material. Neutron radiation is an example of the latter and is a form of indirectly ionizing radiation capable of causing material decomposition, activation, embrittlement, cracking, and other structural changes. High energy neutrons can be especially damaging as they can induce hydrogen “knock on” reactions, creating high linear energy transfer (LET) proton ions in the material. Organic polymers, like PURs, are affected by radiation by crosslinking and chain scission. Cross linking occurs when a bond is formed between polymer chains and results in a more rigid material as the individual chains lose some of their ability to move freely. Chain scission, or chain cleavage, occurs when an individual polymer chain degrades. Either process can lead to physicochemical changes in the material which alter performance. An understanding of the radiation effects observed in PURs is particularly important in industries in which they are commonly exposed to high levels of radiation, such as in nuclear applications.

Calibrated sources of neutrons are needed for polymer radiolysis studies. These facilities are typically found at research reactor facilities or accelerators. One underutilized irradiation source is medical isotope production cyclotrons. These cyclotron facilities are used to produce medical isotopes for nuclear medicine applications including diagnostic information, radiotherapy, and sterilization of medical

equipment. In the mid-1970s, the now widely used imaging modality called positron emission tomography (PET) gained acceptance within the scientific community as a functional and beneficial imaging technique [1]. A PET camera, used in combination with fludeoxyglucose (FDG) as a glucose analog, allows for high quality imaging of brain, heart, and lung functionality as well as cancer diagnosis. FDG, which is synthesized using fluorine-18, has since evolved as by far the most widely used radiopharmaceutical in PET imaging. Fluorine-18 is most commonly produced using a cyclotron and due to its high demand and 109 minute half-life is made daily at hospitals, industrial facilities, and research sites around the world. The University of Missouri Research Reactor (MURR) houses a 16 MeV GE PETtrace cyclotron used to produce radioisotopes for medical purposes. The production of medical isotopes at cyclotron facilities also produces secondary neutron and gamma fields. In this work, an irradiation position is developed for irradiating PUR polymer samples at the MURR cyclotron during routine production of F-18. Following irradiation of PUR, the degree of radiolysis was analyzed using ATR-FTIR techniques to quantify neutron dose dependent changes.

MCNP code was used to calculate the neutron flux spectra emitted from the GE PETtrace cyclotron and calibrate two irradiation positions within the vault. PUR samples were irradiated to a neutron dose of 70–5540 Gy. The development of the MCNP cyclotron model, and calculation and validation of the fast neutron flux, is a major focus of this report. While ultimately used here for material radiolysis experiments, knowledge of the radiation field around the cyclotron at MURR has applications for

secondary radioisotope production, controlled therapy, validating dosimetry techniques, and improving radiation health and safety in general.

1.2 Research Objectives

The main objectives of this research are to develop fast neutron irradiation positions at the MURR PETtrace cyclotron and to identify neutron dose dependent physicochemical changes in PUR samples. These objectives are further defined as follows:

1. Develop fast neutron irradiation positions at MURR GE PETtrace cyclotron:
 - a. Develop a MCNP model of the MURR GE PETtrace cyclotron to calculate fast neutron flux.
 - b. Validate the MCNP model using neutron activation foils and spectrum unfolding techniques.
 - c. Calculate the absorbed neutron dose at irradiation positions during routine fluorine-18 production.
2. Identify physicochemical changes in irradiated PUR samples:
 - a. Irradiate PURs with varying production characteristics.
 - b. Expose samples to a controlled neutron dose between 70 – 5540 Gy.
 - c. Assess neutron and gamma radiolysis degradation using ATR-FTIR.

1.3 Brief Description of Thesis Content

This thesis is comprised of seven chapters which are organized as follows. Chapter one introduces the major topics of interest and outlines the objectives of this research.

Chapter two provides relevant background information of the main subjects to be discussed including the use of (PURs) in industrial and nuclear settings, cyclotron production of fluorine-18, material radiolysis from fast neutrons, and MCNP. This is followed with a brief summary of current work associated with polymer radiolysis from fast neutrons and the use of MCNP for modeling the neutron fluence around a PETtrace cyclotron.

Chapter three summarizes the procedures used by Dr. Michael Quinn and Dr. C.W. Littlefield in the synthesis of various PUR samples. The different production characteristics and types of samples created are explained.

Chapter four details the operational parameters of the GE PETtrace cyclotron at the MURR. This includes an explanation of the cyclotron vault, target assemblies, proton beam, and neutron production considerations during routine fluorine-18 production. The development and functionality of the MCNP model is described and the resulting neutron flux spectrum using TENDL is presented for the irradiation positions. The MCNPX Visual Editor Code is used to track particle paths and the calculated flux results are used to determine the absorbed neutron dose.

Chapter five discusses how the calculated MCNP neutron flux was experimentally validated using activation flux foils as threshold detectors and compares TENDL cross section data with CEM, BERTINI, and INCL physics models. This includes measurement of the neutron induced activities with HPGe, irradiation stand design, neutron unfolding methods, and gamma considerations during cyclotron irradiation.

Chapter six describes the analysis of the irradiated PUR samples using ATR-FTIR. This includes identifying dose-dependent changes in the molecular structure, characterizing changes in the concentration of certain functional groups, and quantifying any correlations using regression analysis. In chapter seven, conclusions are drawn and future work is discussed.

Chapter 2 Background

2.1 Ubiquitous Use of Polyurethanes in Industrial and Nuclear Settings

PURs are a useful class of polymers that are heavily relied on to solve a wide range of challenging problems. PURs are generally formed by reacting a polyol with a diisocyanate. It is this simple reaction that allows PURs to be one of the most versatile plastic materials, as there exists a variety of both diisocyanates and polyols which can be employed in order to produce a broad spectrum of materials.

To compete with the expanding nylon market, PUR was first synthesized in 1937 by Otto Bayer [2]. It was quickly recognized for its elastomeric properties resulting in worldwide industrial scale production soon thereafter. Today, PURs can be observed in

commercial applications ranging from building insulation to adhesives. Table 2.1 lists the types of PURs commonly used in industry along with some of their corresponding applications [2, 3].

Table 2.1: Types of commonly synthesized PURs and their applications in industry [2, 3].

<u>Characteristics</u>	<u>Applications</u>
Rigid, Low-Density	Construction (Insulation Foam) Automotive Appliances
Rigid, Solid	*RIM Solid Plastics Mechanical
Semi-Rigid, Low-Density	Packaging Foam
Semi-Rigid, Solid	Cast Elastomers Coatings Adhesives/Sealants Medical
Flexible, Low-Density	Automotive Foam Bedding Foam Upholstery
Flexible, Solid	Flooring (Carpeting) Apparel (Footwear Midsoles) Print Rollers

*Reaction injection molding

Materials based on organic polymers are also widely used throughout the nuclear industry where they can be subjected to high energy radiation for long periods of time. As is the case with typical commercial items like plastic surfaces, gloves, and building materials, specialty items such as jacketing cables, adhesives, and encapsulates all take advantage of the simple chemistry defining polymers to address specific problems [4]. One such example of this is the use of polymer containing packages and containers to safely store certain types of radioactive waste in geological disposal repositories [5]. Understanding the degree of radiolysis observed due to the radionuclides contained by

the waste packages is needed to evaluate its shielding and containment effectiveness, while providing accurate safety and environmental assessments.

Nuclear applications in particular require that the PUR material retain its physicochemical properties for which it was initially chosen for many years. For some specialty adhesives, this means retaining its chemical properties regardless of the chemically, thermally, or in the case of a nuclear setting, radiatively harsh environments. These chemical properties include the fluidity required for application to various irregular substrates, the cure reactions needed to produce high-molecular weight materials of strong cohesion, and the range of polarities and hydrogen bonding needed to form strong adhesive bonds [2]. It is because of these chemical properties that PURs were first identified as a promising candidate for specialty adhesives. One such specialty adhesive is Halthane 88-3, a PUR developed in the mid-80s by Lawrence Livermore National Laboratory (LLNL) and Y-12 National Security Complex, in collaboration with the Department of Energy (DOE). Developed as a safer alternative to the previous formulation, it uses a non-carcinogenic curing agent mixture (i.e. Asilamine) in place of the suspect carcinogen toluene diisocyanate (TDI) [6]. While safer to synthesize and employ as an adhesive, due to its lower aromatic content it is more susceptible to radiation induced degradation [7]. The diverse chemical compositions and endless variations in concentrations of hard and soft segments lends to extreme customization of PUR materials for a particular application. A general understanding of the chemical and mechanical changes observed in altered PURs from different types and levels of

radiation exposure is crucial from a basic health and safety standpoint and for their continued development.

2.2 GE PETtrace Cyclotron

The cyclotron is the most commonly used device for accelerating particles for low energy nuclear reaction applications [1]. First developed in 1934 by Ernest O. Lawrence as an “apparatus for the acceleration of ions”, the described method is based on cumulative action of a succession of accelerating impulses [8]. The basic principle of operation, as specified by Lawrence is illustrated below in Figure 2-1.

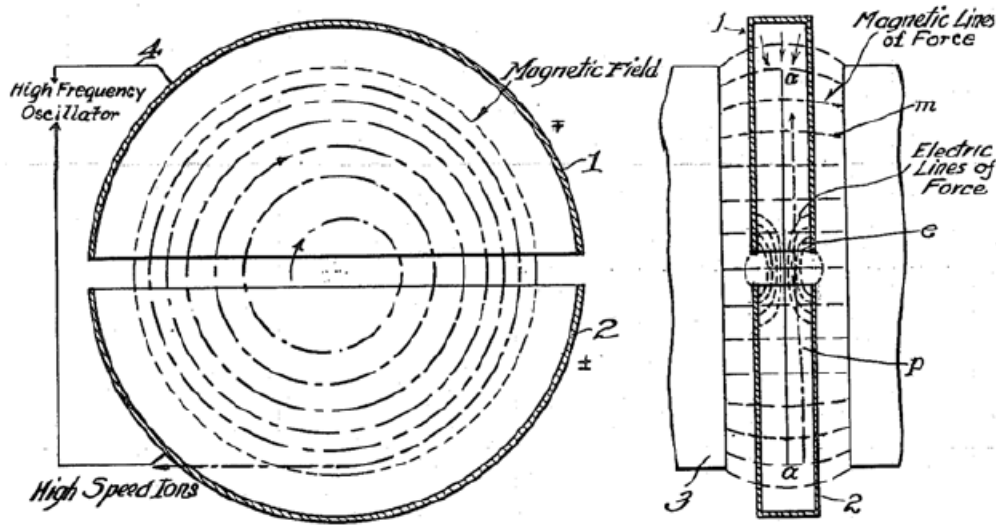


Figure 2-1: Cyclotron principle of operation as specified by Lawrence [8].

In Figure 2-1, the first sketch, left, is a diagram in which two electrodes, labeled 1 and 2, are positioned with a gap between them allowing for the injection of particles. An alternating electric potential is used to accelerate the ions. The second sketch, right, in

Figure 2-1 is a diagram of the electrostatic and magnetic fields produced from the two semi cylindrical hollow electrodes and powerful magnet. A charged particle will begin in the center of the electrodes and begin to gain energy as it is accelerated from one electrode to the other due to the high radio frequency electric field (RFEF) created between the two. With one magnet pole above and the other below the electrodes, the charged particle experiences a static magnetic field resulting in a circular drift and eventually spiraling outwards. In order to consistently accelerate the particle between the electrodes, the generated electric pulse must alternate in direction to align with the particles travel and have the same frequency as the particle. This frequency is referred to as the particle's cyclotron frequency and is given below:

$$f = \frac{qB}{2\pi m}$$

Equation 2.1

In Equation 2.1, q is the electric charge of the particle, B is the strength of the magnetic field, and m is the mass of the particle. The expression above allows particles to experience the same accelerating pulse between the electrodes many times throughout their spiraling path outwards, with no dependency on the radius of their path.

Since its origination, the basic concept of utilizing the same electrode system to accelerate particles into a circle has proven to be a valuable tool throughout the scientific community. Today, cyclotrons are used by facilities worldwide for medical applications including isotope production, equipment sterilization, and various forms of therapy to treat cancer. Of these, the production of radioisotopes for nuclear medicine

applications has become increasingly vital for assessing biological processes in vivo. The PETtrace cyclotron series by GE Healthcare is one of many modern systems designed specifically for fast, easy, and efficient production of PET tracers (radionuclides required for position-emission tomography). Figure 2-2 shows how the electrodes, referred to as “dees”, and magnets are configured in the GE cyclotron system.

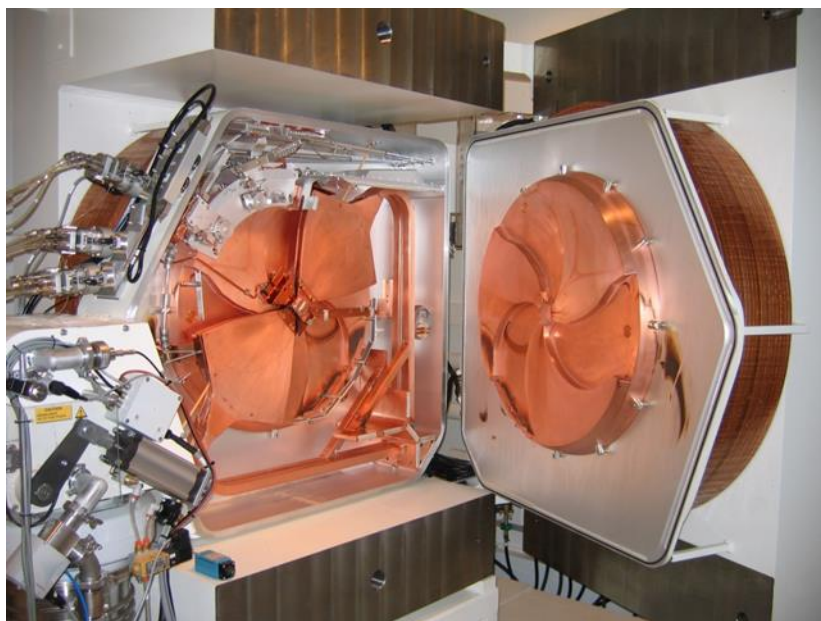
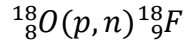


Figure 2-2: GE PETtrace Cyclotron, showing an advanced electrode and magnet design.

Capable of producing high energy protons and deuterons, the system can be configured with various targets and process systems to produce an array of commonly used PET radioisotopes.

The most widely used radioisotope is 2-[¹⁸F]fluoro-2-deoxy-D-glucose (FDG), also referred to as fludeoxyglucose. It functions as a glucose analog and is thus useful in analyzing metabolism throughout the body and for cancer diagnosis. It is most commonly produced via the proton bombardment of oxygen-18 enriched water causing

a (p,n) reaction and resulting in fluorine-18 and neutron by-product. This nuclear reaction is given below:



Equation 2.2

The Q value is calculated below:

$$Q = 931.5 \frac{\text{MeV}}{\text{amu}} (17.999161 + 1.0078250 - (1.0086649 + 18.000938)) = -2.44 \text{ MeV}$$

Equation 2.3

With a Q value of -2.44 MeV, the reaction is endothermic and thus requires a certain net energy input to occur. The amount of energy required can be calculated using the following expression:

$$T_{th,a} = |Q| \frac{m_Y + m_b}{m_Y + m_b - m_a}$$

Equation 2.4

In Equation 2.4, Q is the same Q value as previously calculated, m_Y is the atomic mass of the product formed (fluorine-18), m_b is the atomic mass of the emitted particle in the reaction (neutron), and m_a is the atomic mass of the incident particle (proton). Equation 2.4 requires that the bombarding protons must have a minimum energy of 2.58 MeV to produce fluorine-18 and the resulting neutron by-product. The GE PETtrace cyclotron provides a reliable source of protons with energies exceeding 2.58 MeV for the sole purpose of controlled and efficient isotope production.

2.3 Radiolysis from Fast Neutrons

Radiation chemistry focuses on a specific subdivision within radiochemistry in which the effects of externally applied radiation on chemical systems is studied. In contrast to charged particles and electromagnetic radiation, neutrons interact predominantly with nuclei. Lacking an electric charge, the neutral particles travel in straight lines until reaction with a nucleus. Neutrons are spherical with a radius of approximately 1 fm, or 10^{-15} m, while nuclei typically measure 10^{-14} to 10^{-15} m in size and can be spherical or spheroidal. This causes the probability that a neutron will interact, or collide, with a nucleus to be extremely low. Because of this neutrons are generally very penetrating and create recoiling nuclei when traveling through matter.

The probability for a nuclear reaction to occur is expressed in terms of reaction cross-section with the standard unit being the barn (b), where 1 b is equal to 10^{-24} cm². Neutron reactions are dependent on the incident neutron energy. The classification of neutron energies is given below in Table 2.2:

Table 2.2: Neutron classification according to kinetic energy.

Thermal neutrons	0.025 – 1 eV
Resonance neutrons	1 eV – 1 keV
Fast neutrons	0.5 – 20 MeV

Thermal neutrons have an average energy of 0.04 eV, while the most probable energy is 0.026 eV and are most likely to undergo elastic scattering or absorption in the form of radiative capture [9]. In elastic scattering reactions no energy is converted into nuclear excitation. Elastic scattering is commonly conceptualized as a billiard ball collision.

Radiative capture is a (n,γ) reaction in which a compound nucleus is formed by the absorption of the incident neutron and followed by de-excitation by gamma emission. As the neutron energy increases, radiative capture decreases by v^{-1} . At energies greater than 1 MeV, threshold reactions such as (n,p) , $(n,2n)$, and (n,α) , may take place. It is these nuclear transmutations, in addition to the nuclear recoil resulting from elastic collisions, which allow the propagation of fast neutrons through matter to cause such significant radiation damage. Because the neutron scattering cross section for hydrogen is on the order of 80 b, compared to the neutron absorption cross section of approximately 0.3 b, nuclear recoil from elastic collisions will be the most important consideration.

Fast neutrons have kinetic energies one million times greater than the bond energies, typically 1-5 eV, existing between the atoms of the absorbing material. Interactions of neutrons, via charged particle production or gamma rays, results in excitation and ionization with the potential of forming free radicals and radical ions. A radical is a molecule or ion with an unpaired valence electron. Highly reactive radicals are likely to interact with adjacent polymer chains via crosslinking or chain scission. The degree in which these chemical processes, in addition to any physical deformations, are observed following exposure to varying neutron dose environments is a major focus of this report. Neutrons may produce a different signature than low LET gamma rays because of the “in-situ” high LET radiation products provided by elastic and inelastic scatter reactions.

2.4 Monte Carlo N-Particle Transport Code (MCNP)

MCNP code is utilized for an array of nuclear particle transport applications throughout the nuclear science community. Initially developed in 1957 utilizing FORTRAN language computation to investigate how neutrons and photons interact with bulk matter, the code has since evolved and vastly expanded its capabilities. There are thousands of users worldwide focusing on a broad range of topics including nuclear criticality safety, reactor design, medical physics, radiation shielding, high-energy dosimetry, neutron detection, and accelerator isotope production investigations. It is maintained by Los Alamos National Laboratory and is distributed by the Radiation Safety Information Computational Center (RSICC) in Oak Ridge, TN. While MCNP6.2 is currently in beta release, MCNP6.1 is the most recent version fully released and is designed to transport 37 different particle types over a broad range of energies while offering new and improved data tables and physics models to further improve the radiation transport simulation [10].

The MCNP6 software reads a user created text file, or “deck”, and runs the resulting simulation returning data and information back to the user in an “output” text file. The input file consists of three main parts, or blocks; *cell* definitions, *surfaces* used, and specified *data*. The user defined surfaces are used to create the geometry of the problem. Using Boolean logic, these surfaces are then used to define cells which can be considered as an arbitrary three-dimensional configuration of materials. The last block is for specifying data and is used to define details such as the type of particles, problem materials, radiation source(s), output tally, and specify which data libraries to utilize.

The MCNP6 code utilizes the evaluated nuclear data files (ENDF). The current version is the ENDF/B-VII.1 data library which expanded the neutron sub libraries and now includes a total of 423 nuclide data sets. Information of the types of particles, energy ranges, and how the software simulates interactions with matter is given below in Figure 2-3.

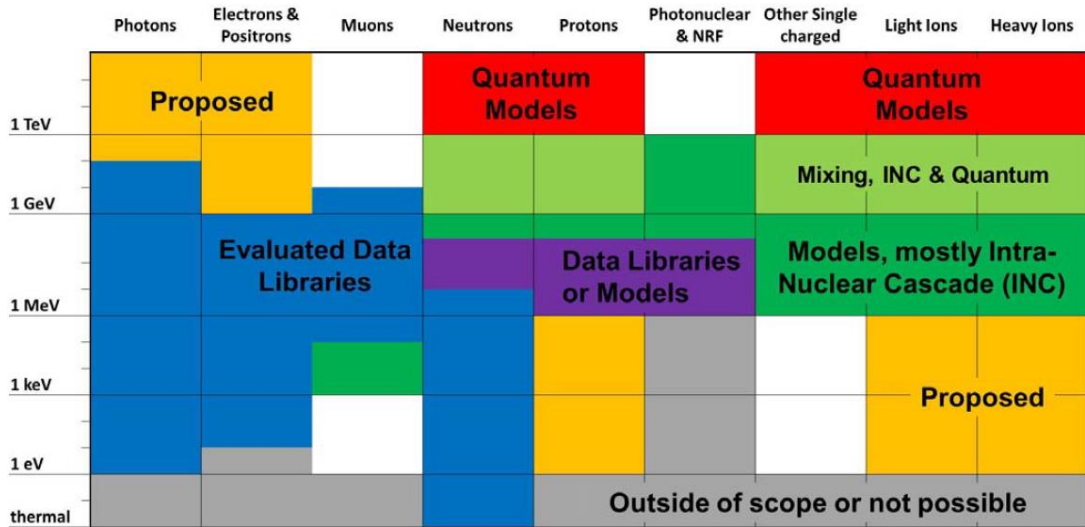


Figure 2-3: MCNP6 particle types, energy ranges, and interaction physics [10].

For the purpose of the present analysis, protons (MeV range) and neutrons (ranging from thermal to fast) are of importance. As evident in Figure 2-3, this requires the combination of measured library data and predictive models built-in to the MCNP6 software.

2.5 Current Work

2.5.1 Radiolysis of Polyurethanes

Exposure to fast neutrons has been found to cause structural modifications in polymers [11]. Rivaton & Arnold (2008) found that a neutron irradiation in the range of

130-320 cGy results in changes of the glass transition temperature or crystallinity, ultimately altering the polymer architecture. Based on experiments involving 13 polymers with varying matrixes, the study reported free radical formation and determined that no scission of double bonds occurred in neutron irradiations.

In general, the radiolysis mechanisms of PURs are relatively well known as discussed by Fromentin et al (2016). The findings show that crosslinking dominates under inert conditions, whereas chain scission is preferential under oxidative conditions. Radio-oxidation resulting from low-ionizing radiation was determined to lead to the formation of gaseous products. Specifically, radio-oxidation was associated with the following products: esters, aldehydes, alcohols, carboxylic acids, peresters, and peroxyacids [5, 12, 13]. Walo et al (2012) investigated the effects of gamma radiation on the chemical structure of PUR components with an emphasis on comparing poly(ester-urethane)s with different hard/soft segment contributions. The study observed the same radicals upon exposure but of various concentrations for soft and hard segments of ratio 40:60 and 60:40. Free radical production in hard segments was found to be dependent on the cleavage of urethane bonds, with the most radiation sensitive being the N-C linkage upon scission. The chemical structure of poly(ester-urethane)s is shown below in Figure 2.4, showing the radiation sensitive N-C linkage.

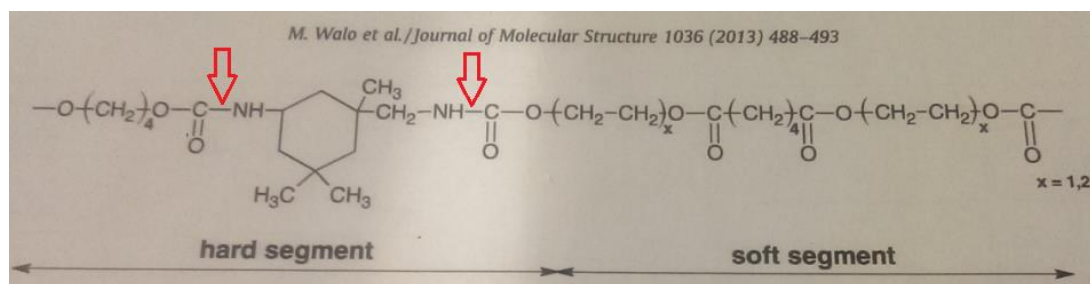


Figure 2-4: N-C linkage in poly(ester-urethane)s [13].

The study found that scission of the N-C linkage was followed by the emission of CO₂. In the ester soft domains, ester radicals were observed via chain scission.

Adem et al (2015) studied the effect of electron beam irradiation (50–4000 kGy) on aliphatic thermoplastics and found that the melting point of the hard segment decreased linearly while the glass transition temperature of the soft segment increased linearly with irradiation. This contrasts with literature studies examining aromatic PURs that observe an increase in hard segment melting point and decrease in the soft segment, poly(tetra methylene) glycol (PTMEG), glass transition temperature with dose.

Aymes-Chodur et al (2011) reported on the degradation mechanism for gamma-irradiated PTMG which is used frequently in industry as the soft segment for thermoplastics due to its low glass transition point, elasticity, and high strength. The study found signatures of formate, the anion derived from formic acid, as the major oxidation product and evidence of crosslinking. These degradation signatures and macromolecular changes were found to be significantly different between low molecular compounds and various polymer samples.

2.5.2 Neutron Flux Spectrum Surrounding Cyclotrons

Cyclotrons are now prevalent in hospitals, industrial facilities, and research sites around the world. These accelerators are often constructed as turnkey facilities, with the major objective being to producing medical isotopes. Knowledge of the radiation field around biomedical cyclotrons is necessary not only from a radiation safety standpoint but for potentially utilizing secondary neutron radiation fields for controlled therapy, material radiolysis experiments, and testing/validating dosimetry techniques. Various experimental measurement techniques, in combination with modeling, have been used to determine the spectral distribution of the neutron energy around PET cyclotrons [15-21]. Guimarães et al (2012) used a Bonner multisphere spectrometry (BSS) system and unfolding codes BUMS and NSDUAZ to measure the neutron spectra around a GE-PETtrace 8 cyclotron during F-18 production. The unfolded neutron spectra were generally in good agreement with each other as well as published data, with slightly varying results at specific energy ranges. The study identifies the need of an unfolding code that allows the input of a previously simulated starting spectrum obtained using the monte carlo method, to optimize the unfolding algorithm.

Similarly, Lacerda et al (2014) employed a BSS system and unfolding codes BUNKIUT, BUMS, and NSDUAZ to obtain experimental data and compared the results with the Monte Carlo code MCNPX simulated results. The neutron spectra was measured and simulated at 4 points around a GE-PETtrace 8 cyclotron during production of FDG-18. The study found that simulated and experimental spectra disagreed by a

factor as high as 14. The work identified the simulation data libraries, selection of the appropriate matrix response suitable for BSS, and the modeling as the causes for the discrepancy.

Cruzate (2015) estimated the neutron and photon energy spectra following the proton bombardment of a $H_2^{18}O$ target using MCNPX code. The study found that calculations using TENDL-2012 cross section data were validated with previous results benchmarked from the Japan Atomic Energy Agency (JAEA). The radiation source term presented can function as a reference for more complete models aiming to provide estimates on the neutron activation of accelerator components, calculate shielding, and carry out radiation protection evaluations in general.

A limited number of studies have reported on applications of the secondary radiation produced during F-18 production beyond those concerning shielding, dosimetry purposes, and radiation safety in general. Infantino et al (2015) reports on the production of Ar-41 in air inside the vault of a GE PETtrace cyclotron during routine production of F-18. Direct experimental measurements of the Ar-41 production are compared with Monte Carlo simulations performed with the FLUKA code, with the simulations ultimately resulting in an overestimation by a factor of 2. While this study may directly prove useful in a variety of radiation protection applications, it also showcases the broad capability, scalability, and rapid assessment of Monte Carlo modeling, specifically in regard to activation of materials due to secondary radiation.

Auditore et al (2017) presented a theoretical estimation of Cu-64 yields induced by the neutrons emitted during routine F-18 production. MCNPX code was used based on ENDF71x and TENDL-2015 data libraries along with experimental data from EXFOR database when available. The secondary target used was 99% Zn-64 enriched cylindrical disks segmented around the F-18 chamber to maximize neutron exposure and weighed a total of 241.8 g. The study found that in order to obtain a yield of Cu-64 relevant for medical purposes, a 30 MeV proton beam would be required. While this is considerably higher than the 15-16.5 MeV beam energy commonly used by medical cyclotrons for F-18 production, the notion of combined production of medical isotopes represents one potential application stemming from a better understanding of the neutron flux spectrum surrounding a cyclotron.

Chapter 3 Polyurethane Synthesis

3.1 Y-12 Samples

3.1.1 Pre-polymers

The University of Missouri and the Y-12 National Security Complex collaborated to irradiate and characterize a specialty PUR adhesive known as Halthane 88. The PUR elastomer is an attractive material for a variety of applications and understanding its strength is important during assembly and disassembly operations [6]. PUR samples were synthesized at Y-12 by mixing pre-polymer A, Halthane 88, with pre-polymer B, Asilamine 170, at a weight ratio of 100:21. Pre-polymer A was comprised of the aliphatic Diisocyanate $H_{12}MDI$ and Polytetramethylene Ether Glycol (PTMEG) with an average

molecular weight of 2000. The Halthane 88 was acquired from the National Nuclear Security Administration's Kansas City National Security Campus and was pre-synthesized. Asilamine 170 curing agent was comprised of two isomers and is given below in Figure 3-1 along with the PUR synthesis.

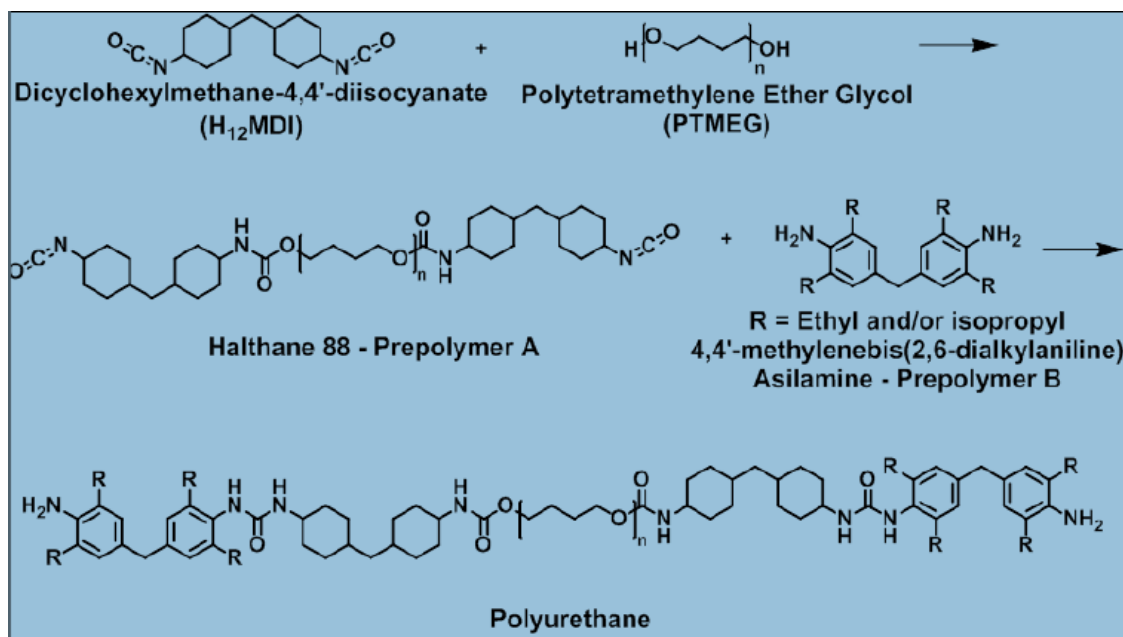


Figure 3-1: PUR synthesis with pre-polymers Halthane 88 and Asilamine 170.

3.1.2 Procedure

Dr. Michael Quinn, an organic chemist and project collaborator from Y-12, performed the synthesis of the Y-12 PUR samples. Pre-polymers A and B were thoroughly mixed and then Teflon coated steel plates were used to press the PUR adhesive into 3.20 mm thick sheets. Dow Corning high-vacuum silicone grease was used to prevent the adhesive from sticking to the Teflon coated plates and ensure no trace fluorine would be transferred to the samples. One group of samples was prepared

under atmospheric conditions, while the other group was degassed under vacuum prior to mixing. To achieve this, the pre-polymers were degassed utilizing a Schlenk line and vacuum desiccator with collar, as shown in Figure 3-2.



Figure 3-2: Schlenk line and vacuum desiccator with collar used to degas pre-polymers.

After allowing the PUR to fully cure, samples of varying size and shape were formed from the large sheets. When completely cured, the samples were gently wiped with hexane to remove any residual silicone grease. Some samples were cut directly from the sheets into 2x2 cm squares, while others were drilled to produce cylindrical specimens with 0.5 cm diameter. Figure 3-3 shows some of the shapes and sizes of synthesized PUR samples.

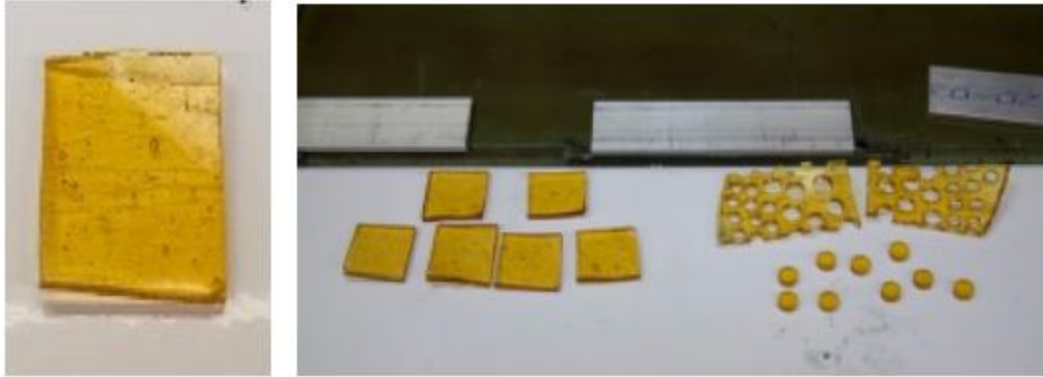


Figure 3-3: Cut 2x2 cm square samples and drilled 0.5 cm diameter samples pre-irradiation.

3.2 MU Samples

3.2.1 Pre-polymers

11 different PUR samples were synthesized at the University of Missouri with varying characteristics. A synthesis similar to that shown in Figure 3-1 was followed, using PTMEG with varying molar ratios, an aromatic and aliphatic curing agent, and varying the ratio of pre-polymer A with pre-polymer B for each sample. The overall synthesis is given in Figure 3-4 comparing the aliphatic versus aromatic PURs.

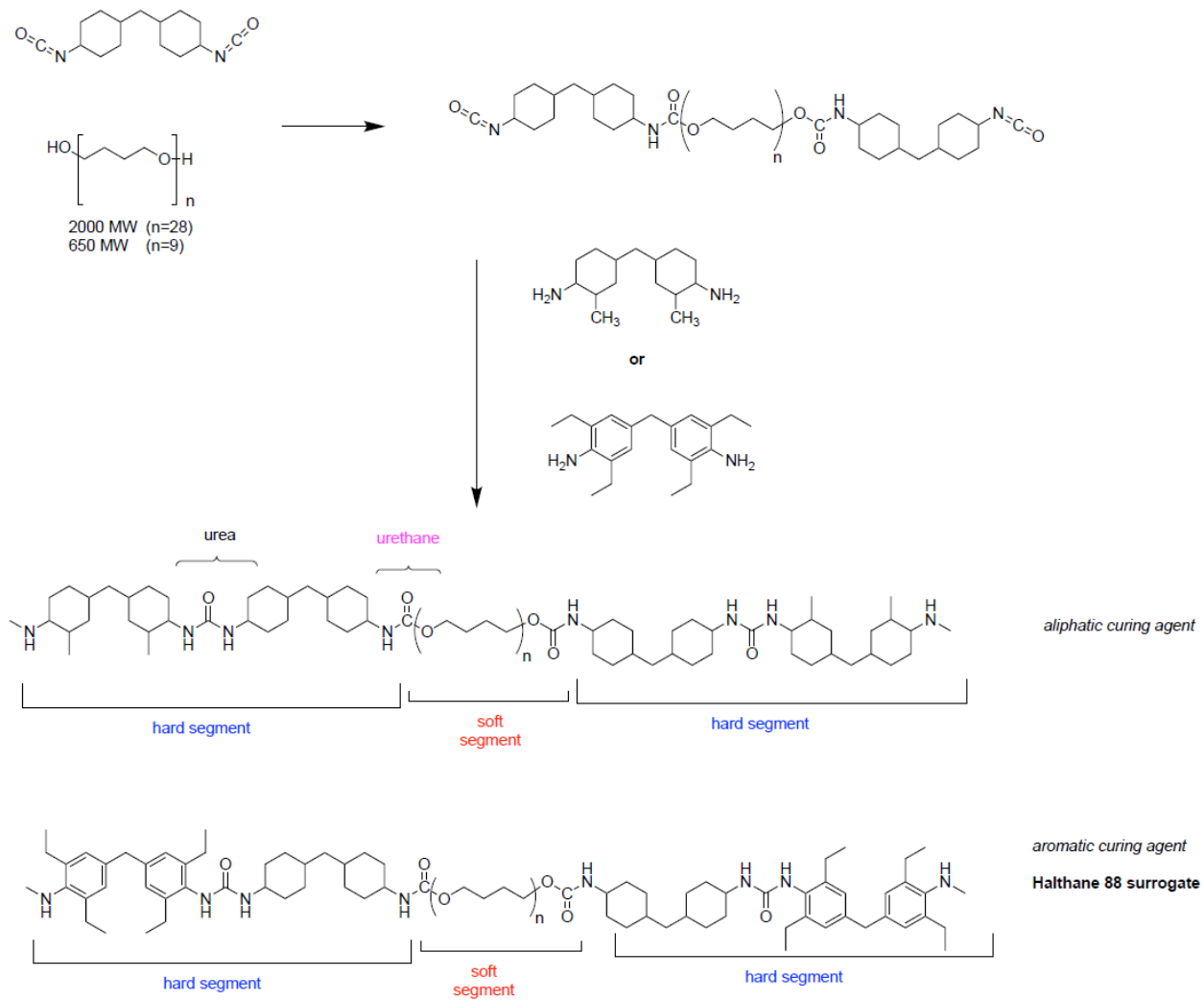


Figure 3-4: Synthesis of University of Missouri PUR samples.

Pre-polymer A was synthesized at the University of Missouri whereas for the samples produced at Y-12 Halthane 88 was obtained directly from the Kansas City National Security Campus. The pre-polymer was still comprised of the aliphatic Diisocyanate $H_{12}MDI$ and PTMEG, but allowed for the molar ratio of PTMEG to be varied between samples. The full procedure for synthesizing pre-polymer A using 650 and 2000 molecular weight PTMEG can be found in the Appendix. Additionally, pre-polymer B was comprised either solely of 4,4'-methylenebis(2,6-diethylaniline) for the aromatic PUR samples, or 4,4'-methylenebis(2-methylcyclohexan-1-amine) for the aliphatic PUR samples. All chemicals were obtained from Sigma Aldrich and were used without further purification.

3.2.2 Procedure

Dr. C.W. Littlefield performed the synthesis of the MU samples at the MURR following a similar procedure to the one used at Y-12. Pre-polymers A and B were thoroughly mixed and then pressed into 3.20 mm thick sheets using Teflon plates and shims. Dow Corning high-vacuum silicone grease was used to prevent the adhesive from sticking to the Teflon plates and ensure no trace Fluorine would be transferred to the samples. As before, certain samples were prepared under atmospheric conditions while others were degassed prior to mixing with a Schlenk line and vacuum desiccator with collar. After allowing the PUR sheets to cure overnight, the samples were gently wiped with hexane to remove any residual silicone grease. The samples were then cut into 12x12 mm specimens to be irradiated. To prevent the samples from being directly taped

to the stand and to reduce potential contamination during irradiation, all the PUR samples were wrapped in a single layer of aluminum foil as shown in Figure 3-5.



Figure 3-5: PUR samples wrapped in aluminum foil prior to irradiation.

Aluminum foil was selected because it will not degrade during irradiation and will have a negligible effect on the delivered dose to the samples. Table 3.1 lists the 11 synthesized samples with different production characteristics.

Table 3.1: PUR samples synthesized at the University of Missouri.

Sample	ATM vs DG	PTMEG M_n	Pre-polymer B	Weight Ratio
1	DG	650	aromatic	3.6:1.0
2	DG	650	aromatic	2.6:1.0
3	ATM	650	aromatic	3.5:1.0
4	ATM	650	aromatic	2.3:1.0
5	ATM	2000	aromatic	5.0:1.0
6	DG	2000	aromatic	5.0:1.0
7	DG	2000	aromatic	7.3:1.0
8	ATM	2000	aromatic	7.3:1.0
9	ATM	2000	aliphatic	5.6:1.0
10	ATM	650	aliphatic	3.3:1.0
11	ATM	650	aliphatic	4.7:1.0

An aliphatic Pre-polymer B was selected with the expectation that it would result in a decrease in radiation resistance. Specifically, the hard segment was expected to become more susceptible to radiolysis as the aromatic units determine its stability. Varying weight ratios were used to evaluate how varying concentrations of hard and soft segments influenced the stability and to better isolate degradation of the individual segments. Employing a polyol with an average molecular weight of 650 is expected to increase stability, as it limits overall range of motion. Only atmospheric samples were synthesized using the aliphatic curing agent due to its low boiling point relative to the temperature required for degassing. It is worth noting that when mixed with pre-polymer A, the aliphatic pre-polymer B rapidly begins to cure and may likely be less homogeneous than samples 1-8.

Chapter 4 MURR: GE PETtrace Cyclotron

4.1 Operational Specifications

4.1.1 Schematics

The University of Missouri Research Reactor (MURR) relies on a GE PETtrace Radiotracer Cyclotron to produce various isotopes to be distributed to hospitals in the region for medical imaging purposes. Depending on the isotope of interest, either negatively charged hydrogen ions or negatively charged deuterium ions are accelerated in an outward spiral path while being confined by an average magnetic field of 1.2 Tesla. The ions are initially extracted from an internal Penning Ion Gauge discharge source fixed in the middle of the cyclotron system. A schematic of the GE PETtrace cyclotron is given below in Figure 4-1.

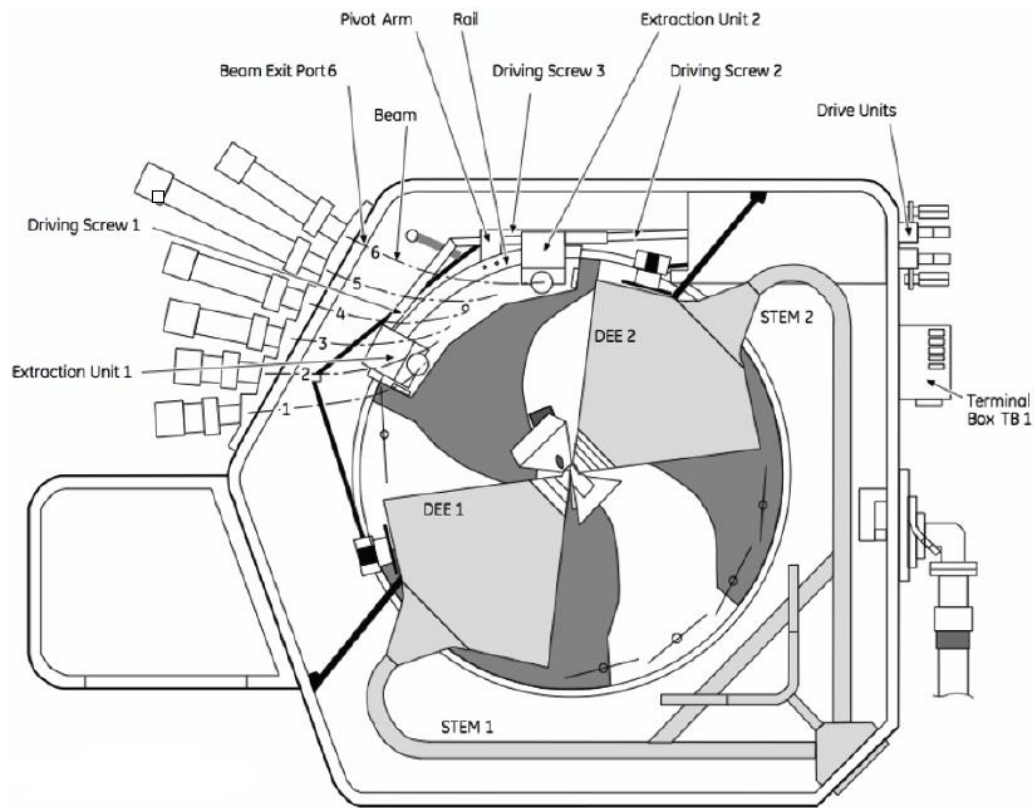


Figure 4-1: Schematic of GE PETtrace cyclotron [22].

A beam extraction can be initiated at two points, labelled Extraction Unit 1 & 2 in Figure 4-1, allowing for simultaneous irradiation of two targets. At these positions, carbon foils are used to strip the electrons off the accelerated ions, converting them into protons. This change in the polarity of their charge reverses the original confining magnetic field force, to now function as a steering force onto one of six particular targets. MURR utilizes the single mode extraction system only.

As part of General Electric's PETtrace 800 cyclotron series, the system functions as a fixed-energy isochronous cyclotron. This technique allows a greater beam current to be produced by relying on an increasing magnetic field with radius. MURR's PETtrace 860 cyclotron is capable of providing a proton or deuteron beam with energy of 16.5 or

8.4 MeV, respectively. The 44,000 lb. system can produce up to a 100 μA proton beam or 60 μA deuteron beam. As the majority of MURR's production utilizes a 16.5 MeV proton beam with a current ranging between 38-72 μA , this will be the focus throughout this thesis.

4.1.2 Vault & Target Assembly

The entire cyclotron system measures 1330 mm in length, 1200 mm wide and 1910 mm tall. The compact accelerator must be housed within a vault to provide adequate shielding from the ionizing radiation created by both its direct operation and following irradiation of various targets. Typical vaults are made of ordinary steel reinforced concrete ranging from 1.5-2.2 m thick walls with 20-40 cm of the inner wall capable of being easily removed and treated as radioactive waste if necessary [23]. The main penetration into the MURR cyclotron vault follows industry guidelines and makes use of a common "S shaped" penetration.

While capable of producing an array of radionuclides, fluorine-18 is the most commonly produced radiotracer at MURR. As shown in Equation 2.2, this is achieved via the proton bombardment of a 95% enriched oxygen-18 water target. The ensuing (p,n) reaction produces fluorine-18 which is then delivered in water and under a carrier gas of helium to an automated FDG synthesis module. A few important cyclotron characteristics affecting the production of fluorine-18 are the proton beam energy and current being used, target volume, and beam size and profile. This allows for optimal production depending on demand and projected runtime. The proton beam has a

diameter of approximately 10 mm with an elliptical shape and Gaussian distribution profile. The beam profile is reasonably uniform which is in part due to the system being a negative ion cyclotron system. Figure 4-2 shows the size and profile associated with the MURR cyclotron beam using burn paper.

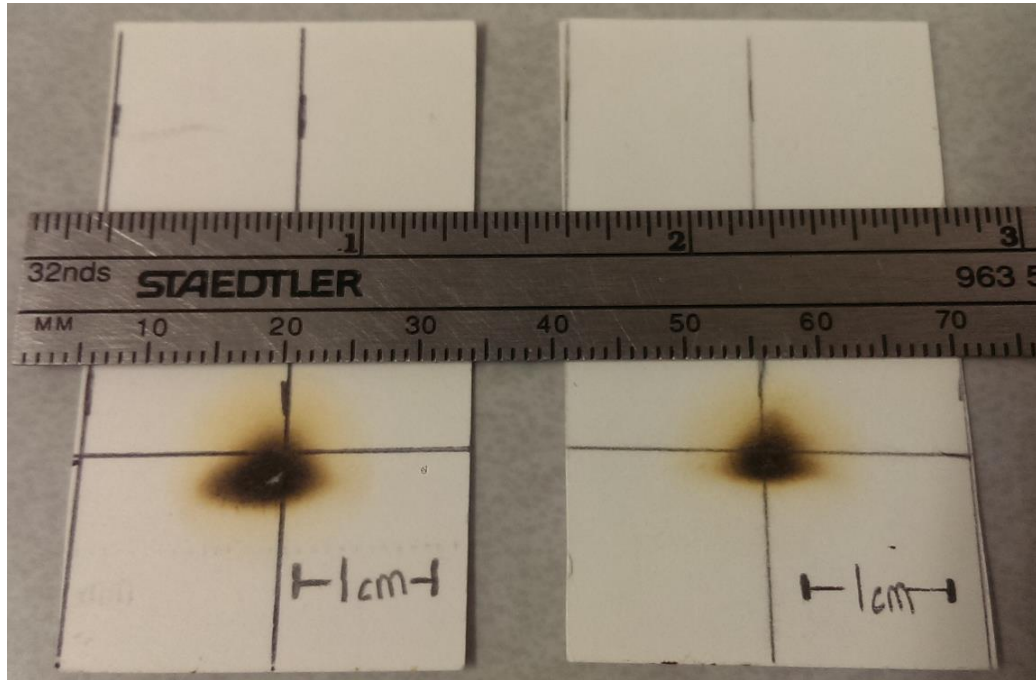


Figure 4-2: Beam profile of MURR PETtrace 860 cyclotron.

Like any radioisotope production facility, the MURR occasionally replaces or upgrades its target assemblies in order to improve overall efficiency and operating costs associated with fluorine-18 production. While an external target system containing enriched water is always used, the construction and material used as the target holder is unique to each manufacturer. Tantalum and niobium target chambers, for example, are more reactive, resulting in higher FDG yields compared with titanium or silver target chambers. The expected maintenance associated with a particular material is another

important consideration; as certain target materials, like silver, can be more susceptible to corrosion.

Currently, two target assemblies are used regularly at MURR and these will be the focus of this thesis. The first is the TS-1650P target from Bruce Technologies, shown below in Figure 4-3.



Figure 4-3: Target assembly by Bruce Technologies for fluorine-18 production.

The target is designed to maximize fluorine-18 production with a single beam current up to 100 μ A while minimizing enriched water costs during operation. The body of the target is made of aluminum and is composed of three blocks that screw together. The enriched water target chamber is housed in a niobium insert located within these blocks and is shown below in Figure 4-4.



Figure 4-4: Niobium insert (left) and Havar foil (right) used in the target chamber.

The chamber holds 3.5 mL of the enriched water target and is held under high pressure with a Havar foil that seals the entrance of the high-pressure water target chamber. A Havar foil prior to irradiation is shown above in Figure 4-4. The 50 μm thick Havar window is exposed to high levels of radiation and being an alloy of cobalt, chromium, iron, nickel, manganese, tungsten, and molybdenum is susceptible to producing an array of activation products.

The second target assembly currently being used at MURR is the P5230 fluorine-18 high yield target assembly by GEMS PET Systems AB. Similar in construction, it consists of three aluminum blocks with a pressurized target chamber within. The chamber is constructed from silver and holds 1.5 mL of the enriched water target and generally operates at a lower beam current of approximately 38 μA . A 50 μm thick Havar window is again used to form the high pressure water target seal, while an

additional 25 μm thick Havar window is used for cooling and to keep the beamline pressurized under helium prior to bombardment of the target.

4.1.3 Neutron Production Considerations

The main purpose of the shielding around a cyclotron is to reduce the overall gamma and neutron flux generated during routine operation. According to international guidelines, the thickness and composition of the various shielding mechanisms should be based on maximum neutron fluxes generated during production as high energy neutrons can be particularly problematic [24]. The interactions of the 16.5 MeV protons with the oxygen-18 enriched water target, given in Equation 2.2, and with the various cyclotron and target components within the beam line are responsible for generating the high intensity radiation field. The neutron production generated from both target assemblies during routine operation at MURR will be considered for this thesis.

One significant target assembly component subject to activation is the Havar film used to seal the high-pressure target chamber. Engineered specially for beam line windows in GE PETtrace cyclotrons, the thin films can withstand the high pressure differential between the target chamber and cyclotron vacuum. Circulating helium gas is used to cool the Havar foils as the proton bombardment causes high temperatures near the target. Table 4.1 lists the composition of the Havar alloy along with a few probable reactions with neutron by-products.

Table 4.1: Elemental composition of Havar foil with probable modes of activation producing neutrons.

Elemental Composition	Probable Reactions
Cobalt (42%)	$^{59}\text{Co}(n, 2n)^{58}\text{Co}$
Chromium (19.5%)	$^{50}\text{Cr}(n, p2n)^{48}\text{V}$
	$^{52}\text{Cr}(n, 2n)^{51}\text{Cr}$
	$^{52}\text{Cr}(p, n)^{52}\text{Mn}$
	$^{54}\text{Cr}(p, n)^{54}\text{Mn}$
Iron (19%)	$^{54}\text{Fe}(n, p2n)^{52}\text{Mn}$
	$^{56}\text{Fe}(p, n)^{56}\text{Co}$
	$^{57}\text{Fe}(p, n)^{57}\text{Co}$
	$^{58}\text{Fe}(p, n)^{58}\text{Co}$
Nickel (13%)	Proton, alpha by-products
Tungsten (3%)	$^{183}\text{W}(p, n)^{183}\text{Re}$
	$^{184}\text{W}(p, n)^{184}\text{Re}$
Manganese (1.5%)	$^{55}\text{Mn}(n, 2n)^{54}\text{Mn}$
Molybdenum (2%)	Gamma by-product

As the Havar foil is positioned immediately in the beam line, it will be directly exposed to the high energy protons required for various neutron emitting transfer reactions. Also included in Table 4.1 are reactions involving neutron activation as the Havar foil will be subjected to a large flux of secondary neutrons produced from the fluorine-18 production.

4.2 MCNP Model of Neutron Flux Spectrum

4.2.1 Input File Structure

MCNP6 version 1.0 was used to estimate the neutron flux spectrum at various points around the targets of the GE PETtrace cyclotron at MURR during routine production of fluorine-18. The model includes the target assemblies, the areas of interest immediately surrounding the targets, and considers the 16.5 MeV proton beam as it impinges on the initial Havar foil in each target assembly.

Precise geometrical measurements of the TS-1650P target from Bruce Technologies and the P5230 fluorine-18 high yield target assembly by GEMS PET Systems AB were taken and are given below in Table 4.2.

Table 4.2: Measurements of Bruce and GE target assemblies.

Assembly Part	Length (cm)	Width (cm)	Depth (cm)
Bruce Block A	10.6	5.6	4.6
Bruce Block B	7.6	5.6	3.0
Bruce Block C	7.6	5.6	1.9
GE Block A	10.8	5.7	3.3
GE Block B	7.0	5.7	2.1
GE Block C	6.4	5.7	1.9

The proton beam is defined using a general source definition, or SDEF, that positions a mono-directional reference vector in the center of the beam line. Protons with energy of 16.5 MeV are given a Gaussian distribution with a 0.4 and 0.2 cm width at half maximum, in length and width respectively. The beam width is also given an average position of 0.4 cm below the reference, in order to better align with the beam profile shown in Figure 4-2.

Monte Carlo code uses tally cards to specify what information is needed from the simulation. As we are presently interested in the neutron flux, the track length estimate of cell flux (F4) and flux at a point (F5) tallies will be employed. Both will return an output that represents the neutron fluence, with units of particles per centimeter squared, for the location specified. The tallies are normalized to the proton beam current by multiplying each tally by the number of protons present per second.

To specify the materials required for the MCNP calculation, a unique material number with a corresponding isotopic composition is needed for each. Geometries defining the two target assembly blocks are therefore filled with aluminum, while the target chambers are constructed with niobium and silver for Bruce and GE, respectively. The material specification for Havar foil, as structured for the input file, is given below in Figure 4-5.

```

m3      27059.          0.42  $ havar foil
        24050.          0.00847275 24052.          0.1633886 24053.          0.01852695
        24054.          0.00461175 28058.          0.08645766 28060.          0.03330334
        28061.          0.001447673 28062.          0.004615815 28064.          0.001175512
        74180.          3.24e-005 74182.          0.007155 74183.          0.0038637
        74184.          0.0082728 74186.          0.0076761 42092.          0.0032494
        42094.          0.0020306 42095.          0.003498 42096.          0.0036696
        42097.          0.0021032 42098.          0.0053218 42100.          0.0021274
        25055.          0.016 6012.          0.0019786 6013.          2.14e-005
        26054.          0.01116395 26056.          0.1752501 26057.          0.00404729
        26058.          0.00053862

```

Figure 4-5: Isotopic material specification of Havar foil.

Complimentary to Table 4.1, the elemental composition of Havar is given along with the isotopic composition for each element. The first, third, and fifth columns in Figure 4-5 correspond to the specific isotope of interest while the second, fourth, and sixth columns show the corresponding contribution of each.

4.2.2 Experimental Data vs. Physics Models

MCNP6.1 utilizes the ENDF/B-VII.1 data library. A cross-section directory file, or XSDIR, organizes and reads all the stored cross-sectional data. In order to be accessed by the XSDIR the initial data must be processed, using NJOY, into a compact ENDF format, or ACE-formatted data file. In addition to the ENDF/B-VII.1 data library, there are numerous others including JEFF (Europe), JENDL (Japan), CENDL (China), ROSFOND (Russia), TENDL (Netherlands/France), IRDF (International), and EXFOR (International). Due to the complexity of processing tools, like NJOY, not all of the data files from these sources are available in the MCNP ACE-format in which case MCNP relies on models to simulate interactions.

Both experimental library data and predictive models built-in to the MCNP6 software were considered in calculating the neutron flux spectrum produced by the $^{18}\text{O}(p,n)^{18}\text{F}$ reaction. Figure 4-6 compares different cross sections for this reaction.

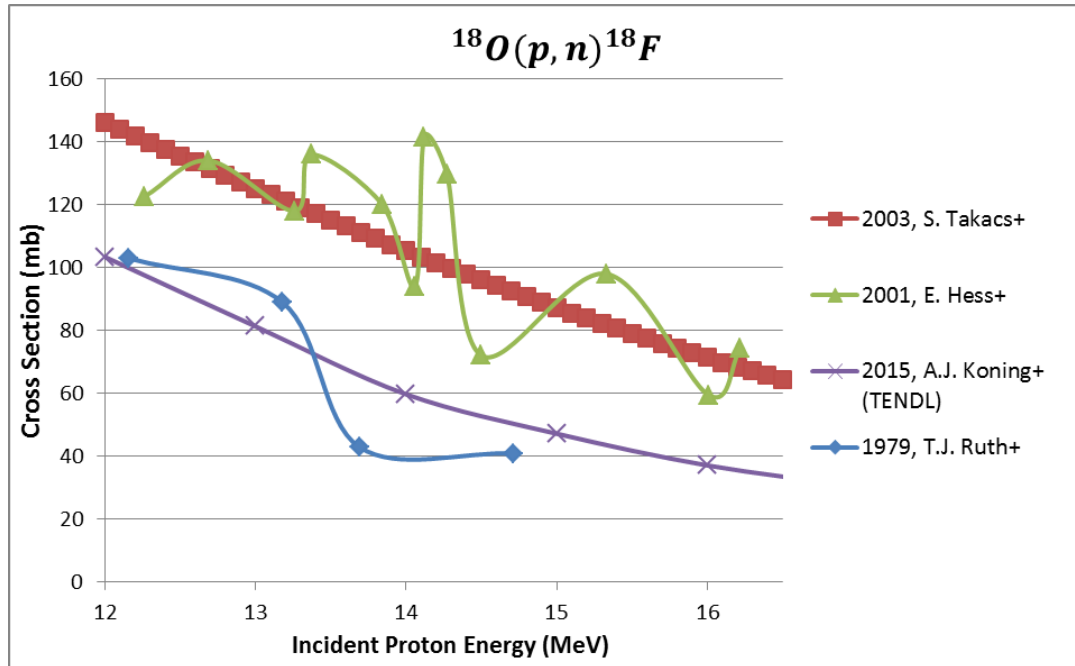


Figure 4-6: Cross section curves for the oxygen-18 (p,n) reaction [25].

In Figure 4-6, E. Hess+ (green) and T.J. Ruth+ (blue) represent original experimental data, while S. Takacs+ data (red) was calculated using fitting procedures combining numerous experimental data sets. The A.J. Koning+ data (purple) is the output of the TALYS nuclear model code system. The calculated fit by S. Takacs+ is the recommended data by the International Atomic Energy Agency (IAEA) [25]. Unfortunately, while this data is available in the computerized database EXFOR, it is not accessible in the MCNP required ACE-format. For this reason, the TENDL nuclear data library was employed for the cross section associated with the oxygen-18 (p,n) reaction. Officially joining the IAEA's collection of evaluated data files in 2017, the 2015 TALYS based data library is unique in that it relies on simulations versus strictly experimental measurements. However, unlike other predictive models, the robust output is provided as a complete data library which can then be processed into ACE-format.

In addition to oxygen-18, TENDL-2015 cross sections were used for calculating the proton activation of the Havar foil components, as these files were also absent from the ENDF/B-VII.1 data library. Calculations of the neutron flux spectrum are compared using these data libraries and the built-in physics models within the MCNP software. There are numerous models available with MCNP6, each used to define unique parameters to best simulate the particle transport for a specific application. The Bertini, CEM03.03, and INCL4 physics models were considered and the neutron flux spectrum from each model was compared. In MCNP6, CEM03.03 is the default option while combination, or “mix and match” settings between physics/data tables are frequently employed. For example, LAHET physics and code system is used for various transport calculations for nucleons and pions within MCNP, including differential particle production cross sections. This means when physics models are used to transport protons in the model, LAHET physics can use either the Bertini intranuclear cascade, CEM, or INCL model. The influence of these models on the neutron flux during routine fluorine-18 production at MURR is given below in Figure 4-7.

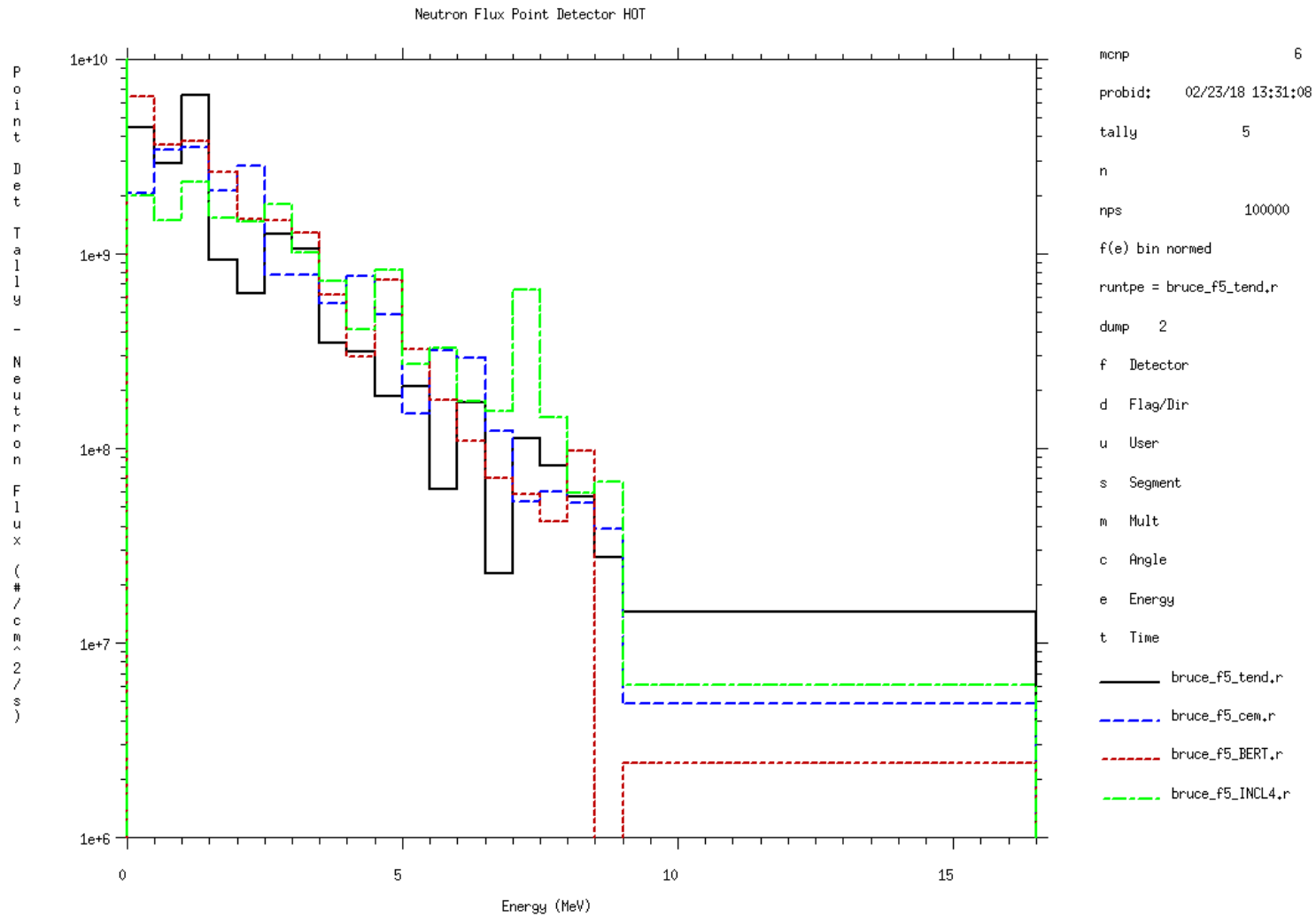


Figure 4-7: Neutron flux 3 inches from target using TENDL (black), CEM (blue), BERTINI (red), and INCL4 (green).

Figure 4-7 is a plot of the neutron flux emitted by the Bruce TS-1650P target assembly with a 63 μA beam and is created using the MCNPLOT plotting function within MCNP with XMING Window System display server. The neutron production from both oxygen-18 and Havar are considered, with neutron contributions from both being simulated by the respective model. The “hot” position is positioned directly on top of the Bruce target assembly, at a distance of 3 inches from the water target being irradiated. Figure 4-8 shows where the 3 inch irradiation position is located on the target assembly, which represents the highest neutron flux exposure possible as it sits directly atop the water target.

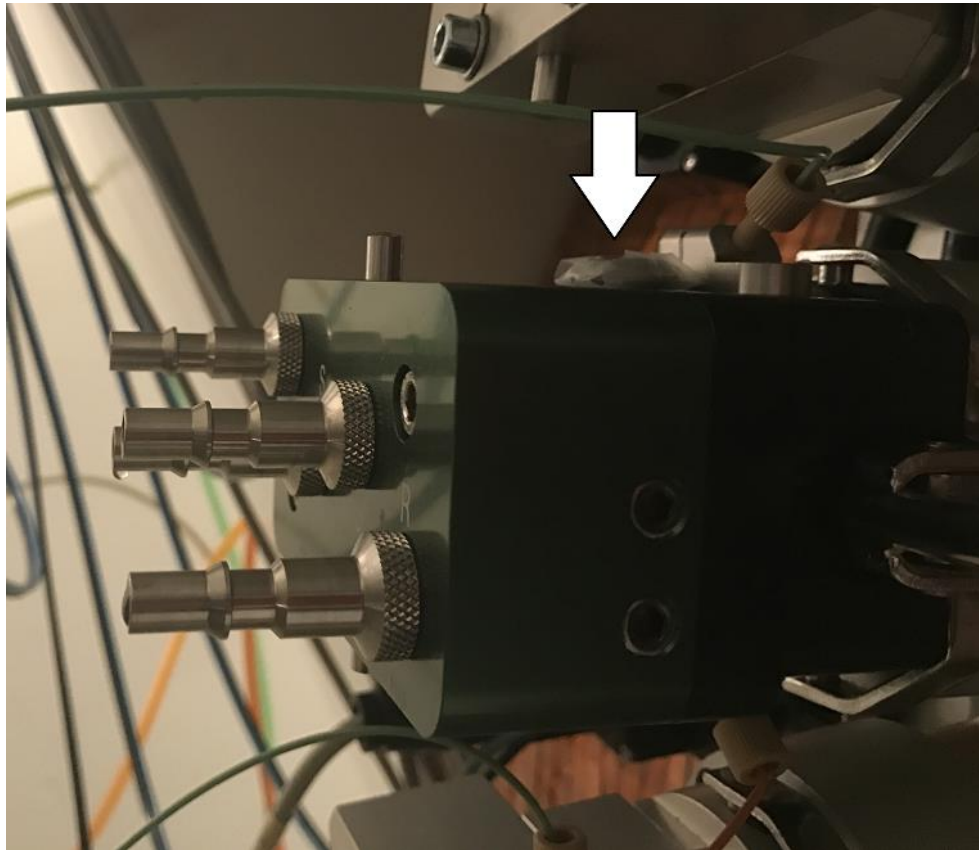


Figure 4-8: The 3 inch, “hot” irradiation position on the Bruce target assembly.

Though unique to each physics model, the simulation runtime and relative MCNP error is comparable for all the models. The total runtime and calculation uncertainty with these input parameters is given below in Table 4.3.

Table 4.3: Simulation runtime and calculation uncertainty for TENDL, CEM.03, BERTINI, and INCL models.

Physics Model	Runtime (hours)	MCNP Uncertainty
TENDL	24.32	0.0060
CEM.03	24.11	0.0058
BERTINI	24.06	0.0050
INCL	24.10	0.0054

In order to better compare the neutron flux calculated from TENDL and the three physics models, Table 4.4 presents each model's calculated neutron flux along with the relative change compared to TENDL.

Table 4.4: Comparison of TENDL neutron flux to CEM, BERTINI, and INCL models for Bruce target assembly at the 3 inch position.

Energy Bin (MeV)	TENDL	CEM.03	% Change	BERTINI	% Change	INCL	% Change
0.00	3.84E+07	2.56E+07	-33%	6.55E+07	70%	3.37E+07	-12%
0.50	1.37E+09	1.33E+09	-3%	2.96E+09	116%	1.64E+09	20%
1.00	1.01E+09	1.11E+09	10%	2.21E+09	119%	1.32E+09	30%
1.50	8.82E+08	9.78E+08	11%	1.62E+09	84%	1.01E+09	14%
2.00	7.12E+08	7.84E+08	10%	1.14E+09	59%	7.94E+08	11%
2.50	5.34E+08	6.57E+08	23%	7.91E+08	48%	6.28E+08	18%
3.00	4.21E+08	5.37E+08	28%	5.52E+08	31%	5.10E+08	21%
3.50	3.79E+08	4.33E+08	14%	4.08E+08	8%	4.13E+08	9%
4.00	3.10E+08	3.67E+08	18%	3.08E+08	-1%	3.45E+08	11%
4.50	2.41E+08	2.91E+08	21%	2.23E+08	-8%	3.05E+08	26%
5.00	1.97E+08	2.32E+08	18%	1.64E+08	-17%	2.51E+08	27%
5.50	1.60E+08	1.72E+08	8%	1.15E+08	-28%	2.06E+08	29%
6.00	1.15E+08	1.55E+08	35%	8.55E+07	-26%	1.80E+08	57%
6.50	1.01E+08	1.06E+08	4%	6.26E+07	-38%	1.42E+08	40%
7.00	8.48E+07	7.11E+07	-16%	4.37E+07	-48%	1.22E+08	43%
7.50	6.43E+07	5.78E+07	-10%	3.45E+07	-46%	9.20E+07	43%
8.00	6.07E+07	4.16E+07	-31%	3.41E+07	-44%	6.89E+07	13%
8.50	4.57E+07	2.99E+07	-34%	2.44E+07	-47%	6.30E+07	38%
9.00	2.95E+07	1.73E+07	-41%	1.56E+07	-47%	3.73E+07	26%
16.50	6.99E+07	4.13E+07	-41%	4.64E+07	-34%	1.14E+08	63%
Total	6.82E+09	7.44E+09	9%	1.09E+10	60%	8.27E+09	21%

In Table 4.4, the neutron flux for each of the 20 energy bins, as well as the overall total, is given in units of number of particles per centimeter squared per second with 100 million particles being simulated. The input file for the TENDL simulation for the 3 inch position placed directly on the Bruce target assembly can be found in the Appendix. The CEM.03, BERTINI, and INCL input files are similar only with the cross section cards removed and the appropriate physics model call out.

4.2.3 MCNPX Visual Editor: Particle Simulations

The Visual Editor Code is designed to assist users in creating, displaying, and validating MCNP input files. Model parameters, including geometry, source terms, material definitions, and specified tallies can be set up and modified directly from the plot window within The Visual Editor. The Bruce target assembly, with the 3 inch irradiation position, is represented in the Visual Editor as the following cross sectional plots.

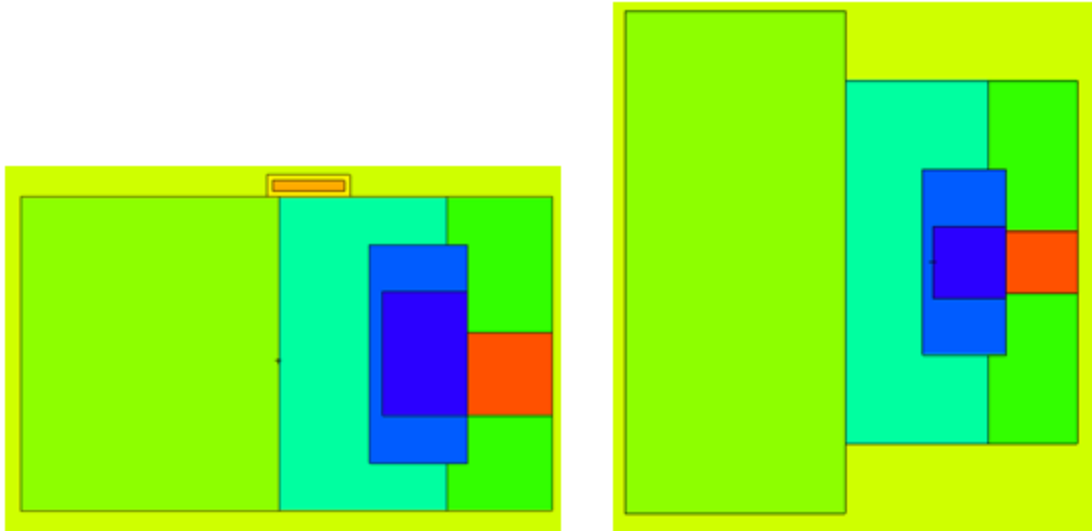


Figure 4-9: Bruce target assembly plotted in X-Z (left) and X-Y (right) planes with colored cells as modeled by The Visual Editor.

In Figure 4-9, each cell, or part of the Bruce target assembly, is represented by a different color. For example, the red represents the vacuum within the aluminum body in which the beam line travels while the dark blue represents the oxygen-18 enriched water target. Figure 4-10 shows the MCNP model of both Bruce and GE target assemblies with the four calibrated irradiated positions at 3, 4.4, 9, and 14 inches as measured from the Bruce water target.

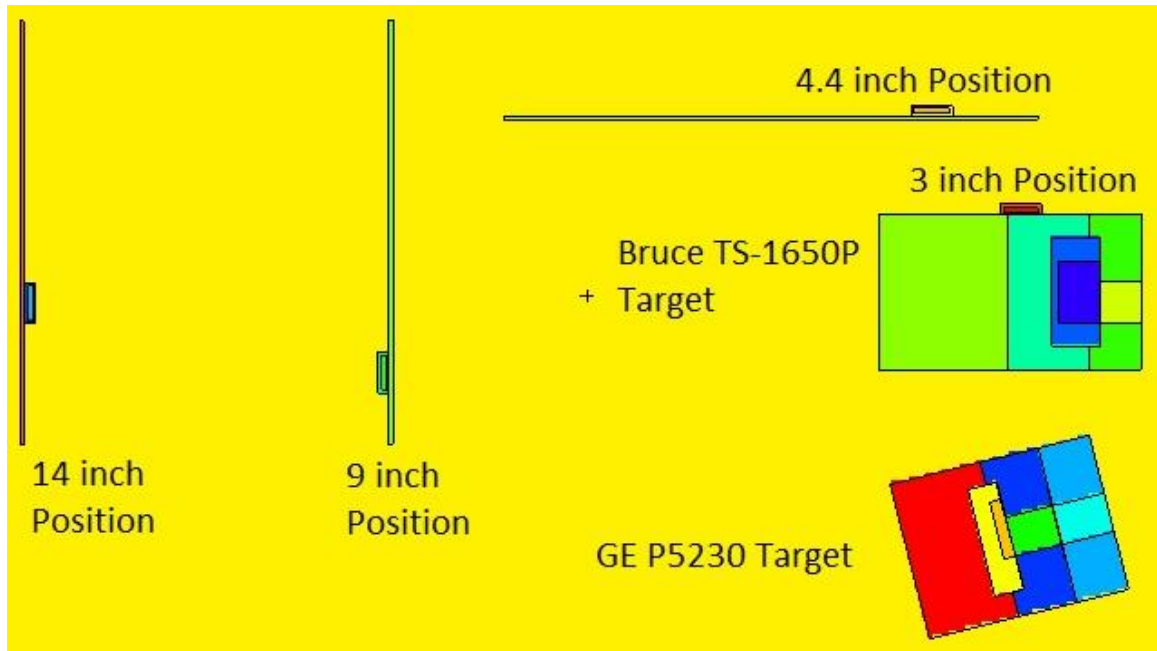


Figure 4-10: MCNP model of the Bruce and GE target assemblies and calibrated irradiated positions as represented by The Visual Editor.

In Figure 4-10, each of the four irradiation positions is modeled by placing a Cadmium cap at the measured distance and tallying the neutron flux inside the cap. While the cap at the 3 inch position sits directly atop the Bruce target, the remaining three caps are secured to Lucite plates supported by a specially constructed polyvinyl chloride stand. The Visual Editor can also be used to view three dimensional plots of the MCNP input using the built-in Dynamic 3D display functionality. A 3D image of the two target assemblies is given below in Figure 4-11.

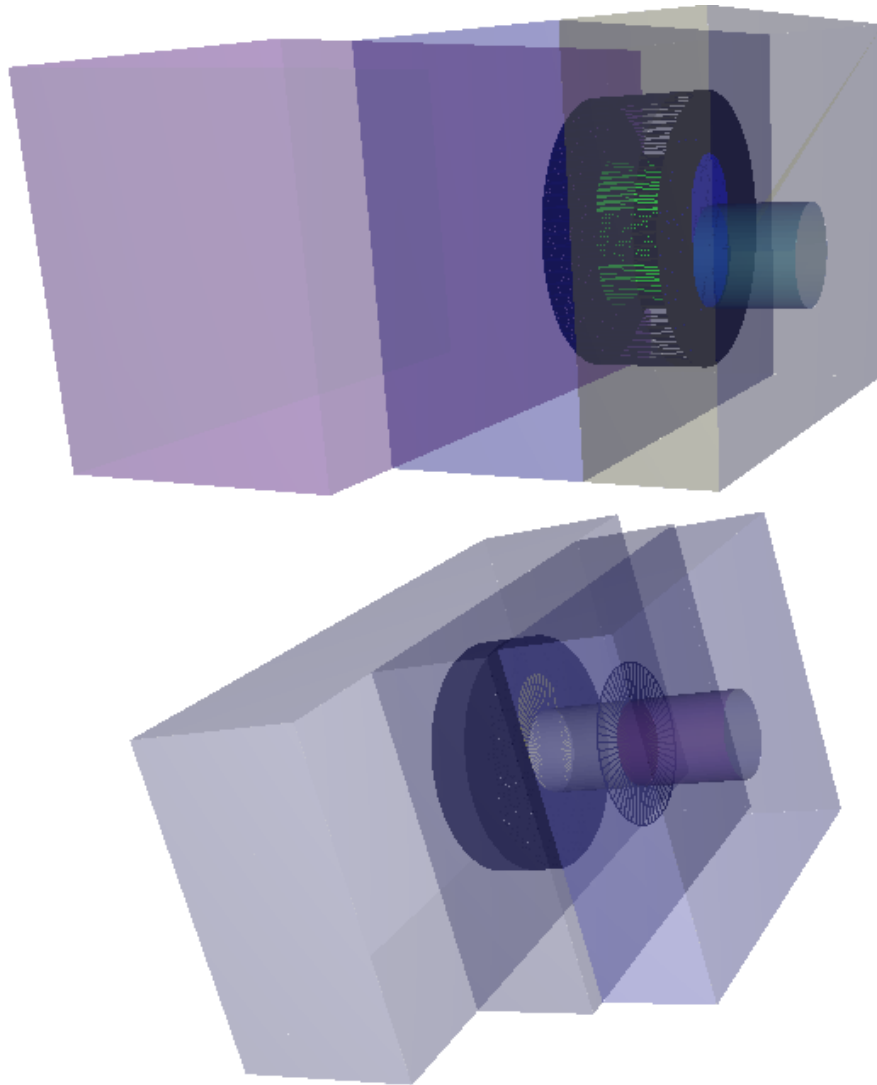


Figure 4-11: 3D image of Bruce (top) and GE (bottom) target assemblies generated using The Visual Editor Code.

Figure 4-11 shows the path of the beam line through the aluminum blocks until it strikes the enriched water target. For the Bruce target assembly, the green oval represents the enriched water target, while the blue sphere represents the thin Havar foil.

The Visual Editor is also useful for particle track plotting. This functionality allows for initial source plotting of the system and the subsequent tracking of simulated particles, both source and emitted, through their various nuclear transport. Figure 4-12

shows a particle track plot simulating 1.0×10^4 protons striking the water target within the Bruce target assembly and the resulting emission of neutrons.

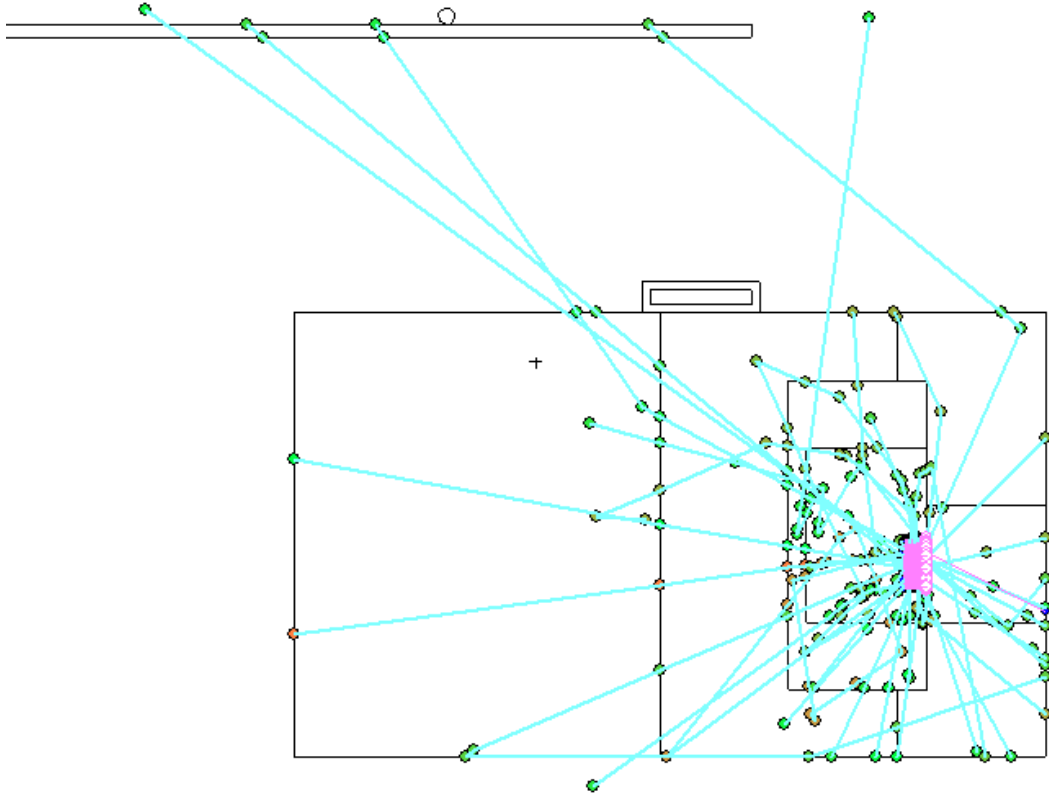


Figure 4-12: Particle track plot simulating 1.0×10^4 protons striking the water target in the Bruce target assembly.

Figure 4-12 shows proton tracks in pink, neutron tracks in teal, low energy neutrons in orange and high energy neutrons in green. Simulating 1.0×10^4 protons, the lowest energy neutrons were 4.25×10^{-5} MeV, while the highest energy neutrons observed were 7.16 MeV. The above simulation considers particles emanating from the specified source, contributing to a tally, experiencing a collision, or crossing a surface.

Particle plotting is also a helpful feature when studying the beam profile defined in the model. Figure 4-13 shows a MCNP beam source plot for the GE PETtrace cyclotron at MURR with 1.0×10^4 protons simulated.

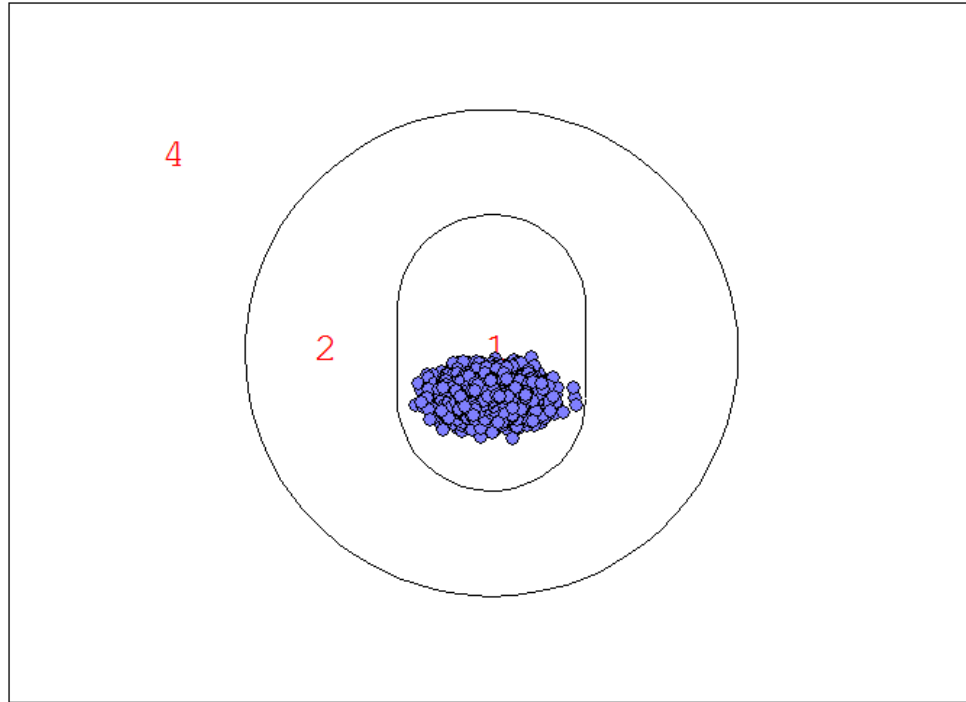


Figure 4-13: Beam profile of MURR's GE PETtrace cyclotron as modeled by MCNP.

Figure 4-13 shows an elliptical shape and Gaussian distribution profile which matches closely with the measured beam profile given in Figure 4-2 using burn paper. The protons will eventually strike the enriched water target, labeled 1 above, and cause neutrons to be emitted outward into the niobium or silver insert and the aluminum target body, labeled 2 and 4, respectively. It is important to note that during routine fluorine-18 production a beam current of up to $72 \mu\text{A}$ is frequently employed for 1-3 hours and results in 4.5×10^{14} protons per second.

4.2.4 Neutron Flux Spectrum

The neutron flux spectrum was calculated using the TENDL nuclear data library. The cross section data is benchmarked to experimental data from EXFOR and validated with statistical integral measurements from JUKO Research. Comparisons of the neutron flux between the TENDL data and CEM.03, BERTINI, and INCL models will also be presented for specific calibration positions. Figure 4-14 shows the neutron flux simulated at the 3 inch irradiation position during fluorine-18 production using the Bruce target with a 63 μA beam.

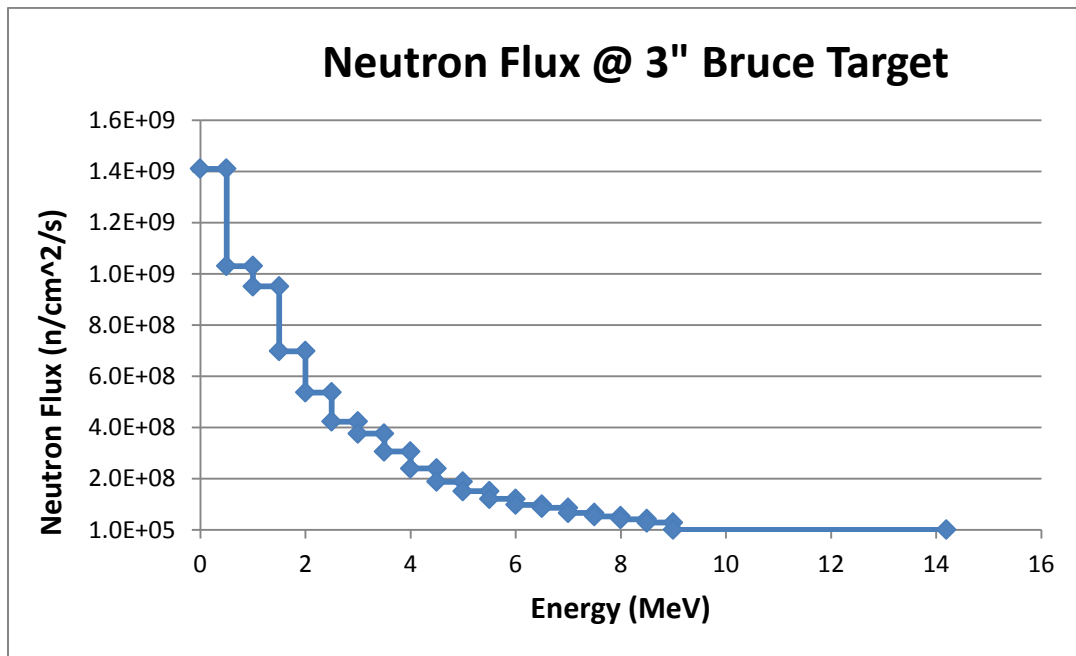


Figure 4-14: Normalized neutron flux at 3" irradiation position during fluorine-18 production using Bruce target.

Figure 4-14 shows the neutron flux spectrum broken down into 19 energy bins beginning at 0.5 MeV. A simulation of 5 million protons, normalized per source particle, found a total neutron flux of 6.8×10^9 neutrons per centimeter squared per second. The

average neutron energy was 2.2 MeV with 47% of the neutrons having energies between 0.5 and 2.5 MeV. Figure 4-15 compares the normalized neutron flux spectrum at the 4.4 inch irradiation position resulting from fluorine-18 production using the Bruce target with a 70 μ A beam and GE target with a 37 μ A beam.

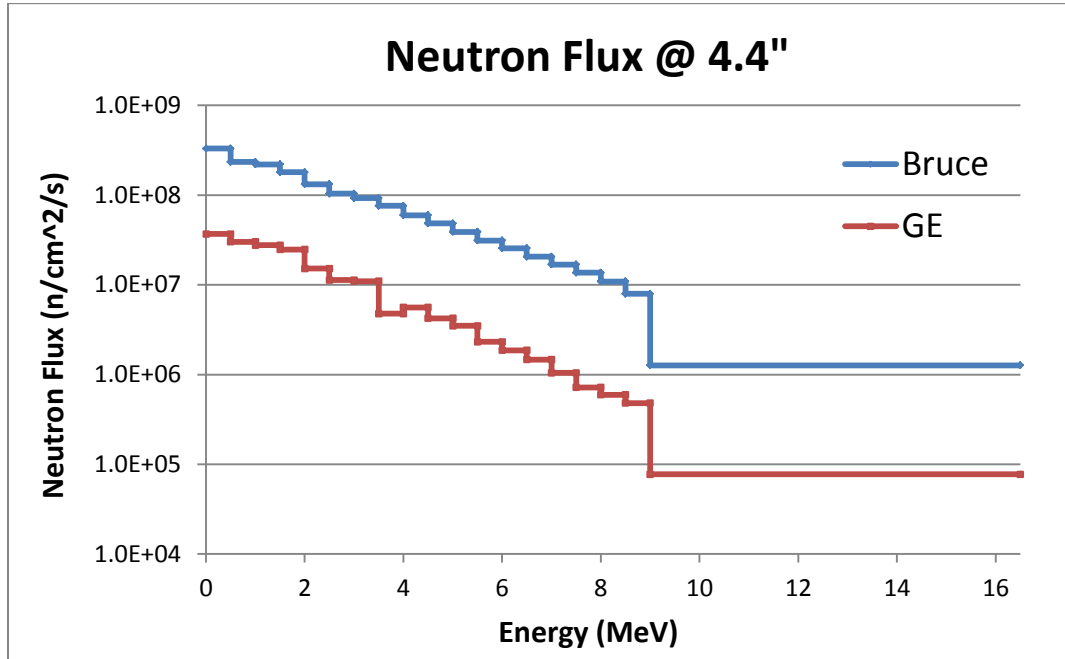


Figure 4-15: Normalized neutron flux at 4.4" irradiation position during fluorine-18 production using Bruce and GE targets.

The results of Figure 4-15 represent two different simulations, one using the Bruce target assembly and the other the GE target assembly, each with 1.0×10^8 protons being transported. Figure 4-16 compares the normalized neutron flux spectrum at the 9 inch irradiation position using the Bruce target with a 70 μ A beam and GE target with a 37 μ A beam.

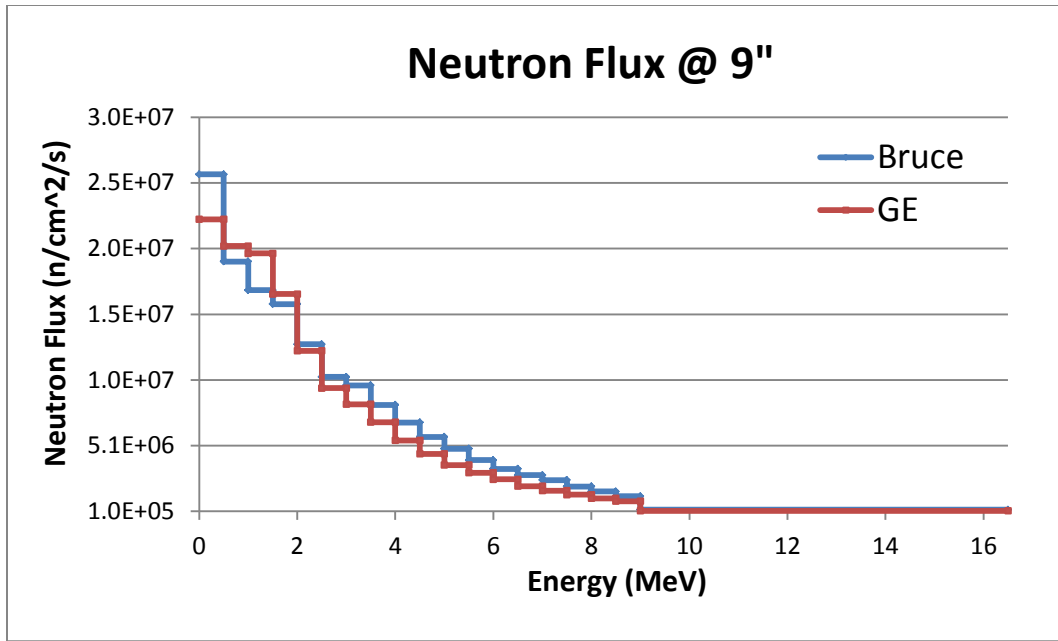


Figure 4-16: Normalized neutron flux at 9" irradiation position during fluorine-18 production using Bruce and GE targets.

Figure 4-17 compares the normalized flux spectrum at the 14 inch irradiation position using the Bruce target with a 70 μA beam and GE target with a 37 μA beam.

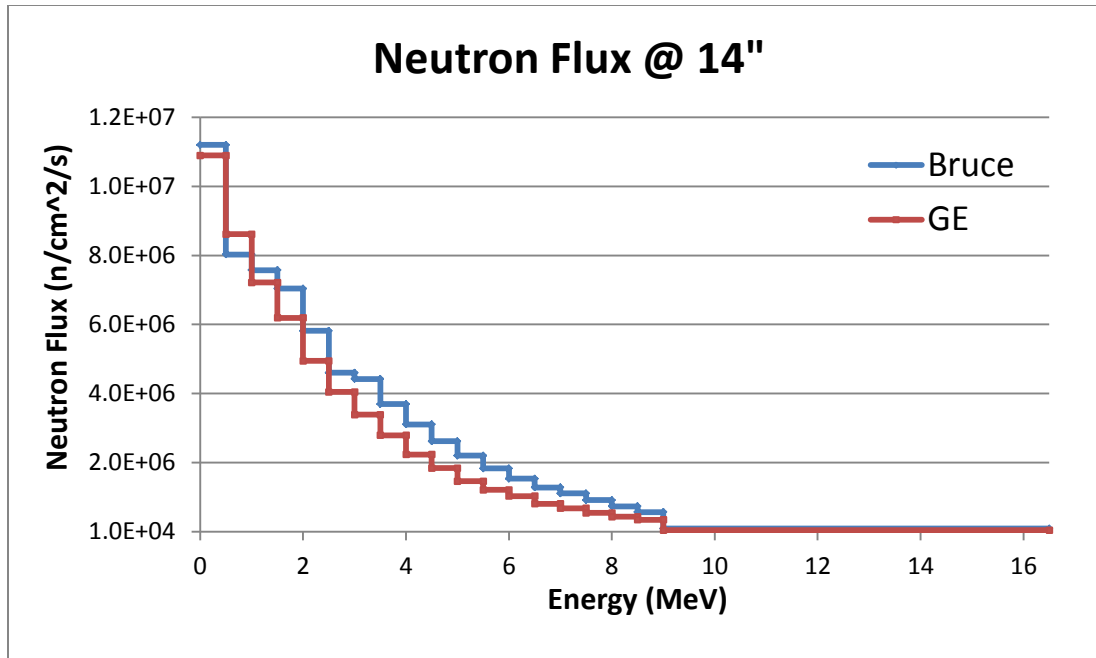


Figure 4-17: Normalized neutron flux at 14" irradiation position during fluorine-18 production using Bruce and GE targets.

The total neutron flux at the 4.4 inch, 9 inch, and 14 inch irradiation positions is given below in Table 4.5.

Table 4.5: Total neutron flux contributions at 4.4, 9, and 14 inch irradiation positions.

	Neutron Flux (n/cm ² /s)		
	4.4"	9"	14"
Bruce Target	1.7E+09	1.6E+08	7.1E+07
GE Target	1.6E+08	1.6E+08	6.0E+07
Total	1.8E+09	3.2E+08	1.3E+08

Table 4.5 shows that the Bruce target accounts for the majority of the flux at the 4.4 inch position, while both the Bruce and GE targets contribute fairly evenly to the 9 and 14 inch positions. This is expected due to the Bruce target assembly being positioned directly in between the GE target assembly and the 4.4 inch position and therefore blocking many of the emitted neutrons from reaching the position.

The reported neutron flux up until this point has been calculated using a F5 tally. This type of tally functions as a ring detector at a specific point on the model and relies on the angular distribution data for produced particles to predict the “next event” in the region of interest. The neutron flux can also be calculated using a F4 tally by summing the track lengths in a particular cell. This method can be useful for scenarios in which there are many tracks in a cell, compared with fewer collisions capable of contributing to the “next event” F5 tally. Table 4.6 compares the neutron flux from a F5 and F4 tally for the 4.4 inch irradiation position using the Bruce target.

Table 4.6: Compared neutron flux calculated using a F5 and F4 tally for the 4.4” irradiation position during fluorine-18 production using the Bruce target.

Energy	F5 Tally	F4 Tally	Difference
5.00E-01	3.31E+08	3.15E+08	-5%
1.00E+00	2.34E+08	2.18E+08	-7%
1.50E+00	2.20E+08	1.86E+08	-15%
2.00E+00	1.80E+08	1.61E+08	-11%
2.50E+00	1.32E+08	1.32E+08	0%
3.00E+00	1.04E+08	1.07E+08	3%
3.50E+00	9.26E+07	8.99E+07	-3%
4.00E+00	7.58E+07	7.84E+07	3%
4.50E+00	5.97E+07	5.40E+07	-10%
5.00E+00	4.84E+07	4.73E+07	-2%
5.50E+00	3.88E+07	3.72E+07	-4%
6.00E+00	3.11E+07	3.48E+07	12%
6.50E+00	2.56E+07	2.47E+07	-4%
7.00E+00	2.06E+07	1.80E+07	-12%
7.50E+00	1.69E+07	1.60E+07	-5%
8.00E+00	1.37E+07	1.17E+07	-14%
8.50E+00	1.09E+07	1.15E+07	5%
9.00E+00	7.93E+06	6.09E+06	-23%
1.65E+01	1.90E+07	1.79E+07	-6%
TOTAL	1.67E+09	1.57E+09	-6%

The F4 simulation uses a surface source file to increase the number of particle tracks modeled at the calibrated position. Table 4.6 shows that the two methods of calculating flux agree closely with one another, with only a 6% difference in the total calculated neutron flux.

4.2.5 MCNP Dose Calculation

Neutron dose was determined using a simplified MCNP model with F4 and F6 tallies and utilized the previously calculated neutron flux at the calibrated positions of interest. The calculated neutron flux spectrum was used as the source in the simplified dose model with the simulated neutrons directed into a cell comprised of typical PUR (54.4% carbon, 12.1% nitrogen, 29.4% oxygen, and 4.1% hydrogen). A constant was found to correlate the results of the F4 in the simplified model with the previously calculated neutron flux spectrum. The results of the F6 energy deposition tally were then multiplied by the correlating constant and give the results in MeV/g. Converting to J/kg, the neutron dose per second for a particular irradiation position. The calculated dose for the 4.4, 9, and 14 inch positions associated with each target assembly is given below in Table 4.7.

Table 4.7: Calculated neutron dose, per second, at 4.4, 9, and 14 inch positions during fluorine-18 production.

Target Assembly	Dose (Gy/s)
Bruce 4.4" Position	2.2E-02
Bruce 9" Position	2.4E-03
Bruce 14" Position	1.1E-03
GE 4.4" Position	2.3E-03
GE 9" Position	2.2E-03
GE 14" Position	9.0E-04

Table 4.7 gives the dose based on standard fluorine-18 production at MURR using a 70 and 37 μ A beam for the Bruce and GE targets, respectively. The 4.4 inch irradiation position will be used as the high dose point while the 9 and 14 inch irradiation positions will give a lower dose points for comparison. Stationary at each position for several weeks, the samples will be exposed to the emitted flux from both Bruce and GE targets during fluorine-18 production.

Two separate irradiation experiments were performed for different PUR materials. The first exposed PUR samples prepared at the Y-12 Nuclear Security Complex to neutron doses ranging between 70 and 5540 Gy, with an additional sample group receiving 6000 Gy of gamma radiation from the Co-60 beam port at MURR. In order to compare the effects from various levels of exposure, the samples were broken into 6 treatment groups, given below in Table 4.8.

The second experiment irradiated various PUR samples synthesized onsite at the University of Missouri. The samples were irradiated at the 4.4 and 9 inch positions for both short and long exposure times to achieve four distinct levels of exposure. The treatment groups and the associated dose received by the University of Missouri (MU) samples are given in Table 4.9.

Table 4.8: The irradiation position, target run time, and dose associated with each treatment group for the samples prepared at Y-12.

Treatment Group	Irradiation Position	Bruce Irradiation Time (hrs.)	Dose (Gy)	GE Irradiation Time (hrs.)	Dose (Gy)	Total Dose (Gy)
1	4.4"	67	5350	23	190	5540
2	9"	56	470	23	180	650
3	14"	56	220	23	80	300
4	9"	12	100	6	50	150
5	14"	12	50	6	20	70
6*	Co-60 pit	N/A	N/A	N/A	N/A	6000

*Gamma Dose Reported

Table 4.9: The irradiation position, target run time, and dose associated with each treatment group for the samples prepared at MU.

Treatment Group	Irradiation Position	Bruce Irradiation Time (hrs.)	Dose (Gy)	GE Irradiation Time (hrs.)	Dose (Gy)	Total Dose (Gy)
1	4.4"	55	4950	12.5	100	5050
2	4.4"	24	2170	11.5	90	2260
3	9"	55	510	12.5	100	610
4	9"	24	220	11.5	90	310
5*	Co-60 pit	N/A	N/A	N/A	N/A	6000

*Gamma Dose Reported

Chapter 5 Neutron Spectrum Validation

5.1 Sample Irradiation Stand

To ensure the activation foils and materials received the same neutron dose at each respective irradiation position; a stand was designed to secure the samples at each point. The portable stand was constructed of polyvinyl chloride (PVC) and fitted with acrylic plates to hold several samples for extended periods of time. **Error! Reference source not found.** shows PUR samples secured at the 4.4, 9, and 14 inch positions.

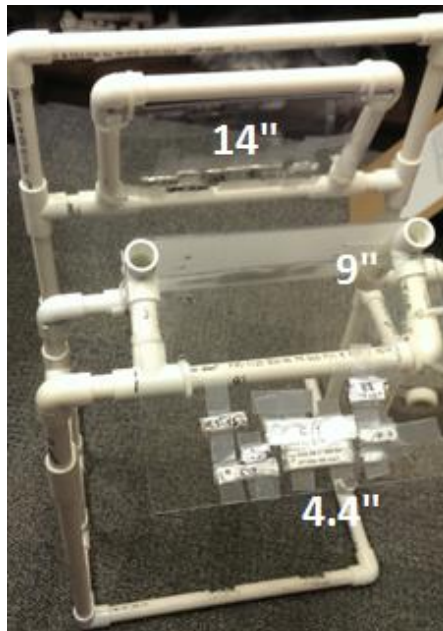


Figure 5-1: PUR samples secured at the 4.4, 9, and 14 inch irradiation positions.

Error! Reference source not found. shows the stand setup in the cyclotron vault at MURR with the four irradiation positions labeled.



Figure 5-2: Portable PVC stand with calibrated positions for irradiation at MURR.

As shown in **Error! Reference source not found.**, samples at the 3 inch irradiation position are placed directly atop the Bruce target, while samples at the remaining three positions are secured onto acrylic plates on the PVC stand. The target stand allows for the irradiation of materials at precise, reproducible positions while not interfering with routine cyclotron operations.

5.2 Activation Foils

Measurements of the neutron flux calculated with MCNP were validated with experimental results using various activation flux foils as threshold detectors. The foils were purchased from Shieldwex[®] and were carefully selected to provide broad coverage of the fast neutron energies of interest. Pure indium, iron, nickel, zinc, and gold foils, each with a diameter of 0.5 inches, were selected for the experiment. The reaction(s) of interest, half-life, threshold energy, peak cross-section energy, and main gamma decay line for each foil are given in Table 5.1.

Table 5.1: Characteristics of the activation foils used for spectrum validation.

Reaction of Interest	Half-life	Threshold Energy (MeV)	Peak xs Energy (MeV)	Main Gamma Line (keV)
$^{115}\text{In}(n,n')^{115\text{m}}\text{In}$	4.5 h	0.5	~1.5	336
$^{58}\text{Ni}(n,p)^{58}\text{Co}$	72 d	2.0	~8.5	811
$^{64}\text{Zn}(n,p)^{64}\text{Cu}$	12.7 h	2.5	~11	511
$^{54}\text{Fe}(n,p)^{54}\text{Mn}$	300 d	2.5	~3.5	835
$^{56}\text{Fe}(n,p)^{56}\text{Mn}$	2.56 h	4.9	~13	847
$^{197}\text{Au}(n,2n)^{196}\text{Au}$	6.2 d	8.5	~15	356

Table 5.1 includes two reactions involving the iron foil, giving a total of six discrete neutron induced nuclear reactions from the five selected foils. All the radioactive

products have a half-life that allows adequate time for counting its decay while also providing high enough activity following the irradiation. While the energy threshold associated with each reaction is useful for determining the neutron spectrum, understanding the peak cross-section (σ_s) energy for each reaction is equally important as this will greatly influence each foils contribution to specific portions of the neutron spectrum.

Since the PUR samples will be intermittingly exposed to the neutron flux emitted by both targets, separate activation foils must be used for each. For this experiment a total of four sets of foils were used, two during routine operation of the Bruce target and two during routine operation of the GE target. Each set of foils was placed in a cadmium cap to shield thermal neutrons and was placed at the 4.4 and 9 inch positions for irradiation. Table 5.2 gives the irradiation parameters associated with each target assembly.

Table 5.2: Activation foils irradiation parameters.

Target Assembly	Time of Irradiation (min)	Beam Current (μA)
Bruce	58	70
GE	60	37

Following irradiation, the neutron induced activities of the five foils were measured with a high purity germanium detector (HPGe) system with Canberra Genie 2000 software. The detector had a 20% relative efficiency relative to a 3" x 3" NaI photon detector for 1.332 MeV photons. The absolute efficiency associated with each measured gamma line was determined for positions one, two, and three using a

geometry matched, NIST traceable mixed gamma source purchased from Eckert and Zeigler. The decay time corrected activity, A_i , of each foil was calculated using Equation 5.1.

$$A_i = \frac{\lambda_i N_\gamma}{I_\gamma \varepsilon (1 - e^{-\lambda_i t_{irr}})(e^{-\lambda_i t_{decay}})(1 - e^{-\lambda_i t_{count}})}$$

Equation 5.1

In Equation 5.1, λ_i is the decay constant of the product radionuclide, N_γ is the number of counts associated with the particular gamma energy peak of interest, I_γ is the gamma yield, ε is the absolute efficiency of the detector at the measured position and energy, and t_{irr} , t_{decay} , and t_{count} indicate the time of irradiation, decay, and counting, respectively. The calculated activities for the activated foils are given below in Table 5.3.

Table 5.3: Decay corrected foil activities at the 4.4 and 9 inch positions.

Reaction of Interest	Activity @ Bruce 4.4" Position (Bq)	Activity @ Bruce 9" Position (Bq)	Activity @ GE 4.4" Position (Bq)	Activity @ GE 9" Position (Bq)
$^{115}\text{In}(n,n')^{115\text{m}}\text{In}$	1.5E5	1.4E4	1.4E4	1.5E4
$^{58}\text{Ni}(n,p)^{58}\text{Co}$	5.7E5	4.6E4	5.0E4	4.7E4
$^{64}\text{Zn}(n,p)^{64}\text{Cu}$	8.2E4	8.1E3	8.4E3	9.1E3
$^{54}\text{Fe}(n,p)^{54}\text{Mn}$	1.7E4	N/A	N/A	N/A
$^{56}\text{Fe}(n,p)^{56}\text{Mn}$	1.1E4	1.2E3	8.3E2	9.6E2
$^{197}\text{Au}(n,2n)^{196}\text{Au}$	1.4E4	3.4E3	1.0E3	2.5E3

For the iron-54 reaction, only the foil at the 4.4 inch position that was irradiated by the Bruce target was able to be counted due to the low activity associated with manganese-54 from the other foils. Using the mass of the foils and the isotopic abundance associated with each reaction, production rates were obtained and used for spectrum unfolding.

5.3 Calibrated Irradiation Positions

The measured production rates from the five activation foils were used to obtain an energy distribution of incident neutron fluence. Neutron spectrum unfolding was determined using adopted methods from Nigg et al. and ASTM-E944 [26, 27]. Following the aforementioned free-beam spectral unfolding algorithm a least-squares fitting procedure was used. The system of activation equations and measured reaction rates were used to calculate an overdetermined flux spectrum for both Bruce and GE targets at the 4.4 and 9 inch positions. The overdetermined flux spectrum utilized three energy bins from 0.35 to 4, 4 to 9, and 9 to 16.5 MeV. Each unfolded spectral distribution was compared against the a priori flux values modeled using MCNP for validation. Figure 5-3 compares the a priori MCNP flux with the overdetermined unfolded flux spectrum at the 4.4 inch position with the Bruce target in operation.

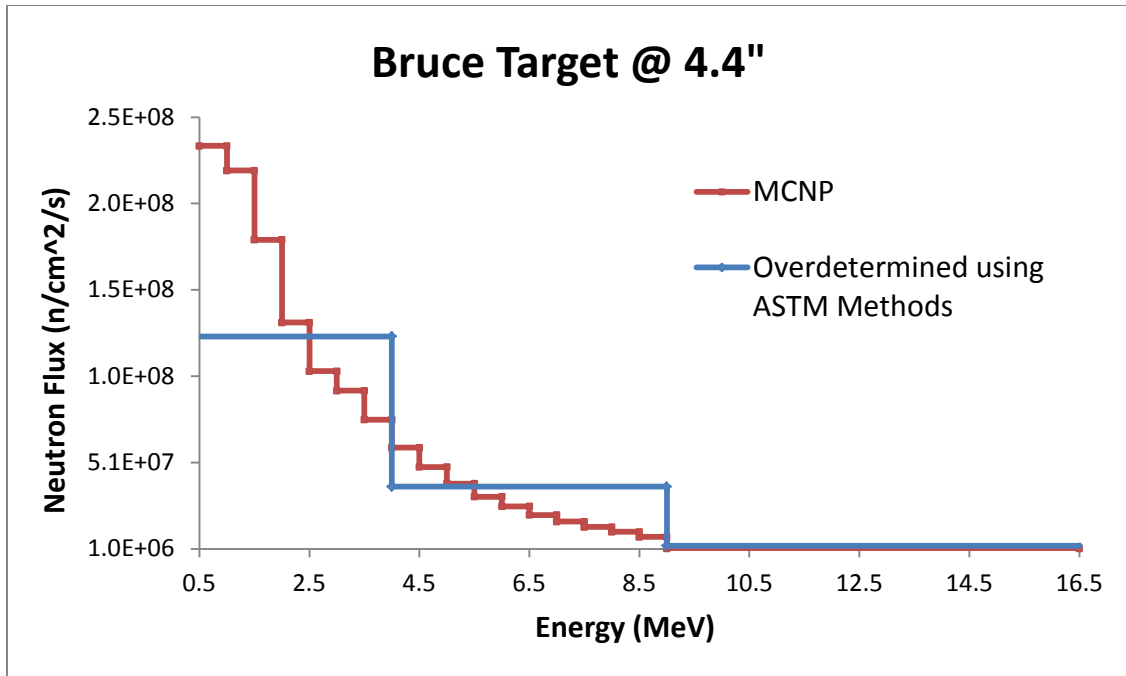


Figure 5-3: MCNP calculated neutron flux spectrum compared to the overdetermined ASTM unfolded spectrum at the 4.4" position for the Bruce target.

Similarly, Figure 5-4 compares the a priori MCNP flux with the overdetermined ASTM unfolded spectrum at the 4.4 inch position with the GE target in operation.

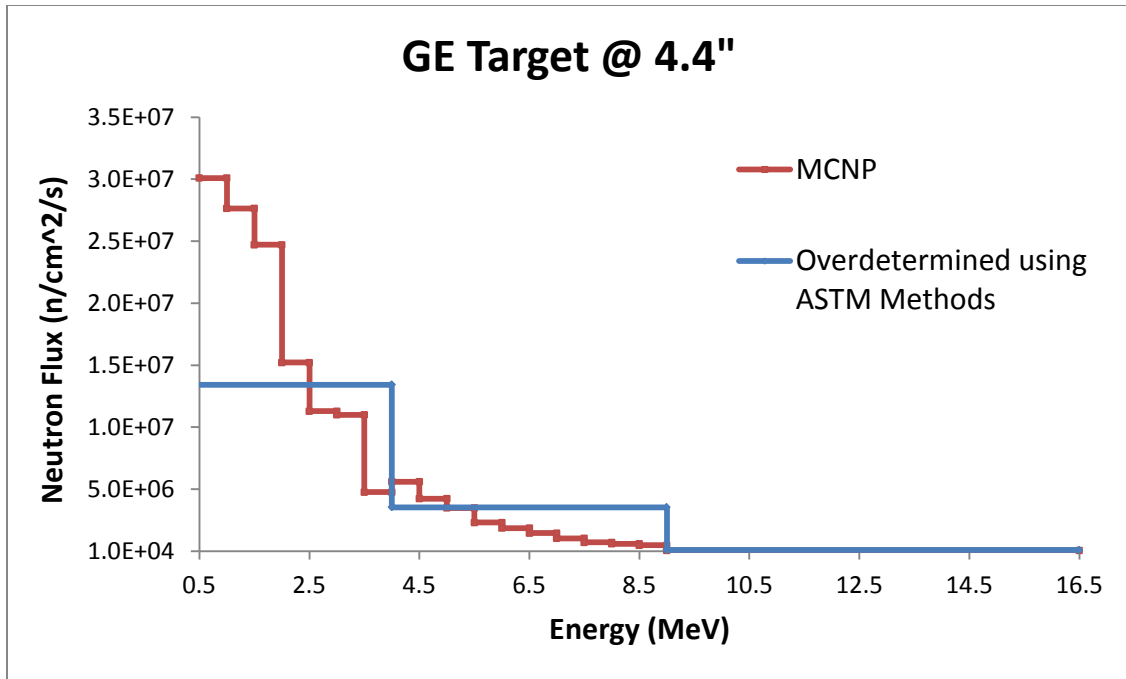


Figure 5-4: MCNP calculated neutron flux spectrum compared to the overdetermined ASTM unfolded spectrum at the 4.4" position for the GE target.

Using the production rates from the second set of activation foils, the flux spectrum at the 9 inch position was unfolded. Figures 5.5 and 5.6 compare the a priori MCNP flux with the overdetermined ASTM unfolded spectrum at the 9 inch position for Bruce and GE targets, respectively.

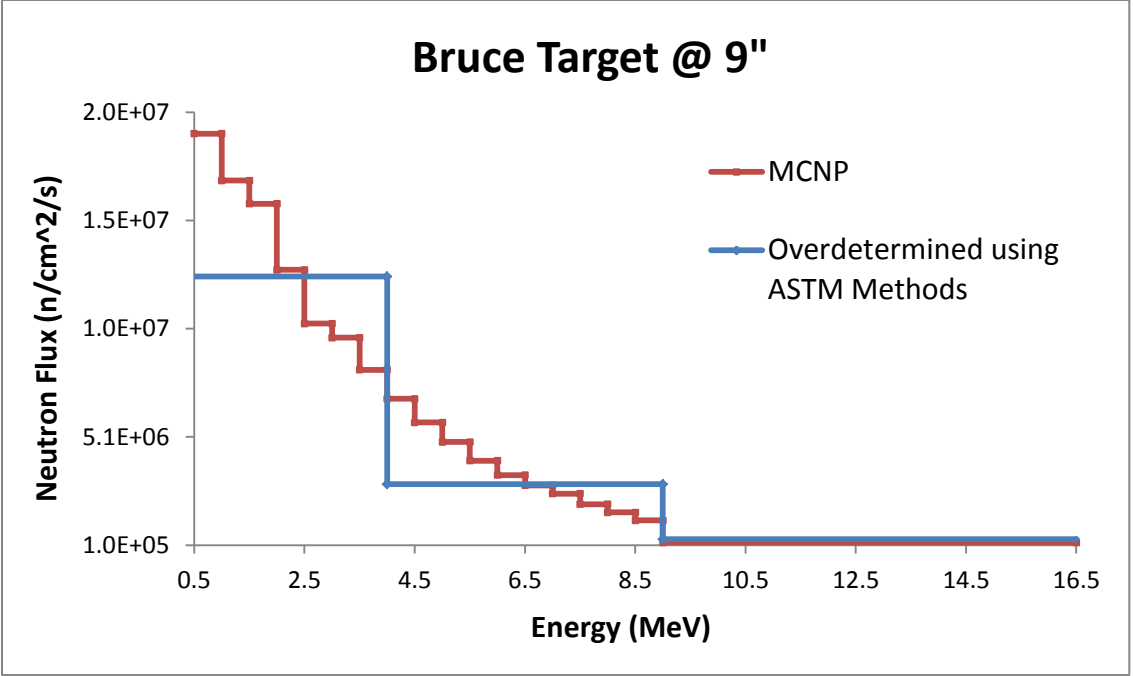


Figure 5-5: MCNP calculated neutron flux spectrum compared to the overdetermined ASTM unfolded spectrum at the 9" position for the Bruce target.

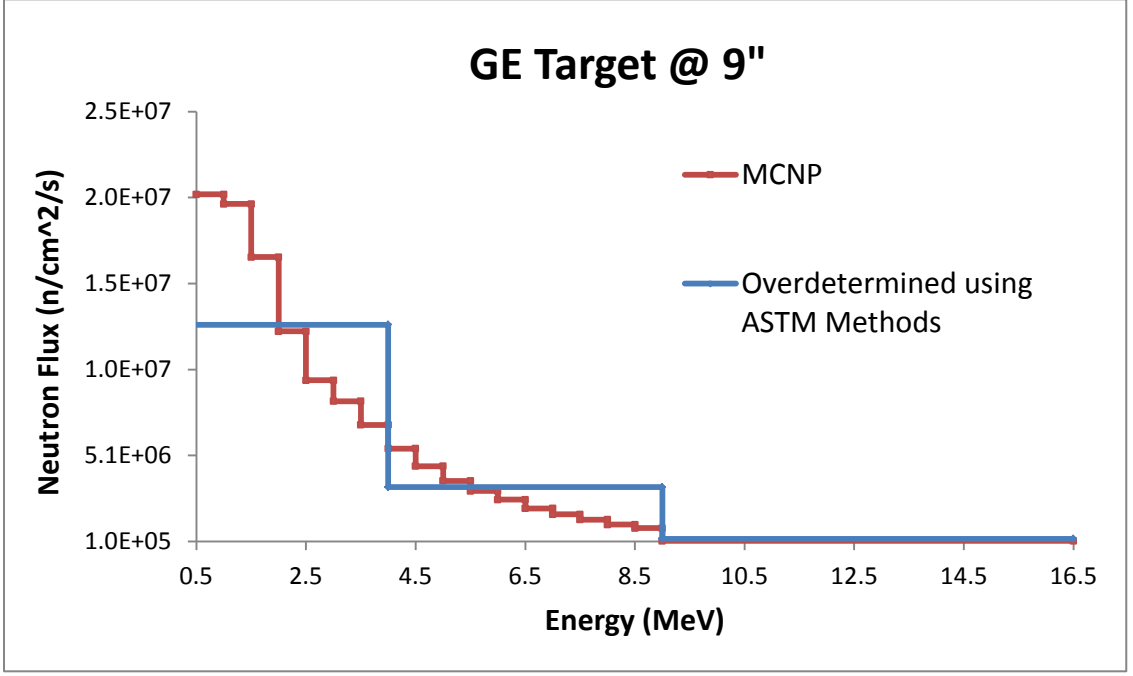


Figure 5-6: MCNP calculated neutron flux spectrum compared to the overdetermined ASTM unfolded spectrum at the 9" position for the GE target.

The total fast neutron flux for 0.5 MeV and greater is given below in Table 5.4 as calculated with MCNP using TENDL data and unfolded using overdetermined ASTM-E944 methods.

Table 5.4: Total fast neutron flux from MCNP and Overdetermined ASTM unfolding.

Target	TENDL MCNP (n/cm²/s)	Overdetermined (n/cm²/s)	Difference
Bruce 4.4"	1.33E+09	1.32E+09	-1%
GE 4.4"	1.56E+08	1.35E+08	-14%
Bruce 9"	1.31E+08	1.26E+08	-4%
GE 9"	1.22E+08	1.29E+08	6%

The a priori MCNP and overdetermined ASTM unfolded flux spectra agree well with one another and validates the calculated neutron flux at the 4.4 and 9 inch positions for both Bruce and GE target assemblies. These experimental results also support the use of the TENDL-2015 cross section data for calculating neutron production from the oxygen-18 target and Havar foil. Tables 5.5, 5.6, and 5.7 compare the overdetermined ASTM unfolded flux spectrum with the calculated MCNP flux using CEM, BERTINI, and INCL physics models, respectively.

Table 5.5: Fast neutron flux from MCNP using CEM physics model.

Target	CEM Model MCNP (n/cm ² /s)	Overdetermined (n/cm ² /s)	Difference
Bruce 4.4"	2.02E+09	1.32E+09	-35%
GE 4.4"	4.11E+08	1.35E+08	-67%
Bruce 9"	1.41E+08	1.26E+08	-11%
GE 9"	1.23E+08	1.29E+08	5%

Table 5.6: Fast neutron flux from MCNP using BERTINI physics model.

Target	BERTINI Model MCNP (n/cm ² /s)	Overdetermined (n/cm ² /s)	Difference
Bruce 4.4"	2.45E+09	1.32E+09	-46%
GE 4.4"	2.68E+08	1.35E+08	-50%
Bruce 9"	2.06E+08	1.26E+08	-39%
GE 9"	1.88E+08	1.29E+08	-31%

Table 5.7: Fast neutron flux from MCNP using INCL physics model.

Target	INCL Model MCNP (n/cm ² /s)	Overdetermined (n/cm ² /s)	Difference
Bruce 4.4"	1.90E+09	1.32E+09	-31%
GE 4.4"	2.24E+08	1.35E+08	-40%
Bruce 9"	1.53E+08	1.26E+08	-18%
GE 9"	1.45E+08	1.29E+08	-11%

These results show that the MCNP neutron flux calculated using TENDL cross sections aligns best with the experimental unfolded flux compared to CEM, BERTINI, and INCL physics models. This is true for both Bruce and GE target assemblies at both the 4.4 and 9 inch irradiation positions.

5.4 Gamma Considerations

5.4.1 Cyclotron Vault

Activation foils as threshold detectors were chosen for spectrum measurements because of their insensitivity to gamma radiation. The foils inherent quality for gamma separation makes them the preferred choice over other methods, such as Bonner sphere systems, for use in mixed radiation fields. Additionally, activation foils require little space and fairly straightforward unfolding techniques compared to other detectors.

5.4.2 Cobalt-60 Beam Port

Gamma radiation can break chemical bonds and prevent bond recombination, especially in organic plastic compounds like the PUR samples presently being analyzed. In general, covalent bonds have the least resistance to decomposition and can contribute to reactions including polymerization, oxidation, and halogenation during irradiation [1]. To help differentiate the physicochemical degradation resulting from neutron and gamma radiation, for each type of PUR material irradiated in the cyclotron vault an identical sample was also placed in a cobalt-60 beam port and exposed only to gamma radiation. The PUR samples were placed in a 1 x 4 inch aluminum sample can

which was then welded shut. The can was lowered 6-8 feet into water and positioned between four separate cobalt-60 sources for approximately 40 minutes. All samples in the cobalt-60 treatment group received 6000 Gy of gamma radiation and function as a reference for gamma degradation mechanisms.

Chapter 6 Analysis of Irradiated Polyurethane

6.1 Attenuated Total Reflectance Fourier-Transform Infrared Spectroscopy

6.1.1 Mechanism and Sampling Technique

Attenuated total reflectance Fourier-transform infrared spectroscopy (ATR-FTIR) is an analytical technique relying on total internal reflection phenomenon to identify the molecular structure of the sample being interrogated. The non-destructive technique requires limited sample preparation and can be used to analyze a variety of sample types, including solids, liquids, gases, gels, and powders. This allows for relatively quick measurements with a high degree of spectral reproducibility while not destroying or interfering with the samples physicochemical characteristics. Two ATR-FTIR systems were used for analyzing the various PUR samples. The samples prepared at the Y-12 National Security Complex were measured using a type 4300 handheld FTIR system from Agilent Technologies. The system was coupled with a diamond ATR interface and was equipped with MicroLab and Grams FTIR collection software. To ensure equal pressure was applied during the measurements, a 3D printed sample holder was built and coupled to the ATR interface. The holder, shown below in Figure 6-1, was constructed

from a polypropylene thermoplastic and allowed a 1 kg calibration weight to be evenly applied during each measurement.

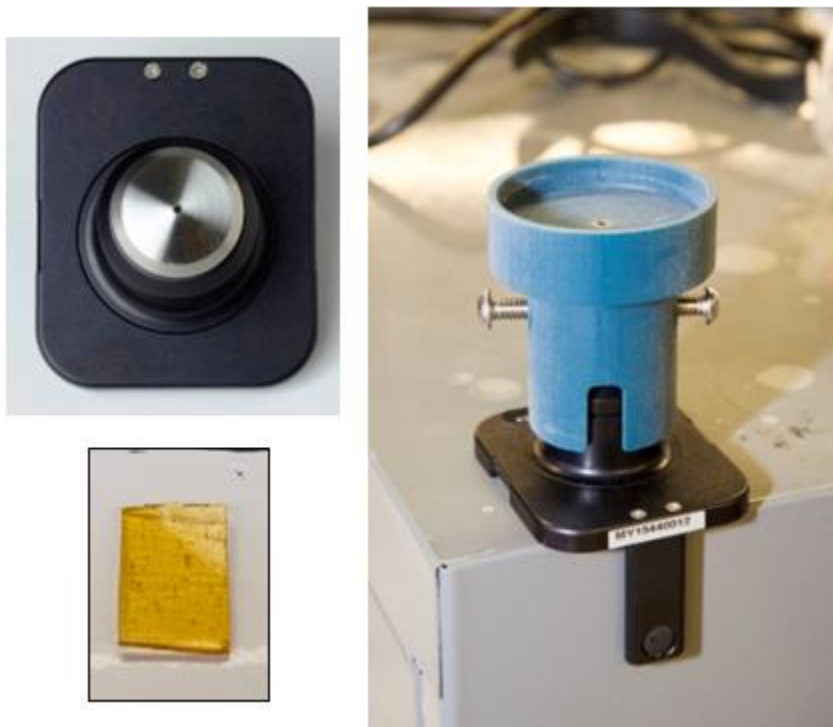


Figure 6-1: ATR interface (top left), PUR sample (bottom left), and 3D printed polypropylene sample holder.

Samples were analyzed in single-reflection mode, as recommended for polymers, using 64 scans and a resolution of 4 cm^{-1} . Samples prepared at the University of Missouri were measured using a Thermo Nicolet Nexus 670 FTIR from Thermo Scientific. The system was coupled with a MIRacle ATR sampling accessory from Pike Technologies and used Omnic FTIR analysis software. This system was configured with a Germanium ATR crystal, whereas the FTIR from Agilent Technologies used a diamond ATR crystal. This causes the resulting IR spectra to differ between the two systems because of the difference in the refractive index and depth of penetration of the crystals. Only samples measured on the same system were directly compared to one another. The Nicolet

system used a micrometer clamp capable of applying up to 3.5 lbs. to secure the sample. As before, samples were analyzed in single-reflection mode using 64 scans and a resolution of 4 cm^{-1} .

Both ATR-FTIR systems operate by measuring the changes that occur in an internally reflected IR beam when the beam comes into contact with a sample. First, an infrared beam is directed onto an optically dense crystal where it is totally reflected at the crystal to sample interface. Due to the crystal having a much higher index of refraction compared to the sample, and the beams wavelike properties, a fraction of the light extends beyond the surface of the crystal and into the sample in the form of an evanescent wave. This is only possible when the incident beam strikes the boundary at an angle greater than the critical angle necessary for total internal reflection. This principle is presented below in Figure 6-2.

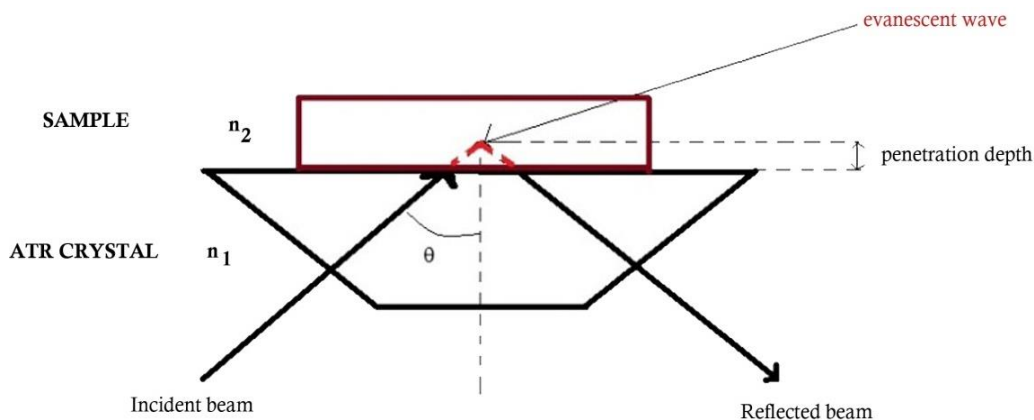


Figure 6-2: Schematic diagram of ATR and total internal reflection principle [28].

The infrared radiation, in the form of an evanescent wave, induces transitions between vibrational energy states as the sample absorbs energy at frequencies characteristic to

its structure. The IR beam only penetrates the sample 0.5 – 3 μm and is defined by the following equation:

$$Depth_{penetration} = \frac{\lambda}{2\pi(\sin^2\theta - n_{21}^2)^{\frac{1}{2}}}$$

Equation 6.1

In Equation 6.1, λ is the wavelength, θ is the incident angle, and n_{21} is the refractive index of the sample divided by the refractive index of the crystal. The detector then records the IR beam as an interferogram signal where it is decomposed into the frequencies that make it up by the mathematical Fourier transformation method. The converted spectrum is presented by plotting the amount of IR radiation absorbed by the sample (absorbance) as a function of wavenumber.

6.1.2 Pre-polymers

In addition to the Y-12 PUR samples, the pre-polymers used in their synthesis were also analyzed using the same 4300 handheld ATR-FTIR system. The IR spectrum of the premixed Halthane 88 (pre-polymer A) is given below in Figure 6-3.

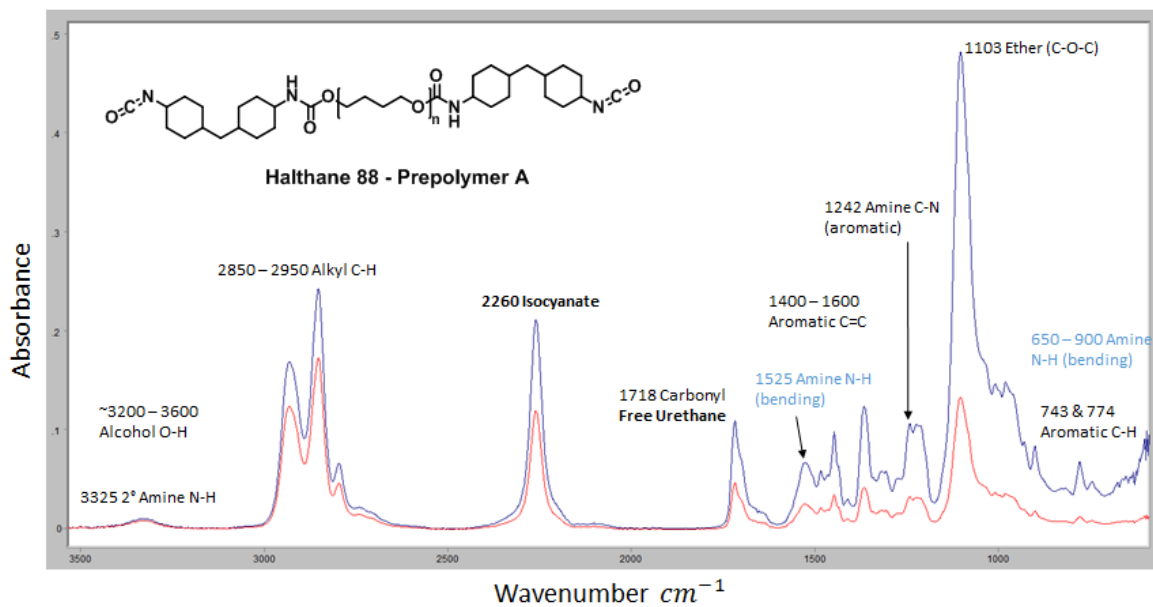


Figure 6-3: IR spectra of pre-polymer A showing the presence of isocyanate and free urethane.

Figure 6-3 shows the original IR spectrum in blue and the ATR corrected spectrum in red for pre-polymer A. IR spectra recorded with an ATR must be corrected to account for the relative shifts in band intensity and is done so according to the penetration depth of the IR beam. Since the penetration depth is proportional to the wavelength, the observed effect is that the absorbance associated with lower wavenumbers must be adjusted down. All remaining IR spectra report the ATR corrected measurements. Distinct peaks are labelled with the stretching or bending (shown in blue) associated with a particular functional group. Figure 6-3 confirms the presence of free urethane and isocyanate in pre-polymer A by revealing strong peaks at 1718 and 2260 cm^{-1} , respectively. Figure 6-4 shows the IR spectrum of Asilamine 170 (pre-polymer B).

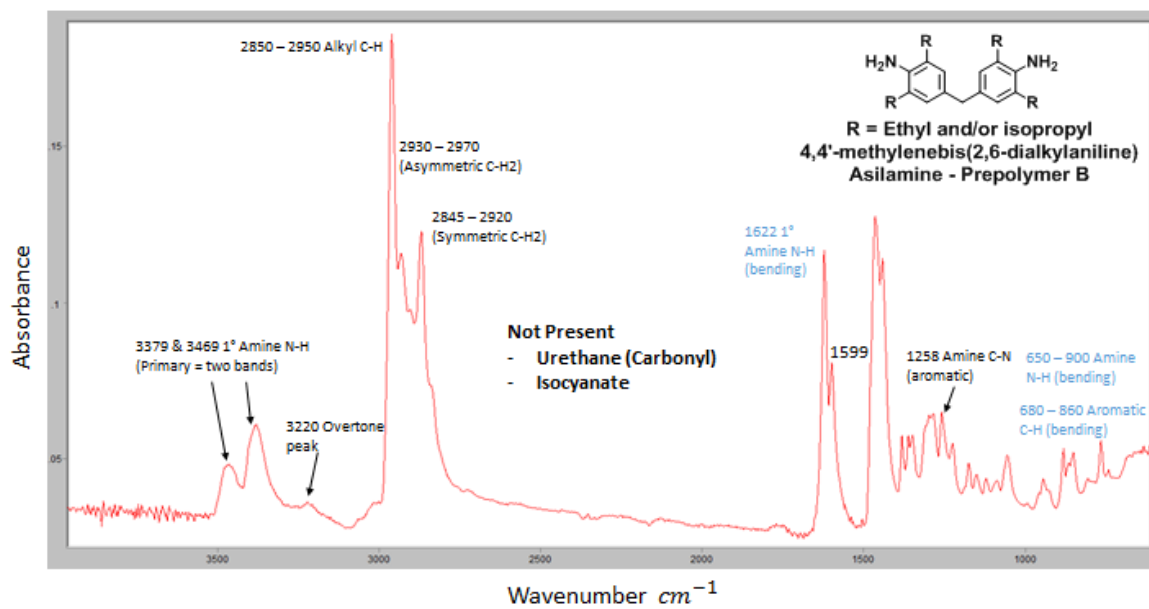


Figure 6-4: IR spectra of pre-polymer B used for synthesizing Y-12 PUR samples.

As expected, Figure 6-4 reveals the absence of urethane and isocyanate in pre-polymer B. The two distinct bands at 3379 and 3469 cm^{-1} are associated with the stretching vibrations of the primary amines, while the peak at 1622 cm^{-1} is associated with the bending vibrations. Understanding the IR spectra associated with pre-polymers A and B is crucial for recognizing changes in the PUR samples post irradiation.

6.1.3 Atmospheric vs Degassed: Observed Isocyanate Reaction

PUR samples were prepared using either atmospheric or degassed methods. Figure 6-5 compares the entire IR spectra of interest, $1000 - 3400\text{ cm}^{-1}$, of the Y-12 control samples prepared using both methods.

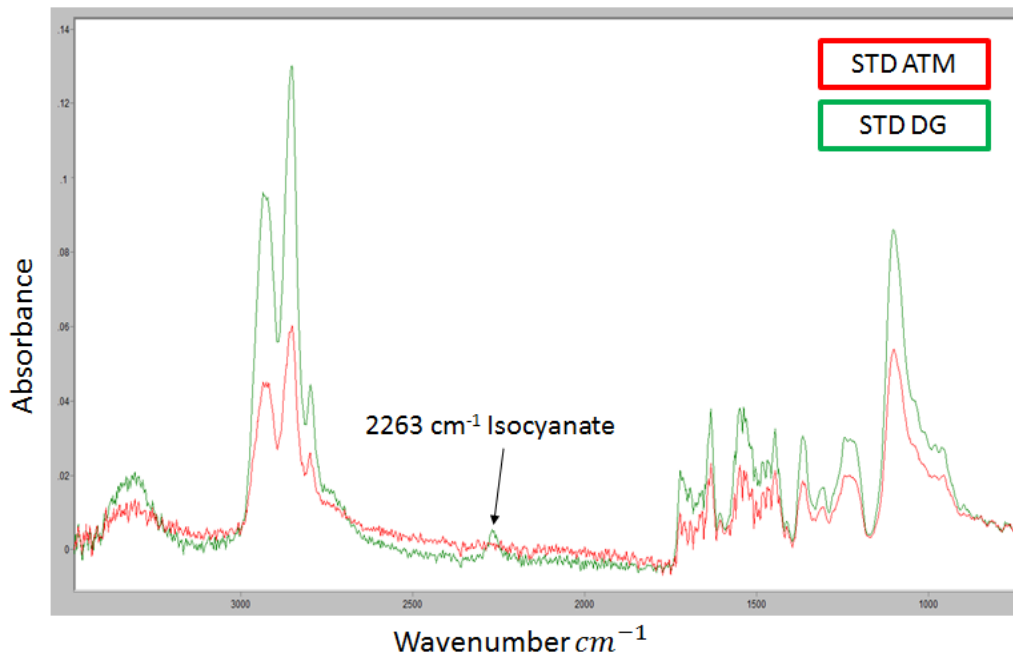


Figure 6-5: IR spectra comparing Y-12 PUR standard controls prepared under atmospheric conditions (STD ATM) and when pre-polymers were degassed under vacuum (STD DG).

Figure 6-5 shows that the degassed control contained excess isocyanate, represented by a definitive peak at 2263 cm^{-1} , while the standard atmospheric samples did not contain this peak. The presence of isocyanate can be attributed to the absence of water reducing the rate of reaction in the case of the degassed samples. This is because water behaves as a catalyst in the reaction of an amine with isocyanate when forming carbamic acid. Figure 6-6 shows the IR spectra of two degassed samples from treatment group 1.

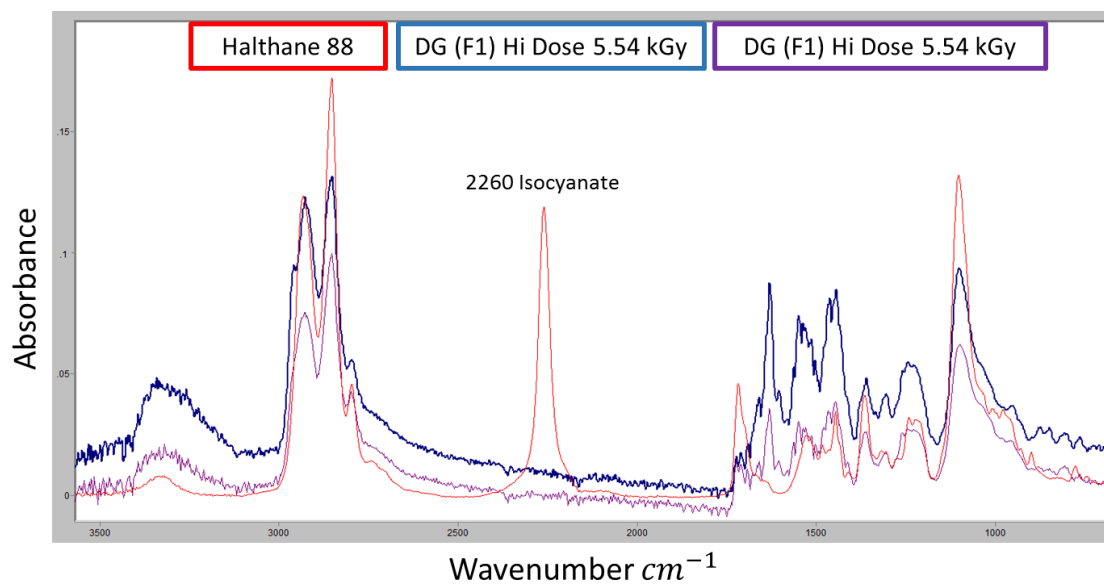


Figure 6-6: IR spectra of degassed PUR samples from treatment group 1.

Figure 6-6 displays the IR spectra of pre-polymer A for reference, as the 2260 cm^{-1} isocyanate peak previously observed in the degassed standards is no longer present in the samples following neutron irradiation. These results suggest that high dose irradiation, on the order of kGy, reacts excess isocyanate in PUR samples prepared using degassed pre-polymers. It is interesting to note that the presence of isocyanate in a sample of Halthane-88 is an indicator that the sample was prepared in conditions that reduced the amount of water in the pre-polymers at the time of mixing. This relatively costly degassing step suggests that the adhesive polymer was specifically prepared for a water sensitive application.

PURs were further investigated using samples made at the University of Missouri and examining the correlation between the isocyanate concentration and received dose. To minimize the effect of sample heterogeneity, IR spectra were taken before and after

irradiation for every PUR specimen. Figure 6-7 shows the isocyanate peak region of the IR spectrum for sample 1 and compares treatment groups 1 (high dose) and 4 (low dose) and non-irradiated control prior to and following irradiation.

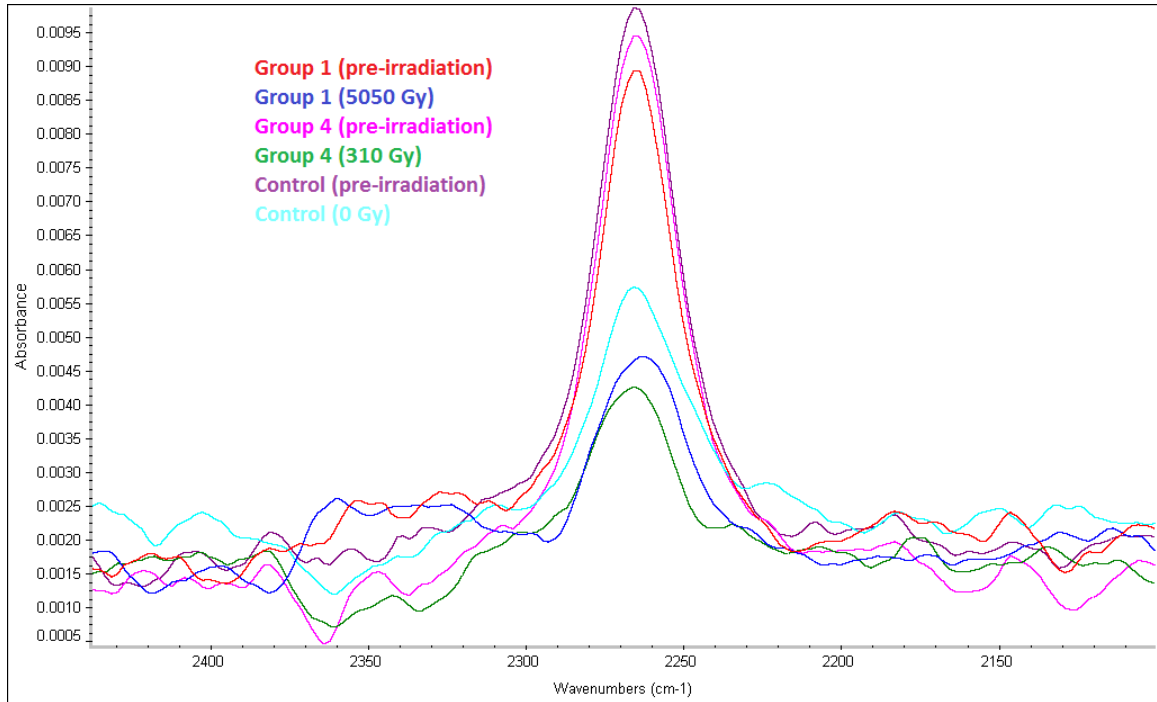


Figure 6-7: Sample 1 treatment groups 1 and 4 and non-irradiated control prior to and following irradiation.

Figure 6-7 shows that sample 1 pre-irradiation measurements exhibit the same characteristic isocyanate peak that was observed in the degassed samples prepared at Y-12 after receiving no neutron dose. However, whereas previously the isocyanate peak disappeared entirely following irradiation, it now continues to be present regardless of radiation exposure. In each case, the peak height was highest pre-irradiation and then decreased when measured after irradiation. This relative decrease in peak height is exhibited in all measured PUR specimens, including the non-irradiated control as shown above. The isocyanate concentration in the same PUR specimen decreased throughout

the experiment, independently of neutron radiation exposure. Figure 6-8 compares sample 2 treatment groups 1, 5 and non-irradiated control pre and post irradiation.

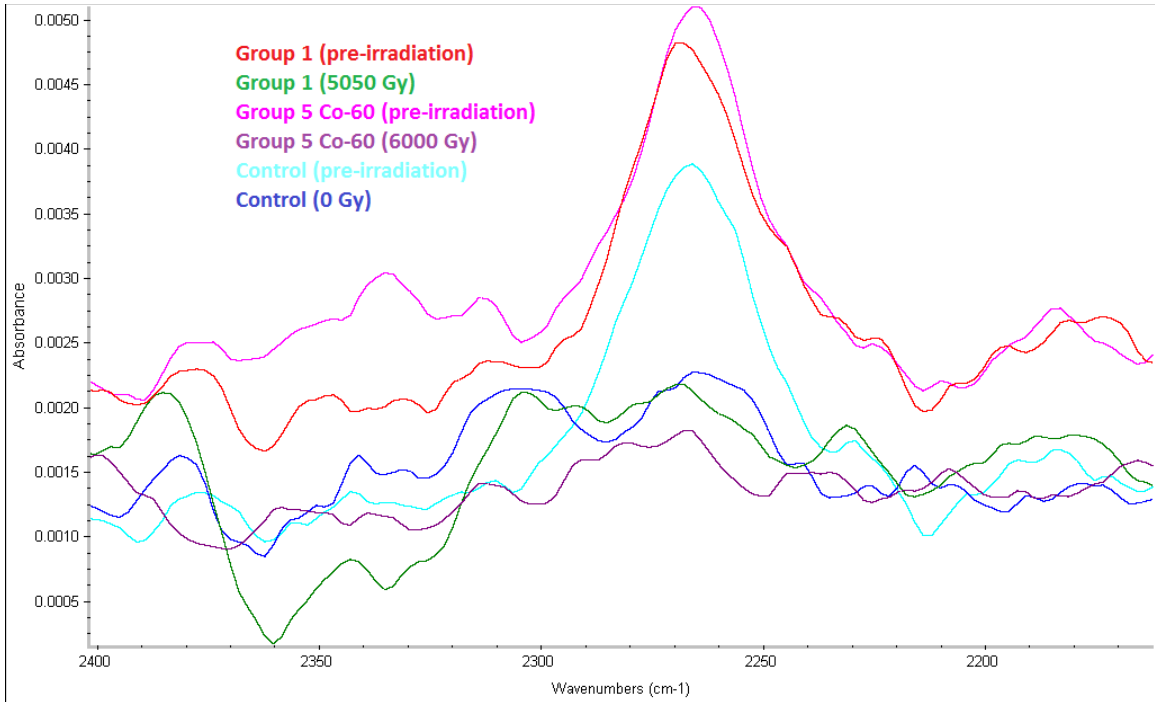


Figure 6-8: Sample 2 IR spectra comparing treatment group 1 with standard control and pre-irradiation.

Figure 6-8 shows that isocyanate is present in the pre-irradiation IR spectra but is absent when measured post-irradiation in both treatment group 1 and the non-irradiated control. IR spectra of the remaining samples reflect the findings exhibited in samples 1 and 2 and suggest that neutron exposure in this dose range is not responsible for the decrease in isocyanate concentration. The relative decrease in isocyanate concentration with time suggests that the samples continue to cure over the length of the experiments, as pre-polymers A and B continue to react. Additionally, the relative decrease in isocyanate concentration may be due to prolonged exposure to air, as the water in the air can directly react with the excess isocyanate.

6.1.4 Dose Dependent Physicochemical Changes

IR spectra of the irradiated PUR samples were analyzed and compared to determine if a dose response could be identified. Figure 6-9 compares the IR spectra of the Y-12 PUR samples for treatment groups 1 through 6 and a non-irradiated control.

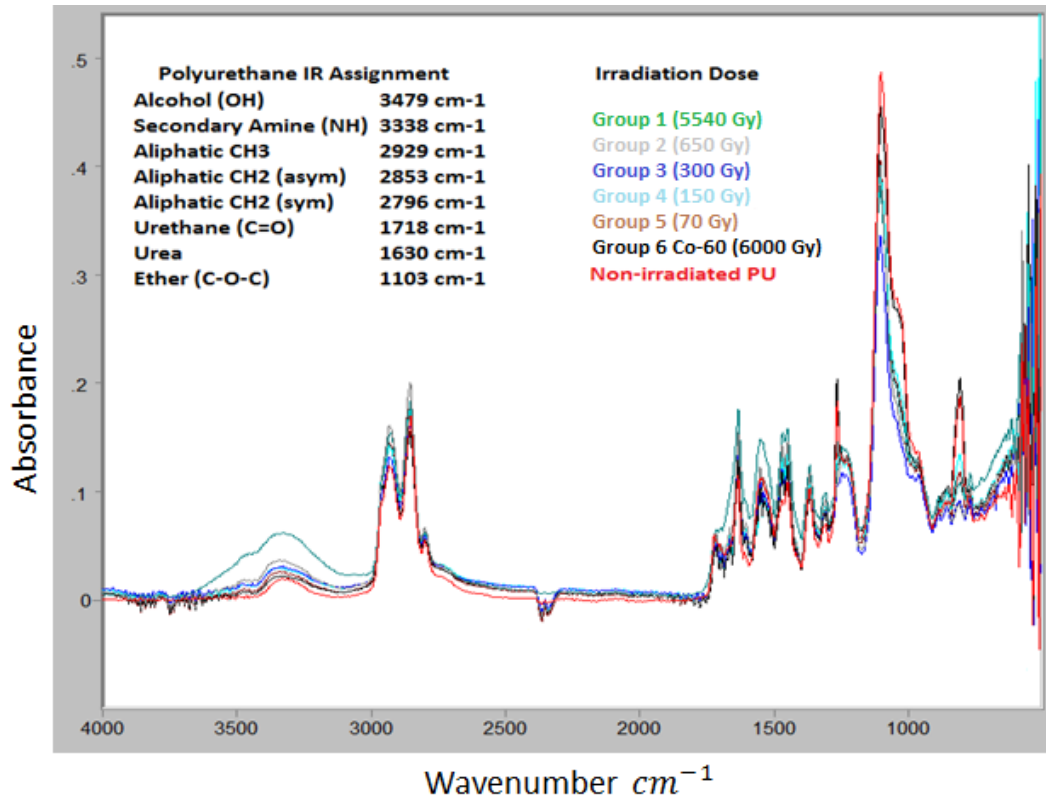


Figure 6-9: Comparison of non-irradiated control Y-12 ATM PUR versus treatment groups 1-6.

Figure 6-9 includes the entire IR spectra considered for comparison and labels the characteristic peaks associated with PUR. The urea, urethane, secondary amine and alcohol peaks were identified as peaks of interest as changes in the molecular structure are observed between treatment groups compared to the non-irradiated control. Figure

6-10 further examines the dose response for secondary amines and alcohol as previously observed.

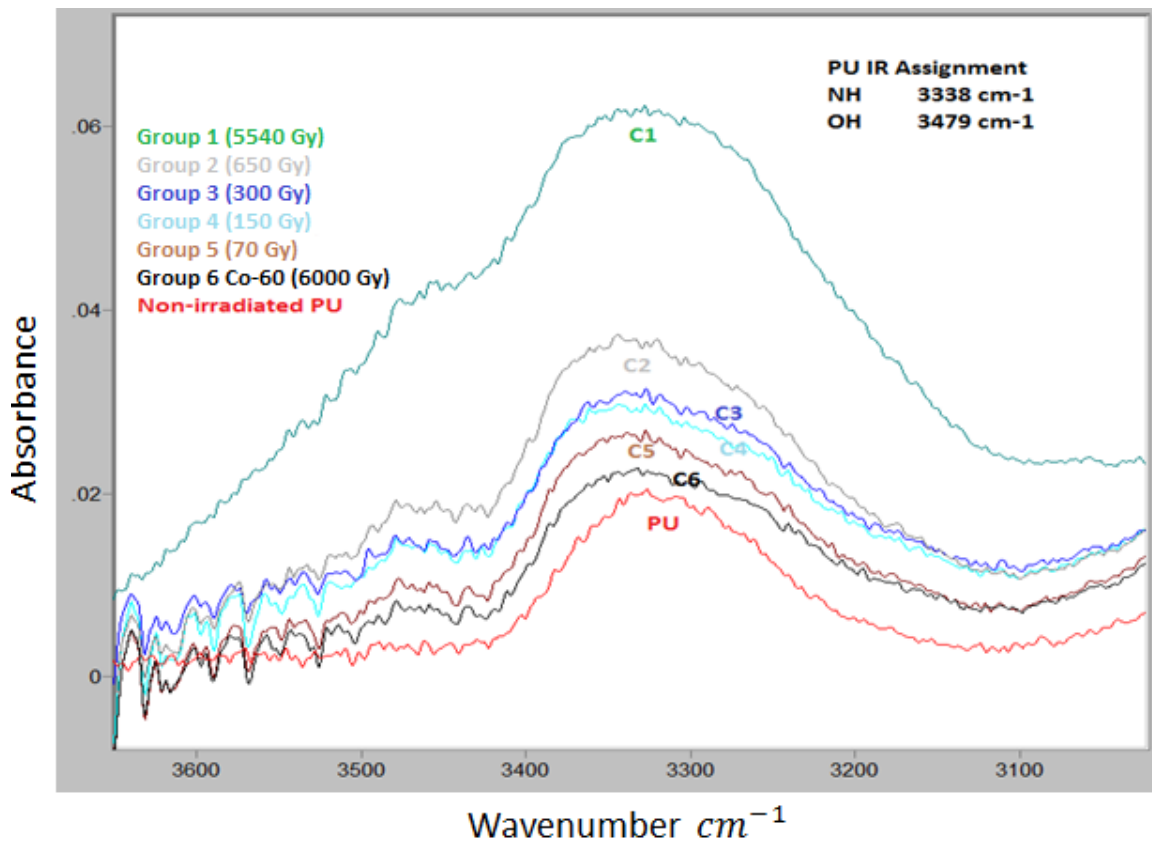


Figure 6-10: Dose response of secondary amines and alcohol in ATM PUR.

Figure 6-10 suggests that PUR samples prepared under atmospheric conditions demonstrate a dose response as the concentration of secondary amines and alcohol increases as the neutron dose increases. Mechanistically, an increase in alcohol functionality could be caused by the cleavage of the polyether soft segment of PUR. This suggestion is possible as the concentration of ether linkages was found to slightly decrease following neutron exposure, as shown below in Figure 6-11.

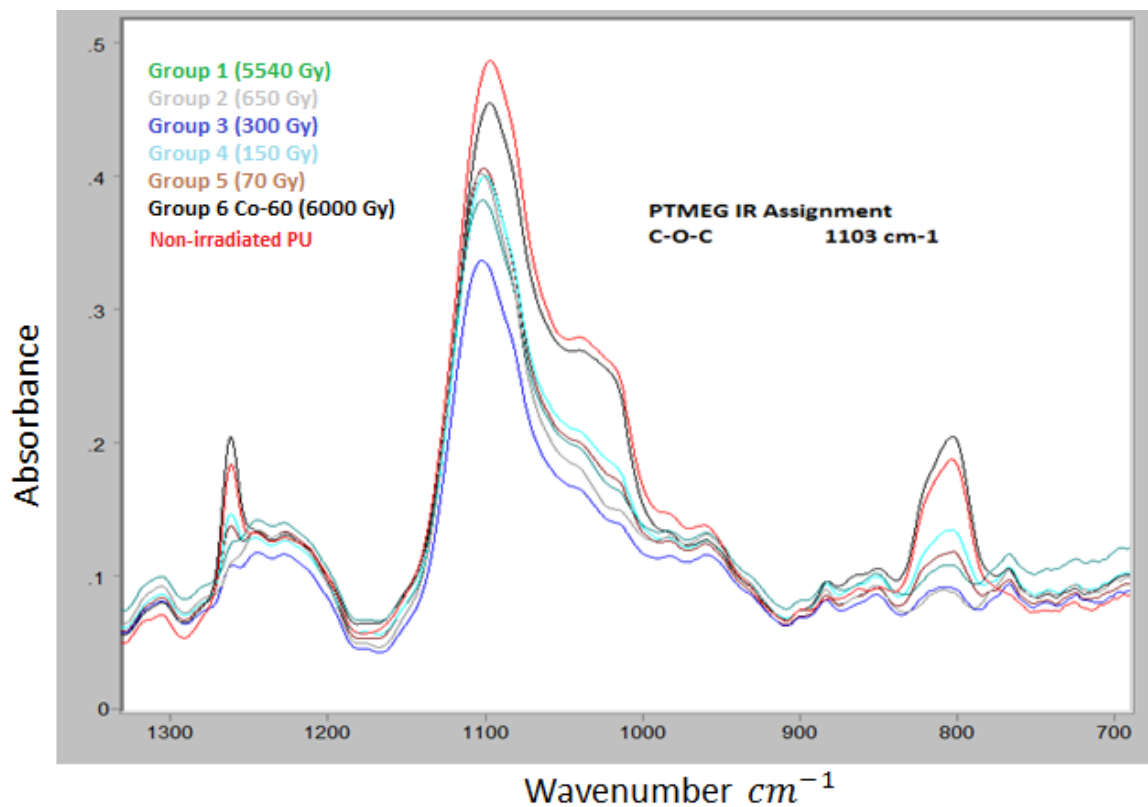


Figure 6-11: Ether cleavage following neutron exposure in ATM PUR.

While the irradiated treatment groups do not fit a dose response, Figure 6-11 does show the concentration of ether to be lower post irradiation. Comparing the relative urethane and urea concentrations before and after irradiation was initially hypothesized as a potential candidate for exhibiting a dose response due to urethane's susceptibility to free radical formation following irradiation. Figure 6-12 shows the relative urethane and urea concentrations compared to a non-irradiated control for ATM Y-12 samples.

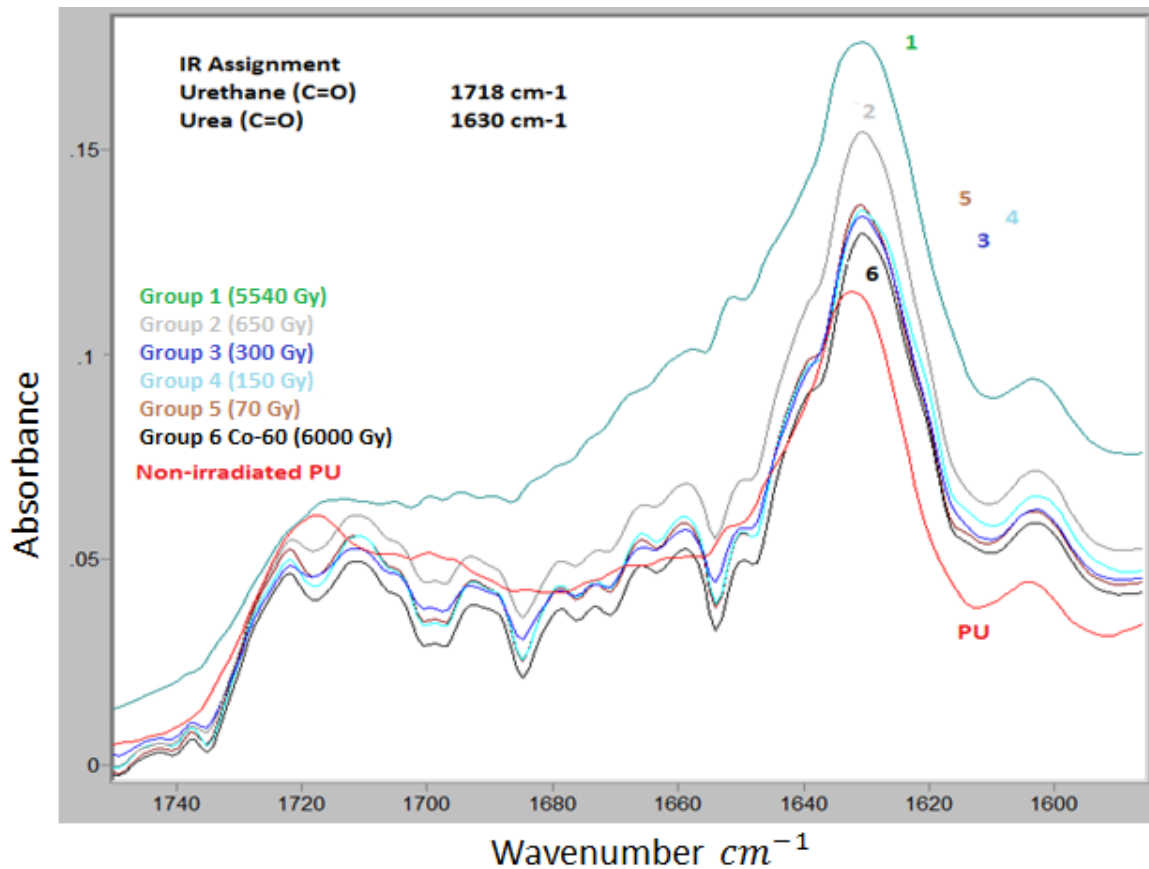


Figure 6-12: Urea and Urethane concentrations for Y-12 ATM PUR samples groups 1-6.

Figure 6-12 suggests an increase in urea concentration with a relative decrease in urethane concentration following irradiation. While no dose response is directly observed, treatment groups 1 and 2 exhibit the highest urea peaks relative to their urethane concentration. The potential degradation of urethane in the presence of amines could produce more urea linkages. Additional samples must be analyzed to definitively characterize the dose dependency associated with these functional groups.

The second experiment considered 11 samples synthesized at the University of Missouri with different production characteristics, as presented in Table 3.1. As before,

the IR spectra post irradiation were compared to non-irradiated controls to identify and characterize changes in the molecular structure of the PUR. In addition to using non-irradiated controls, each PUR specimen was measured prior to irradiation to allow for a direct comparison while negating the potential differences from specimen to specimen. Figure 6-3 shows sample 7 IR spectra for treatment groups 1, 5, and non-irradiated control before and after irradiations.

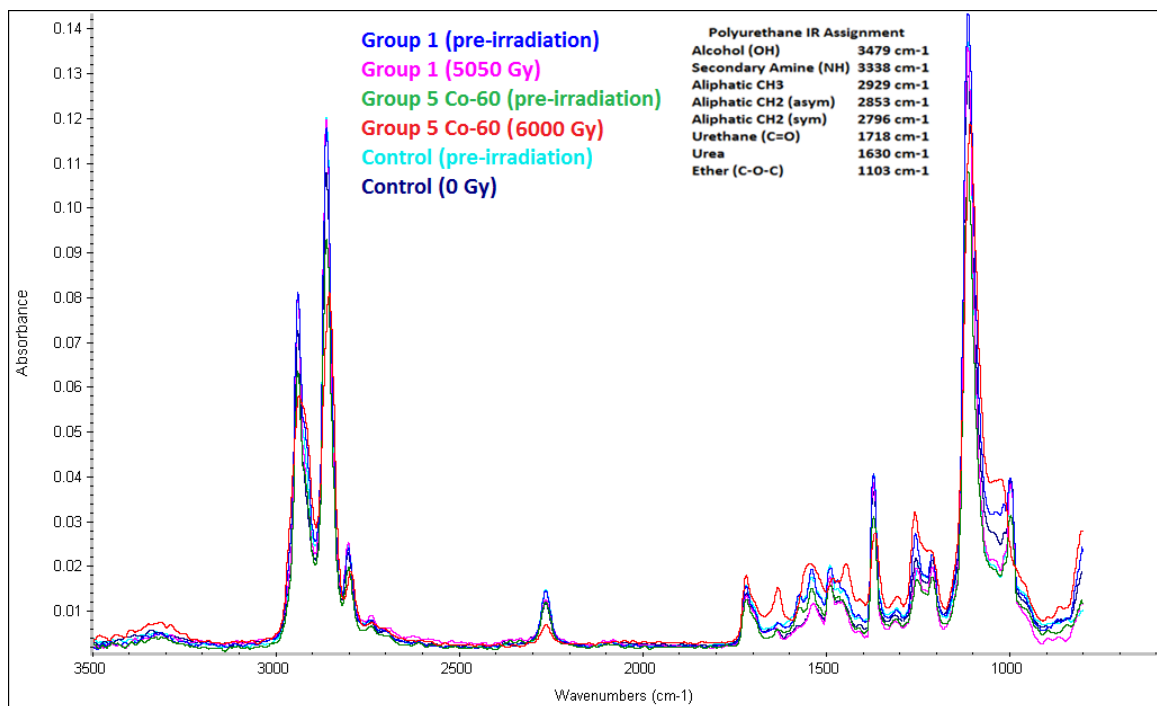


Figure 6-13: Sample 7 IR spectra of treatment groups 1, 5, and non-irradiated control before and after irradiation.

Figure 6-13 labels the characteristic peaks observed in the IR spectrum for sample 7. There are no recognizable differences between treatment group 1, however treatment group 5 showed a decrease in isocyanate and increase in amine and urea concentrations after exposure to gamma radiation. Figure 6-14 shows how the concentration of urea in sample 7 changes before and after irradiation.

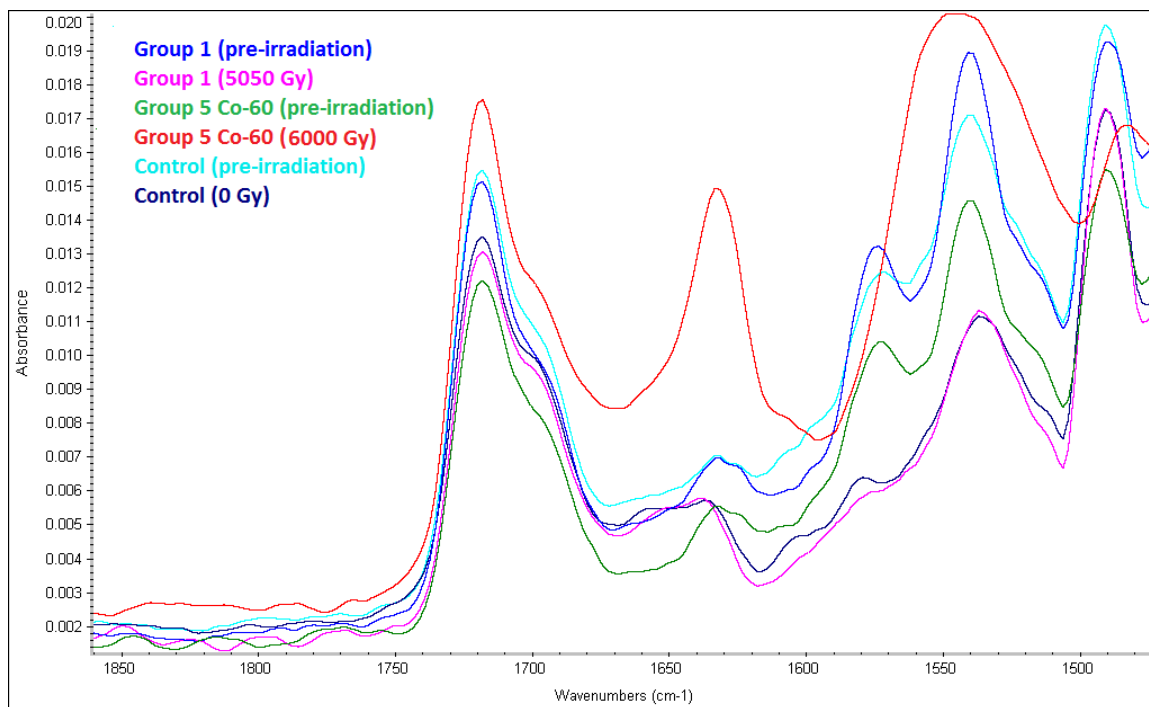


Figure 6-14: Sample 7 urethane and urea concentrations prior to and post irradiation.

Figure 6-14 shows a relative decrease in urethane to urea concentrations after exposure to gamma radiation, but no discernable effect following neutron exposure. Figure 6-15 compares the IR spectra of sample 4 treatment groups 1, 4, and control before and after irradiation.

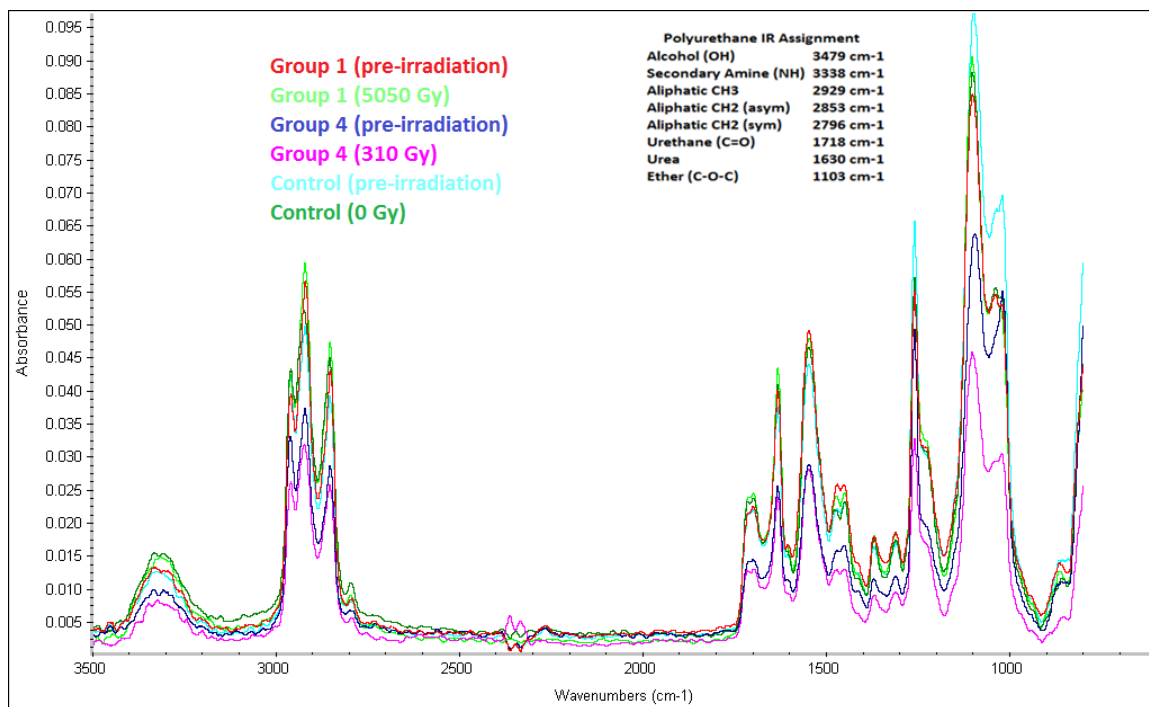


Figure 6-15: Sample 4 IR spectra of treatment groups 1, 4, and non-irradiated controls before and after irradiation.

Like sample 7, Figure 6-15 shows no noticeable changes in sample 4 that can be directly attributed to the received neutron dose. To more accurately identify and characterize minor changes due to neutron irradiation, statistical peak analysis is required. Regression analysis was used to compare the changes in relative peak heights in samples 1 through 11 due to the neutron dose received. Figure 6-16 shows a regression analysis of the relative urethane to urea ratio as a function of neutron dose for sample 4.

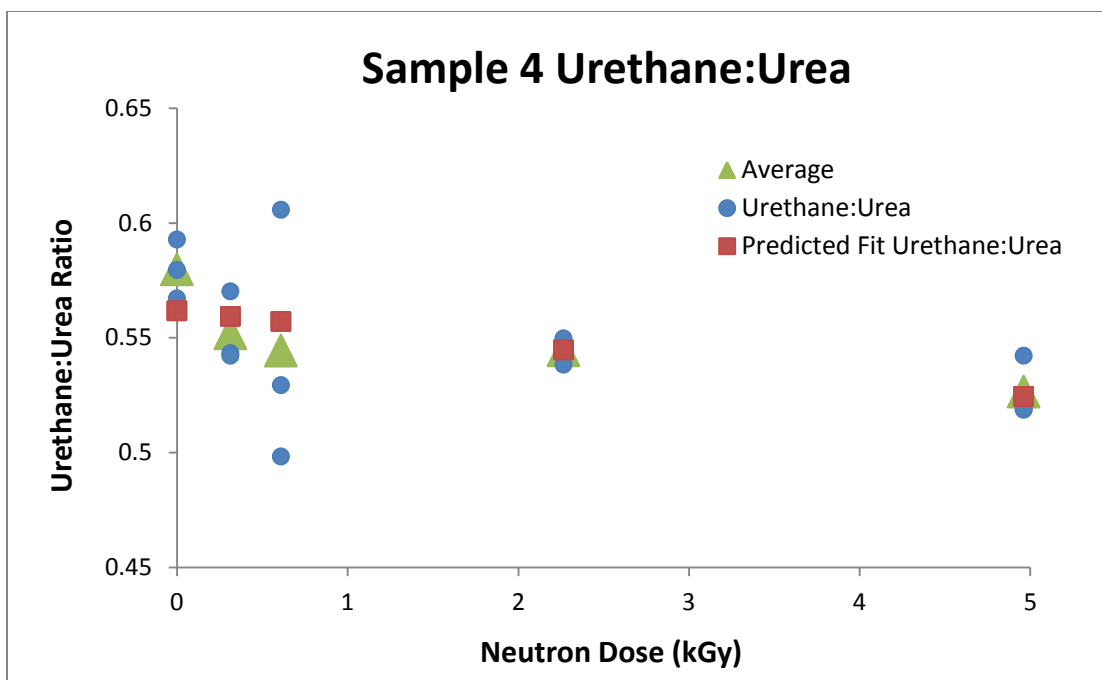


Figure 6-16: Regression analysis of the urethane to urea concentrations as a function of neutron dose for sample 4 (prepared under ATM conditions).

Figure 6-16 demonstrates a slight decrease in the ratio of urethane to urea concentrations as neutron dose increases. Of samples 1 through 11, sample 4 exhibited the greatest correlation between the urethane/urea peaks and dose, with a P-value of 0.06. The P-value represents the level of marginal significance dose plays in changing the urethane to urea ratio. A calculated P-value of less than 0.05 indicates a significant correlation, with larger values indicating the predictor, in this case dose, not being statistically significant. The analysis shows that all remaining samples result in a P-value greater than 0.1.

The change in relative peak heights of the amine and urea functional groups was also studied. Figure 6-17 shows how these functional groups change as a function of dose for sample 4.

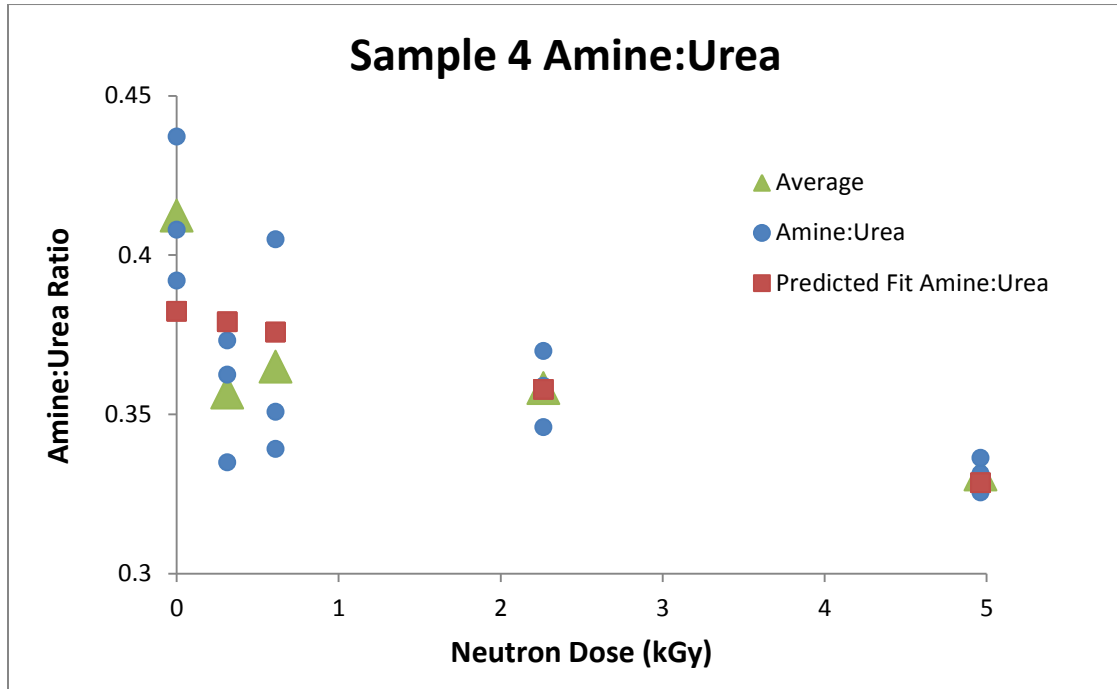


Figure 6-17: Regression analysis of the amine to urea concentrations as a function of neutron dose for sample 4 (prepared under ATM conditions).

The ratio of amines to urea demonstrated the greatest dependence on dose in sample 4, with a P-value of 0.01. Figure 6-17 suggests that dose is significant in determining the relative concentrations of amine and urea in the sample 4 PURs. This suggests the ratio of amines to urea could be used as a simple test in differentiating between non-irradiated PURs and those that have absorbed 5 kGy. One explanation for this is the potential reaction between excess amine and urethane to form urea. With sample 4 being prepared in atmospheric conditions, there was no isocyanate present in the IR

spectra. As previously stated, this is likely due to the reaction of isocyanate with water which yields an amine. This would cause there to be an initial increase in amine concentration, which in the presence of urethane will react to form urea. As neutron dose increases, the potential increase in available urethane would cause the ratio of amine to urea to decrease as amines react with urethane to produce urea. The remaining samples showed no discernable neutron dose response, resulting in P-values larger than 0.05.

Chapter 7 Conclusions

7.1 Calibrated Neutron Flux Spectrum

7.1.1 Efficacy and Challenges

The neutron flux was calculated using MCNP at four positions within the cyclotron vault. The model includes the Bruce Technologies (TS-1650P) and GEMS (P5230 flourine-18) target assemblies as both are intermittingly used with the GE PETtrace cyclotron at the MURR. Experimental results using five activation flux foils as threshold detectors was used to validate the calculated neutron flux obtained from MCNP at the 4.4 and 9 inch irradiation positions. The a priori MCNP, with TENDL cross section data, and the unfolded flux spectra agree well with one another showing only minimal differences in the total neutron flux detected. A difference of 1% and 14% was determined between the calculated MCNP and over determined flux for the 4.4 inch position for Bruce and GE targets, respectively. Similarly, a difference of 4% and 6% was determined for the 9 inch position for Bruce and GE targets, respectively. The a priori

MCNP neutron flux calculated using TENDL cross sections aligns best with the experimental unfolded flux compared to CEM, BERTINI, and INCL physics models. This is true for both Bruce and GE target assemblies at both the 4.4 and 9 inch irradiation positions and validates the use of TENDL data.

One limiting factor of the flux unfolding methodology used is that it only defines broad neutron energy groups. While it is helpful for total neutron flux comparisons, it does not validate the fine group energy resolution calculated using MCNP. For further validation, either the use of more activation foils or employing an underdetermined flux spectrum unfolding algorithm can be used. This would allow for additional energy groups to be used in order to better define the spectrum at specific neutron energies. Use of more than one unfolding technique would increase confidence in the neutron spectrum calculations. Future work associated with this research will use STAYSL PNNL computer code to perform least-squares neutron spectral adjustment in addition to ASTM-E944 techniques presented here for more comprehensive validation and can be extended to validate the neutron flux at the 14 inch position.

The development of two fast neutron irradiation positions at the MURR GE PETtrace cyclotron was achieved and validated using MCNP with TENDL cross section data and neutron activation foils with spectrum unfolding. The validated neutron flux results suggest the correct neutron dose is being estimated at each irradiation position. The ability to adjust the MCNP model to accommodate changes in beam current, target assemblies, and material irradiation positions is a major advantage of its application.

7.1.2 Future Applications

Knowledge of the neutron flux spectrum surrounding a medical cyclotron is fundamental for determining adequate shielding, operational dose limits, and evaluating neutron activation of various accelerator and vault components over time. Utilizing the secondary neutrons emitted during fluorine-18 production for radiolysis studies and radioisotope production is a novel approach. The ultimate appeal of these applications is that fast neutrons are already consistently being generated in this routine process. The specially designed irradiation stand allows samples to receive a controlled neutron dose at distinct positions within the cyclotron vault. This research shows that the characterized neutron flux can be used in accelerated aging studies to simulate nuclear environments involving fast neutron radiation. While in this research it was used to prepare surrogate irradiated PUR material representative of arsenal elements, namely Halothane 88-3, the same experimental concept could be applied to other materials. This includes: examining neutron damage to electronic circuitry (radiation hardening), evaluating components commonly used in aviation and aerospace applications, studying the activation and release of radioactive gases into the atmosphere, and assessing and calibrating neutron dosimetry techniques.

Perhaps the most promising application of this research is the novel opportunity for isotope production utilizing the secondary fast neutron flux emitted from a primary target. Placement of the production target material near the primary cyclotron target could be easily achieved by utilizing an irradiation calibration stand, similar to the stand

designed and constructed for his research. As cyclotron technologies advance, higher beam energies and intensities will result in higher secondary neutron energies that are capable of producing more radioisotopes without a nuclear reactor. Current candidates for radioisotope production via fast neutrons resulting in no-carrier-added product include chlorine-36, scandium-47, nickel-63, copper-67, krypton-85, zirconium-89, radium-224, actinium-225, thorium-229, palladium-231, and neptunium-237 [29]. The potential for secondary radioisotope production is greatest at facilities employing a high energy proton beam, with energies beyond 40 MeV, capable of attaining both clinical and research scale production yields.

7.2 Dose Response of Irradiated Polyurethane

7.2.1 Efficacy & Challenges

Following irradiation of PUR, the degree of radiolysis was analyzed using ATR-FTIR to quantify neutron dose dependent changes. Results show a distinct isocyanate peak in samples prepared using degassed methods and in select samples prepared under atmospheric conditions because water behaves as a catalyst in the reaction between isocyanate and amine. The absence of water in the samples prepared using degassed pre-polymers reduced the reaction rate resulting in excess isocyanate. While initial results suggested that high dose irradiation reacted with excess isocyanate, additional analysis found no correlation between the change in isocyanate concentration and neutron dose. Similarly, while certain dose responses could be observed in select PUR samples, no exhaustive or reproducible conclusions could be

drawn. Further analysis and validation of the samples is required to corroborate certain observations including: the increased concentration of secondary amines and alcohol, decreased concentration of ether linkages, and relative increase of urea:urethane and urea:amine concentrations with neutron dose.

The quick setting time of the PUR samples presented a major challenge in obtaining a completely homogeneous system. This resulted in complicated spectral comparisons and made it difficult to attribute any observed changes directly with neutron dose. Additionally, the effect of heterogeneity was only more pronounced due to ATR-FTIR only penetrating a few microns into each sample. The results also suggest that certain samples continued to cure throughout the experiment, causing changes in certain functional group concentrations with time. Collectively, the results show that PURs do not appear to be affected up to doses of 5 kGy and should be considered for use in radiation fields.

7.2.2 Future Work

Future work will analyze PUR samples receiving doses from 10-1000 kGy. Simpler polymer compounds, in addition to pre-polymers, will be irradiated and analyzed to minimize the effects of heterogeneity. Analysis techniques including thermomechanical analysis, differential scanning calorimetry, thermogravimetric analysis, electron paramagnetic resonance, and gas chromatography-mass spectrometry will be used to further identify and characterize potential dose dependent changes.

References

1. International Atomic Energy Agency, *Cyclotron Produced Radionuclides: Principles and Practice*, in *Technical Reports Series, Report No.: TRS465*. 2009, International Atomic Energy Agency Stationery Office, The Distributor: Lanham, London.
2. Szycher, M. and Ebrary Inc., *Szycher's handbook of polyurethanes*. 2013, CRC Press,; Boca Raton, FL. p. 1 online resource.
3. American Chemistry Council. *Polyurethanes*. 2018 [cited 2018 25 Jan]; Available from: <https://polyurethane.americanchemistry.com/>.
4. Aymes-Chodur, C., *Radiation effects on a linear model compound for polyethers*. Polymer Degradation and Stability, 2011.
5. Fromentin, E., et al., *Leaching of Radio-oxidized Poly(ester urethane): Water-Soluble Molecules Characterization*. Polymer Degradation and Stability 2016.
6. Pretzel, C.W., *ES&H DEVELOPMENT ACTIVITIES FOR THE W89 WARHEAD*. SAND95-8232. 1995, Sandia National Laboratories: Oak Ridge, TN.
7. Maxwell, R.S., *NMR Analysis of Gamma-Radiation induced degradation of Halthane-88 Polyurethane Elastomers*. . Polymer Degradation and Stability, 2002. 82.
8. Lawrence, E.O., "*Method and apparatus for the acceleration of ions*". 1934: U.S. Patent 1948384.
9. Choppin, G., J.-O. Liljenzin, and J. Rydberg, *Radiochemistry and Nuclear Chemistry*. Third ed. 2002, Woburn, MA: British Library Cataloguing-in-Publication Data.
10. Goorley, J.T., et al., *Initial MCNP6 Release Overview - MCNP6 version 1.0, LA-UR-13-22934* (2013).
11. Rivaton, A. and J. Arnold, *Structural modifications of polymers under the impact of fast neutrons*. Polymer Degradation and Stability, 2008. 93 (10): p. 1864 - 1868.
12. Dannoux, A., et al., *Degradation kinetics of poly(ether-urethane) Estane® induced by electron irradiation*. Nuclear Instruments and Methods in Physics Research Section B: Beam Interactions with Materials and Atoms, 2005. 236(1-4): p. 488-494.
13. Walo, M., G. Przybytniak, and J. Sadło, *Radiation-induced radicals in aliphatic poly(ester urethane)s studied by EPR spectroscopy*. Journal of Molecular Structure, 2012. 1036 (2013): p. 488 - 493.

14. Adem, E., et al., *Effect of dose and temperature on the physical properties of an aliphatic thermoplastic polyurethane irradiated with an electron beam*. Radiation Physics and Chemistry, 2015. 112 (2015): p. 61-70.
15. Lacerda, M.A.S., et al., *Use of the MCNPX to calculate the neutron spectra around the GE-PETtrace 8 cyclotron of the CDTN/CNEN, Brazil*. Applied Radiation and Isotopes, 2014. 83(2014): p. 235-241.
16. Infantino, A., et al., *Accurate Monte Carlo modeling of cyclotrons for optimization of shielding and activation calculations in the biomedical field*. Radiation Physics and Chemistry, 2015. 116(2015): p. 231-236.
17. Cruzate, J.Á., *Estimate of the radiation source term for F-18 production via thick H₂O-¹⁸O targets bombarded with 18 MeV protons*. Radiation Physics and Chemistry, 2015. 117(Dec. 2015): p. 54-58.
18. Guimarães, A.M., et al., *Use of a TLD-based multisphere spectrometry system to measure the neutron spectra around a not-self-shielded PET cyclotron: Preliminary results*. Applied Radiation and Isotopes, 2012. 71(Dec. 2012): p. 92-95.
19. Hagiwara, M., et al., *Spectrum Measurement of Neutrons and Gamma-rays from Thick H₂O-¹⁸O Target Bombarded with 18 MeV Protons*. Journal of the Korean Physical Society 2011. 59(No. 2): p. 2035-2038.
20. Auditore, L., E. Amato, and S. Baldari, *Theoretical estimation of Cu-64 production with neutrons emitted during F-18 production with a 30 MeV medical cyclotron*. Applied Radiation and Isotopes, 2017. 122(April 2017): p. 229-234.
21. Infantino, A., et al., *Experimental measurement and Monte Carlo assessment of Argon-41 production in a PET cyclotron facility*. Physica Medica, 2015. 31(8): p. 991-996.
22. Healthcare, GE, *PETtrace 800 series - SERVICE MANUAL - ACEELERATOR*. 2011, GE Healthcare.
23. International Atomic Energy Agency, *Cyclotron Produced Radionuclides: GUIDANCE ON FACILITY DESIGN AND PRODUCTION OF [18F]FLUORODEOXYGLUCOSE (FDG)*, in *IAEA RADIOISOTOPES AND RADIOPHARMACEUTICALS SERIES No. 3*. 2012, International Atomic Energy Agency Vienna International Centre: Vienna, Austria.
24. International Atomic Energy Agency, *Cyclotron Produced Radionuclides: Guidelines for Setting Up a Facility*, in *Technical Reports Series, Report No.: 471*. 2009, Sales and Promotion, Publishing Section: Vienna, Austria.
25. *IAEA Nuclear Data Services*. Available from: <https://www-nds.iaea.org/>.

26. Capote, R., et al., *Journal of ASTM International (JAI)*. 2012. 9(4).
27. Nigg, D.W., et al., *Modification of the University of Washington Neutron Radiotherapy Facility for optimization of neutron capture enhanced fast-neutron therapy*. *Medical Physics* 2000. 27(359).
28. Atitar, M., et al., *The Relevance of ATR-FTIR Spectroscopy in Semiconductor Photocatalysis*. 2015.
29. Engle, J.W., E.R. Birnbaum, and M.E. Fassbender, *PARASITIC ISOTOPE PRODUCTION WITH CYCLOTRON BEAMGENERATED NEUTRONS*. 2013. TH2PB02.

Appendix

Synthesis for pre-polymer A 2000 M_n

2000 molecular weight (MW) PTMEG containing copolymer A: In an oven dried three neck 250 mL round bottom flask fitted with a thermometer adaptor and rubber septa, 4,4'-methylene-bis(cyclohexylisocyanate) (45 g, 0.172 mol, 2.75 equiv.) was added. The flask was flushed with nitrogen and then heated in an in oil bath to 60°C while stirring. Polytetrahydrofuran-2000 MW (PTMEG) was previously heated to 50°C in a round bottom flask and dried under high vacuum for four hours to remove all traces of water. The 2000 MW PTMEG (125 g, 0.0625 mol, 1 equiv.) was slowly added to the flask containing HMDI over 15 minutes at such a rate the mixture did not drop below 50°C. The reaction was maintained at 60°C under nitrogen atmosphere for 16 hours, resulting in a viscous clear liquid which was used without further purification.

Synthesis for pre-polymer A 650 M_n

650 MW PTMEG containing copolymer A: In an oven dried three neck 500 mL round bottom flask fitted with a thermometer adaptor and rubber septa, 4,4'-methylene-bis(cyclohexylisocyanate) (75.8 g, 0.289 mol, 2.21 equiv.) was added by cannula transfer. The flask was flushed with nitrogen and heated in an in oil bath to 55°C while stirring vigorously. Polytetrahydrofuran-650 MW (PTMEG) was heated to 40°C and dried under high vacuum for four hours to remove all traces of water. The 650 MW PTMEG (85 g, 0.131 mol, 1 equiv.) was slowly added to the flask containing HMDI over 15 minutes.

The reaction was maintained at 55°C under nitrogen atmosphere for 16 hours, resulting in a highly viscous clear liquid which was used without further purification.

MCNP input file calculating neutron flux using TENDL for 3 inch position on Bruce target assembly.

IRRADIATION OF O18 ENRICHED WATER WITH 16.5 MEV PROTONS

```

c ***** BLOCK 1: CELL CARDS
*****
c          O18 Enriched Water
1  4  -1.11 (-2 7 -8):(3 -4 -5 6 7 -8):(-1 7 -8) imp:n=1  imp:h=1
c          Tantalum Insert
2  2  -16.69 -9 10 -8 (2 :-7 :8)(1 :-7 :8)(5 :-6 :4 :-3 :-7 :8)
    imp:n=1  imp:h=1
c          Havar Foil
3  3  -8.30397 8 -11 -9 imp:n=1  imp:h=1
c          Block 2 (aluminum)
4  1  -2.6989 -15 13 14 -12 16 -17 (9 :-10 :8) imp:n=1  imp:h=1
c          Block 1 (aluminum)
5  1  -2.6989 -15 -18 12 14 16 -17 (9 :11)(1 :-11 :18) imp:n=1
    imp:h=1
c          Block 3 (aluminum)
6  1  -2.6989 -15 14 20 -21 -13 19 imp:n=1  imp:h=1
c          Room (air)
7  6  -0.001205 -22 (-19 :13 :15 :-14 :-20 :21)(15 :-14 :-13 :18 :-16
    :17)(23 :25 :-15)(-29 :28 :33) imp:n=1  imp:h=1
c          Cadmium Cover 2 "hot"
8  0  -25 -23 15 (26 :-27 :24) imp:n=1  imp:h=1
c          Cadmium 2 "hot" Interior (air)
9  6  -0.001205 27 -26 -24 imp:n=1  imp:h=1
c          Beam Vacuum
10  0  -1 11 -18 imp:n=1  imp:h=1
c          Graveyard
11  0  22 imp:n=0  imp:h=0
c          Cadmium Cover 2 "cold"
12  0  -33 29 -28 (34 :-30 :31) imp:n=1  imp:h=1
c          Cadmium 2 Interior (air)
13  6  -0.001205 -31 30 -34 imp:n=1  imp:h=1

```

c ***** BLOCK 2: SURFACE CARDS

1 c/x 0 -0.3625 0.745 \$ CYLINDER (water)
2 c/x 0 0.3625 0.745 \$ CYLINDER (water)
3 py -0.745 \$ RIGHT PLANE (water)
4 py 0.745 \$ LEFT PLANE (water)
5 pz 0.3625 \$ TOP PLANE (water)
6 pz -0.3625 \$ BOTTOM PLANE (water)
7 px 0 \$ BACK PLANE (water)
8 px 1.5 \$ FRONT PLANE (water)
9 cx 1.95 \$ CYLINDER (tantulum)
10 px -0.23 \$ BACK PLANE (tantulum)
11 px 1.505 \$ FRONT PLANE (havar)
12 px 1.14 \$ FRONT PLANE (block 2)
13 px -1.81 \$ BACK PLANE (block 2)
14 pz -2.8075 \$ BOTTOM PLANE (all blocks)
15 pz 2.8075 \$ TOP PLANE (all blocks)
16 py -3.8125 \$ RIGHT PLANE (blocks 1&2)
17 py 3.8125 \$ LEFT PLANE (blocks 1&2)
18 px 3 \$ FRONT PLANE (block 1)
19 px -6.37 \$ BACK PLANE (block 3)
20 py -5.275 \$ RIGHT PLANE (block 3)
21 py 5.275 \$ LEFT PLANE (block 3)
22 so 55 \$ SPHERE (room)
23 c/z -1.3 0 0.735 \$ CYLINDER (cadmium 2 "hot")
24 c/z -1.3 0 0.635 \$ CYLINDER (cadmium 2 "hot")
25 pz 3.2075 \$ TOP PLANE 1 (cadmium 2 "hot")
26 pz 3.1075 \$ TOP PLANE 2 (cadmium 2 "hot")
27 pz 2.9075 \$ BOTTOM PLANE (cadmium 2 "hot")
28 px -36.85 \$ FRONT PLANE (cadmium 1 "cold")
29 px -37.25 \$ BACK PLANE (cadmium 1 "cold")
30 px -37.15 \$ INNER BACK (cadmium 1 "cold")
31 px -36.95 \$ INNER FRONT (cadmium 1 "cold")
33 c/x 0 -0.3625 0.735 \$ CYLINDER (cadmium 1 "cold")
34 c/x 0 -0.3625 0.635 \$ CYLINDER (cadmium 1 "cold")

c ***** BLOCK 3: DATA CARDS

mode n h

c ***** MATERIALS

m1 13027. 1 \$ aluminum
m2 73181. 0.99988 \$ tantalum
73180. 0.00012

m3 27059. 0.42 \$ havar foil

24050.	0.00847275	24052.	0.1633886	24053.	0.01852695
24054.	0.00461175	28058.	0.08645766	28060.	0.03330334
28061.	0.001447673	28062.	0.004615815	28064.	0.001175512
74180.	3.24e-005	74182.	0.007155	74183.	0.0038637
74184.	0.0082728	74186.	0.0076761	42092.	0.0032494
42094.	0.0020306	42095.	0.003498	42096.	0.0036696
42097.	0.0021032	42098.	0.0053218	42100.	0.0021274
25055.	0.016	6012.	0.0019786	6013.	2.14e-005
26054.	0.01116395	26056.	0.1752501	26057.	0.00404729
26058.	0.00053862				

m4 1001. 0.6665903 \$ O-18 enriched water

1002.	7.666671e-005	8018.	0.3166664	8016.	0.01666665
-------	---------------	-------	-----------	-------	------------

m6 6012. 0.00015 \$ air

7014.	0.784431	8016.	0.210748	18040.	0.004671
-------	----------	-------	----------	--------	----------

m7 48106. 0.0125 \$ cadmium

48108.	0.0089	48110.	0.1249	48111.	0.128
48112.	0.2413	48113.	0.1222	48114.	0.2873
48116.	0.0749				

c ***** CROSS SECTIONS

xs1 8018.00h 17.844540 tendlo18 0 1 1 81324
 xs2 8018.00c 17.844540 tendlo18c 0 1 1 176189 0 0 2.526E-08
 xs3 27059.00h 58.426930 tendlco59 0 1 1 80925
 xs4 74180.00h 178.400900 tendlw180 0 1 1 80897
 xs5 42092.00h 91.117290 tendlmo92 0 1 1 73142
 xs6 42094.00h 93.098400 tendlmo94 0 1 1 79308
 xs7 42095.00h 94.090560 tendlmo95 0 1 1 82674
 xs8 42096.00h 95.080820 tendlmo96 0 1 1 80308
 xs9 42097.00h 96.073550 tendlmo97 0 1 1 83727
 xs10 42098.00h 97.064350 tendlmo98 0 1 1 81487
 xs11 42100.00h 99.049220 tendlmo100 0 1 1 83395
 xs14 25055.00h 54.466100 tendlmn55 0 1 1 82412
 xs15 6013.00h 12.891650 tendlc13 0 1 1 74831
 xs16 26054.00h 53.476250 tendlfe54 0 1 1 72104
 xs17 26056.00h 55.454430 tendlfe56 0 1 1 76260
 xs18 26057.00h 56.446290 tendlfe57 0 1 1 81483
 xs19 26058.00h 57.435600 tendlfe58 0 1 1 79699
 xs20 73180.00h 178.401600 tendlta180 0 1 1 85582
 xs21 73181.00h 179.393600 tendlta181 0 1 1 84301

c ***** Physics Model

c lca 8j 2

```

c ***** SOURCE
*****
sdef axs=-1 0 0 x=1.505 y=d1 z=d2 par=9 erg=16.5 vector=-1 0 0 dir=1
sp1 -41 0.4 0
sp2 -41 0.2 -0.3625
nps 100000000
c ***** TALLIES
*****
fc5 Neutron Flux Point Detector HOT
f5:n -1.3 0 3.0075 .1
fm5 3.9508e14
e0 0.001 0.5 1 1.5 2 2.5 3 3.5 4 4.5 5 5.5 6 6.5 7 7.5 8 8.5 9 16.5
c
fc15 Neutron Flux Point Detector COLD 14"
f15:n -37.05 0 -.325 .1
fm15 3.9508e14
c e15 0.001 4 9 15
c
fc25 Neutron Flux Point Detector 7"
f25:n -18.5 0 -.325 .1
fm25 3.9508e14
c e25 0.001 4 9 15

```